Forschungszentrum Karlsruhe
in der Helmholtz-Gemeinschaft
Wissenschaftliche Berichte
FZKA 7412

Three-dimensional Liquid Metal Flows in Strong Magnetic Fields

L. Bühler

Institut für Kern- und Energietechnik
Programm Kernfusion

September 2008

Forschungszentrum Karlsruhe
in der Helmholtz Gemeinschaft

Wissenschaftliche Berichte

FZKA 7412

Three-dimensional liquid metal flows in strong magnetic fields

L. Bühler

Institut für Kern- und Energietechnik
Programm Kernfusion

Von der Fakultät für Maschinenbau
der Universität Karlsruhe (TH)
genehmigte Habilitationsschrift

Forschungszentrum Karlsruhe GmbH, Karlsruhe
2008

Forschungszentrum Karlsruhe GmbH
Postfach 3640, 76021 Karlsruhe

Mitglied der Hermann von Helmholtz-Gemeinschaft
Deutscher Forschungszentren (HGF)

ISSN 0947-8620

urn:nbn:de:0005-074129

Three-dimensional liquid metal flows in strong magnetic fields

Abstract

The prediction of three-dimensional MHD flows for applications in fusion engineering, where magnetic fields confining the plasma are very high, is still a challenging task since, up to the present day, numerical simulations for such conditions are beyond the capabilities of modern CFD tools. Also experimentally, on laboratory scales, these values of parameters are hard to reach. Asymptotic analyses instead are able to cover such regimes in which inertia and viscous forces play only a minor role in comparison with the strong electromagnetic forces. However, especially for geometries with sudden changes of cross section, inertia effects may still be present in thin viscous parallel layers, where relatively high values of velocity can occur. For such cases only numerical simulations and/or experiments can give the proper insight into the physics involved. Those methods are therefore applied to determine the relevant scaling laws for strong fields, which allow a physically meaningful extrapolation of data to the desired parameters for engineering applications.

As an example the 3D MHD flow through a sudden expansion of rectangular ducts is considered; results have been obtained by asymptotic theory for strong magnetic fields, by numerical simulations up to moderate magnetic fields and they are compared with experimental data. It is possible to derive the relevant scaling laws for pressure drop, as a function of the Hartmann number Ha and the interaction parameter N. Results obtained by asymptotic analysis and numerical simulations show quite good agreement with experiments for the investigated parameters. Moreover, the numerical simulations allow analyzing the interesting 3D transitions and changes in the flow topology, occurring in the parameter range between the hydrodynamic case with $Ha = 0$ and the strong field case where $Ha \gg 1$, $N \gg 1$.

Dreidimensionale Flüssigmetall-Strömungen in starken Magnetfeldern

Zusammenfassung

Die Vorhersage dreidimensionaler magnetohydrodynamischer Strömungen für Anwendungen in der Fusionstechnologie, wo starke Magnetfelder zum Plasmaeinschluss Verwendung finden, stellt bis heute eine Herausforderung dar, da numerische Simulationen für derartige Bedingungen verfügbare CFD Programme überfordern. Auch experimentell lassen sich diese Strömungen bei den relevanten Parametern im Labormaßstab nur schwer realisieren. Asymptotische Verfahren hingegen sind in der Lage, solche Bereiche abzudecken, bei denen Trägheits- und Reibungskräfte eine untergeordnete Rolle im Vergleich mit den starken elektromagnetischen Kräften spielen. Speziell für Geometrien mit abrupten Änderungen des Strömungsquerschnitts können Trägheitskräfte trotzdem von Bedeutung sein, da in dünnen Grenzschichten relativ hohe Geschwindigkeiten auftreten können. Für solche Anwendungen verschaffen uns nur numerische Simulationen und/oder Experimente einen Einblick in das physikalische Verhalten. Deshalb werden die zuvor genannten Methoden zusammen angewandt, um die charakteristischen Skalierungsgesetze für starke Magnetfelder zu bestimmen, die eine sinnvolle Extrapolation der Daten in den Parameterbereich der technischen Anwendungen ermöglichen.

Als Beispiel wird eine dreidimensionale Strömung durch eine plötzliche Querschnittserweiterung rechteckiger Kanäle betrachtet. Ergebnisse, die für moderate Magnetfelder durch numerische Simulationen und für starke Magnetfelder mittels asymptotischer Verfahren ermittelt wurden, werden mit experimentellen Daten verglichen. Damit ist es möglich, die relevanten Skalierungsgesetze für den Druckverlust als Funktion der Hartmann Zahl Ha und des Interaktionsparameters N abzuleiten. Die Ergebnisse asymptotischer Rechnungen und numerischer Simulationen zeigen im untersuchten Parameterbereich recht gute Übereinstimmung mit Experimenten. Darüber hinaus erlauben die numerischen Simulationen einen Einblick in den interessanten Übergangsbereich zwischen hydrodynamischer Strömung bei $Ha = 0$ und Strömungen in starken Magnetfeldern bei $Ha \gg 1$, $N \gg 1$, in dem die Strömung ihre Topologie verändert.

.

Three-dimensional liquid metal flows in strong magnetic fields

Contents

1 Introduction

Blankets in future nuclear fusion reactors are fundamental components for energy conversion, heat removal and tritium production. Liquid metals such as Li or the PbLi alloy may serve as breeding material for generation of tritium, one fuel component, that does not occur naturally. For tritium removal and purification of the liquid metal the breeder has to be slowly circulated towards external facilities. The motion of the electrically conducting fluid through the strong magnetic field confining the fusion plasma, leads to the induction of electric currents. Their interaction with the magnetic field creates the Lorentz force that finally dominates the fluid flow when the magnetic field is high.

The fusion power is released within the liquid metal and the solid blanket structure. Any design concept which uses liquid metals also as coolants needs fluid velocities of sufficient magnitude in order to ensure save cooling conditions. However, with higher velocity the magnetohydrodynamic interaction increases strongly so that the pressure difference that is required to drive the flow at desired speed may reach unacceptably high values. This is the case especially for flows in ducts with electrically conducting walls where currents find possible shortcuts through the walls. A reasonable mean for pressure drop reduction is the use of electrically insulating walls or layers that decouple the liquid metal from the wall, minimize currents, the associated Lorentz force and pressure drop. Electrically insulating walls fabricated from silicon carbide composite materials are indeed considered in conceptual studies of highly advanced reactor models (Giancarli, Golfier, Nishio, Raffray, Wong and Yamada (2002)), but the technological feasibility of such designs remains to be proven.

Near-term blanket research focuses therefore on more or less standard technologies where walls are fabricated from steel and no insulation at the wall is foreseen. For that reason in general the liquid metal is not used as a coolant any more and a separate cooling system is required. The currently proposed designs of blankets consider walls which have internal cooling channels through which the electrically non-conducting coolant (helium at high pressure) flows at high speed to remove the fusion heat. The liquid metal instead circulates at very low velocity, required for tritium extraction. Since the average velocities are very small, inertia forces give only a minor contribution to the momentum balance, i.e. to the pressure drop, but they could still affect the topology of the flow.

In the proposed design concept known as *Helium Cooled Lithium Lead* blanket, the liquid metal flows between cooling plates that form narrow gaps with high aspect ratio. The fluid is distributed to and collected from the breeding zone through a piping system which has much smaller dimensions. This means that at the entrance and at the exit of the blanket module the geometry expands and contracts preferentially in the direction of the magnetic field.

Expansions and contractions are important elements of actual fusion blankets and they are also basic geometric components of any liquid metal device. They received attention in the past by a number of authors and one should recall as examples the experiments reported by Branover, Vasil'ev and Gel'fgat (1967), Gel'fgat and Kit (1971) who consider MHD flows in insulating sudden expansions, or Walker, Ludford and Hunt (1972) who study MHD flows through smoothly expanding insulating channels using an inertialess approximation. Smooth expansions with thin conducting walls are considered by Walker (1981) or by Picologlou, Reed, Hua, Barleon, Kreuzinger and Walker (1989)

The present work considers MHD flows in a single expansion as shown in Fig. 1. The expanding flow problem is used here as an example to highlight the need of combining computational fluid dynamics (CFD) simulations, inertialess asymptotic techniques and experiments in order to achieve a complete understanding of the flow phenomena in fusion applications. The parameter range accessible with CFD includes applications with low and moderate magnetic fields. Within this range the flow undergoes practically all the changes in topology from a pure hydrodynamic flow towards one dominated by magnetohydrodynamics. These nonlinear transitions can be predicted only by numerical tools that take into account all the terms present in the governing equations. The asymptotic approach, however, works best in the range of very strong fields, where inertia terms become negligible and viscous effects are confined to thin boundary and internal layers. Experiments in strong fields are necessary to provide a data base for validation of the theoretical approaches. On the other hand, laboratory conditions often cannot meet the fusion relevant parameter range so that extrapolations of experimental results, supported by the scaling laws derived from asymptotic analysis, are required.

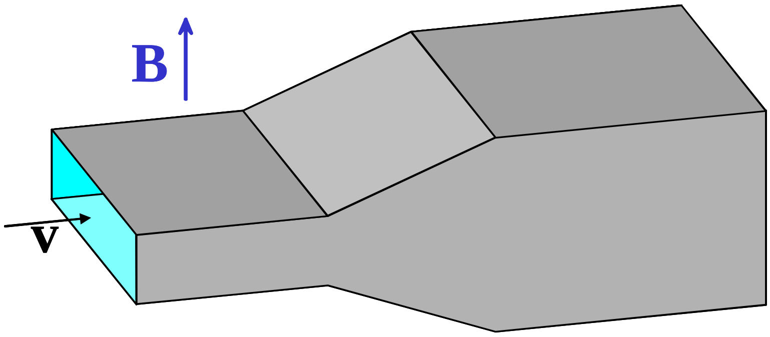

Figure 1: Sketch of an expansion.

2 Theoretical analysis

2.1 Governing equations

Let us consider the incompressible viscous magnetohydrodynamic flow of an electrically conducting fluid, governed by the balance of momentum

$$\frac{1}{N}\left[\partial_t \mathbf{v} + (\mathbf{v}\cdot\nabla)\,\mathbf{v}\right] = -\,\nabla p + \frac{1}{Ha^2}\nabla^2\mathbf{v} + \mathbf{j}\times\mathbf{B}, \tag{1}$$

mass conservation

$$\nabla\cdot\mathbf{v} = 0, \tag{2}$$

and by Ohm's law

$$\mathbf{j} = -\nabla\phi + \mathbf{v}\times\mathbf{B}. \tag{3}$$

Conservation of charge

$$\nabla\cdot\mathbf{j} = 0 \tag{4}$$

is identically satisfied if the electric potential ϕ in (3) is determined as

$$\nabla^2\phi = \nabla\cdot(\mathbf{v}\times\mathbf{B})\,. \tag{5}$$

In the equations shown above $\mathbf{v}$, $\mathbf{B}$, $\mathbf{j}$, p, ϕ stand for velocity, magnetic induction, current density, pressure and electric potential, scaled by the reference quantities u_0, B_0, $j_0 = \sigma u_0 B_0$, $\sigma a u_0 B_0^2$ and $a u_0 B_0$, respectively. The scale of velocity u_0 is chosen as the average velocity in a particular cross section of the duct where a is a typical length scale. The quantity B_0 is the magnitude of the applied magnetic induction. The fluid properties like the electric conductivity σ, the kinematic viscosity ν, and the density ρ, are assumed to be constant.

The flow is governed by a balance between inertia forces, pressure forces, viscous forces and Lorentz forces. The current density $\mathbf{j}$ in the *Lorentz force* term $\mathbf{j}\times\mathbf{B}$ is determined through (3) by the gradient of the electric potential ϕ and the *induced electric field* $\mathbf{v}\times\mathbf{B}$ due to the motion of the electrically conducting fluid with velocity $\mathbf{v}$, subject to a magnetic field $\mathbf{B}$. The ratios of different forces are expressed through the two nondimensional parameters, the Hartmann number Ha and the interaction parameter N

$$Ha = aB_0\sqrt{\frac{\sigma}{\rho\nu}}\,, \qquad N = \frac{a\sigma B_0^2}{\rho u_0}\,. \tag{6}$$

The square of the Hartmann number characterizes the ratio of electromagnetic forces to viscous forces while the interaction parameter represents the ratio of electromagnetic forces to inertia forces.

The hydrodynamic Reynolds number can be expressed in terms of Ha and N as

$$Re = \frac{Ha^2}{N}. \tag{7}$$

The equations shown above represent already a simplification from the more general Maxwell equations that describe the complete electrodynamic behavior. They are valid in the limit of vanishing magnetic Reynolds number $R_m = \mu\sigma a u_0 \to 0$, for which the dynamics of the magnetic field is neglected. The field $\mathbf{B}$ is here considered as a given stationary quantity, externally applied and unaffected by the flow, with the consequence that the electric field can be derived from the gradient of the scalar electric potential ϕ. For almost all industrial and laboratory applications R_m is small so that this so-called *inductionless approximation* is fairly valid for channel flows. Moreover, Walker (1986b) showed that the requirement on R_m can be further relaxed if the current density is small, as it is the case e.g. for ducts with thin or poorly conducting walls.

At the fluid wall interface the flow satisfies the no-slip condition,

$$\mathbf{v} = 0, \tag{8}$$

and continuity of wall normal current and electric potential (no contact resistance)

$$\mathbf{j} \cdot \mathbf{n} = \mathbf{j}_w \cdot \mathbf{n}, \quad \phi = \phi_w. \tag{9}$$

Here the subscript w stands for variables in the wall.

In the wall, the currents are determined by the gradient of the wall potential and charge conservation,

$$\mathbf{j}_w = -\frac{\sigma_w}{\sigma} \nabla \phi_w \ \text{ with } \nabla \cdot \mathbf{j}_w = 0. \tag{10}$$

If the duct walls are thin and electrically conducting the latter equations simplify to the so-called *thin-wall approximation* (compare Walker (1981)) for the determination of the wall potential ϕ_w according to

$$\mathbf{j} \cdot \mathbf{n} = -\frac{\partial \phi}{\partial n} = \nabla \cdot \left(c \nabla_t \phi_w \right). \tag{11}$$

Here ∇_t denotes the components of the gradient operator in directions tangential to the wall, $\mathbf{n}$ is the inward unit normal to the wall and c stands for the wall conductance ratio

$$c = \frac{\sigma_w t_w}{\sigma a}. \tag{12}$$

It describes the conductivity of the wall with thickness $t_w \ll a$ compared with the conductivity of the fluid. The boundary condition (11) is a result of integrating (10) across the *thin* wall along its normal direction and taking into account that the potential does not vary along the thickness to the leading order of approximation. Since the wall is thin, wall currents driven by gradients of ϕ_w flow preferentially in tangential direction. Currents leaving the fluid enter the tangential balance (11) as a source term. See also Fig. 2.

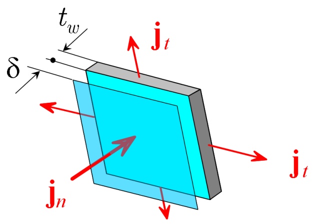

Figure 2: Sketch for thin-wall boundary condition. Currents leaving the fluid enter the wall in which they flow preferentially in tangential direction.

2.2 Numerical solutions and related problems

The equations shown above can be solved in principle using numerical methods as available in commercial CFD codes. In general, MHD is not an option in such codes so that an extension of the code has to be implemented by the user through modeling of the Lorentz force $\mathbf{j} \times \mathbf{B}$ as a source term in the momentum equation (1). The equation (5) for electric potential is a diffusive transport equation in which the induced electric field $\mathbf{v} \times \mathbf{B}$ appears as a source term. This type of equation is usually available in commercial codes. From a principle point of view such a modeling through user defined subroutines seems straight forward and it may yield reasonable results for applications with moderate magnetic fields. Some applications of the user-extended commercial code CFX are discussed below to show the capability and the limits of such an approach. The implementation of the equations and details of the analysis have been described by Mistrangelo (2005).

The purpose of this subsection is to highlight the major difficulties encountered during numerical modelling of 3D MHD flows in strong magnetic fields, i.e. at high Hartmann numbers $Ha \gg 1$. The list shown below justifies serious doubts concerning the accuracy of numerical predictions for strong fields so that a careful validation of numerically obtained results is required.

For applications in very strong magnetic fields, when the Hartmann number becomes quite large, the equations displayed above constitute a singular perturbation problem. As a result, the viscous term in the momentum equation (1) becomes negligible in most of the fluid domain called the *core*, where the flow behaves nearly as being inviscid. Viscous effects remain confined within very thin viscous boundary or internal layers. Boundary layers at walls where the magnetic field has a normal component are known as the *Hartmann layers* and the corresponding wall is called the *Hartmann wall.* The thickness of the Hartmann layers scales typically as $\delta_H \sim Ha^{-1}$. Walls which are entirely aligned with the magnetic field are known as *side walls* or *parallel walls* and the thickness of viscous *parallel layers,* which develop along those walls, scales as $\delta_S \sim Ha^{-1/2}$. Properties of Hartmann layers and MHD flows at high Hartmann numbers have been first investigated theoretically and experimentally by Hartmann (1937) and Hartmann and Lazarus (1937) while the details of parallel layers have been studied initially by Shercliff (1953) for insulating walls, and by Hunt (1965) for electrically conducting walls. The latter author shows that the conductivity of the walls influences greatly the velocity profile and that situations are possible, where the thin side layers can carry a flow rate of the order one, or in the most extreme case, practically all the flow. Typical velocity profiles are shown in Fig. 3 for a moderate Hartmann number $Ha = 50$.

The scales for viscous layers show already one major difficulty for numerical predictions of MHD flows for fusion applications, where the Hartmann number can exceed even values of $Ha > 10^4$. For such high values of characteristic parameters there is a formation of extremely thin layers along Hartmann walls, and depending on the wall conductance, of high-velocity jets along side walls. A proper numerical resolution of these layers requires an enormous computational effort. The viscous details of Hartmann layers at $z = \pm 1$ may appear unimportant at a first view with the focus on the profile of velocity. However, these layers provide a closed path for electric currents which are induced in the inviscid core. The thickness of the Hartmann layers determines thereby the electric resistance of the global current path and the magnitude of current density in the whole cross section. An insufficient numerical resolution of these layers, especially along poorly conducting or insulating walls, leads not only to inaccurate predictions of

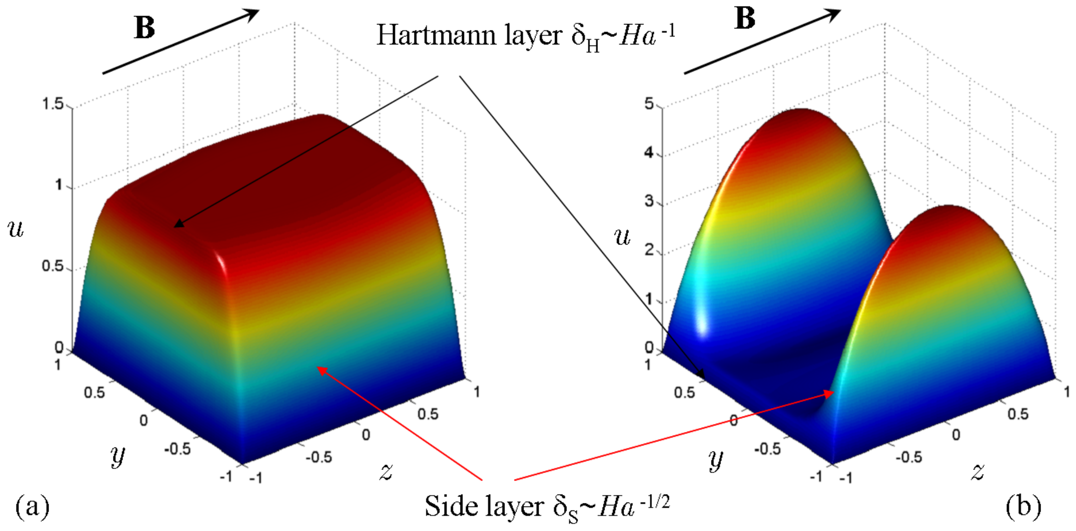

Figure 3: Fully developed velocity profiles in rectangular ducts with (a) all walls insulating (Shercliff 1953), (b) Hartmann walls perfectly conducting and side walls insulating (Hunt 1965), for $Ha = 50$. Colors indicate the magnitude of velocity.

the flow close to the wall but to wrong solutions in the whole fluid domain, even in the inviscid core. A sketch of current path is shown in Fig. 4a. Limitations in computational resources restricted the numerical solutions for 3D MHD flows in the past to applications with Hartmann numbers of a few hundred, see e.g. Sterl (1990), and even with modern codes and powerful computational facilities it is still difficult to go beyond $Ha = 1000$ and to predict accurately general 3D flows (Mistrangelo and Bühler (2007)).

Another difficulty in modeling of MHD flows is the fact that the computational domain does not end at the fluid-solid interface. Currents which are induced in the fluid may enter the walls and shortcut their path along the walls. This requires additionally an adequate numerical resolution of the walls and increases further the computational effort. Moreover, inspection of (11) shows that the wall potential is primarily governed by the solution of a 2D Poisson type equation in the plane of the wall, with a source term proportional to $c^{-1}\frac{\partial\phi}{\partial n}$. Usually duct walls are thin compared with the size of the cross section, with the consequence that c may become relatively small, i.e. $c \ll 1$. For such conditions even small numerical errors in $\frac{\partial\phi}{\partial n}$ get amplified when divided by the small quantity c. As a consequence the system of algebraic equations derived from the discretized Poisson equation looses its diagonal dominance and efficient iterative solution methods fail.

A similar problem arises from Ohm's law (3). As outlined above the current density is limited by the resistance of the walls or of the Hartmann layers. Therefore the magnitude of current density in the core may be of the order of c for conducting walls or of the order of Ha^{-1} for insulating walls. This small current density $\mathbf{j}$ is balanced by the sum of two order one terms on the right-hand side. Even if both of these latter terms are known to a certain degree of precision, the determination of $\mathbf{j}$ is less accurate and relative errors can be larger by a factor of c^{-1} or Ha compared with the numerical errors for potential gradient or velocity. When introduced

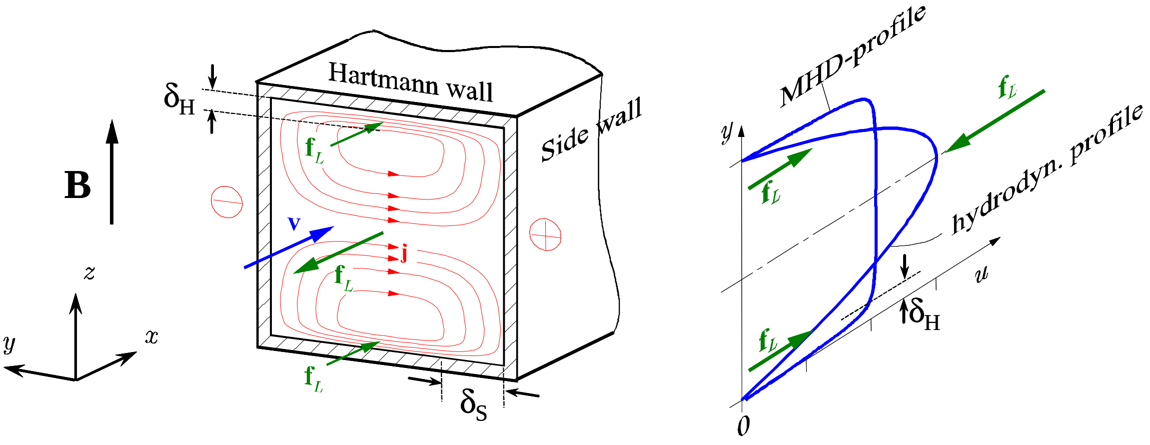

(a) (b)

Figure 4: a) Principle sketch of the phenomenology of MHD channel flow, b) velocity profile in the middle of the ducts at $z = 0$ and influence of Lorentz force $\mathbf{f}_L$ on the viscous velocity profile.

in the momentum equation, inaccurate current density yields imprecise results for velocity and even worse results for currents in the next iteration step unless quite strong underrelaxation is introduced.

For all these reasons, present numerical simulations cannot cover or reach the relevant parameter range required for predictions of MHD flows for fusion applications. Some of the restrictions can, however, be relaxed by applying the thin-wall condition directly instead of resolving the wall and by using analytically known wall functions to describe the details in boundary layers. For special geometries like rectangular ducts this method has proven its computational capability, even for time-dependent flows, for which the transition from 3D flows to a quasi two-dimensional flow has been studied (Mück, Günther, Müller and Bühler (2000)). A general formulation for analytical wall functions has been presented by Widlund (2003) but an implementation of these ideas into a flexible CFD software is still not available.

The most important aspect of the Hartmann layers is their ability to provide a path where currents may close, i.e. the Hartmann layer increases virtually the local conductivity near the wall. A detailed boundary layer analysis shows that the thin wall condition becomes extended to

$$-\frac{\partial \phi}{\partial n} = \nabla \cdot \left[\left(c + \delta_H \right) \nabla_t \phi_w \right], \tag{13}$$

where $\delta_H = \left(Ha \left| \mathbf{n} \cdot \mathbf{B} \right| \right)^{-1}$ stands for the local dimensionless thickness of the Hartmann layer (see Fig. 2 or Bühler (1995)). The equivalent condition valid at insulating walls has been given by Walker, Ludford and Hunt (1971).

However, even if today's numerical simulations are unable to predict the MHD flows for fusion applications, they offer the great advantage of getting valuable insight into the phenomena that determine the flow in strong magnetic fields. Most changes in the flow topology occur already at magnetic fields or Hartmann numbers which are accessible with the simulations. Some of them will be described later in this work, i.e. the modification of flow separation and recirculation regions with the strength of the magnetic field, the tendency to develop quasi 2D structures, the formation of thin boundary and internal layers including their typical scaling laws etc. (Mistrangelo and Bühler (2005), Mistrangelo (2005)).

At present day only numerical methods based on asymptotic techniques are able to cover the Hartmann number parameter range of 3D fusion relevant MHD flows. Experiments constitute a valuable data base for validation of numerical tools and of asymptotic models. Moreover, with the knowledge of the proper scaling laws, obtained from experiments and theory, it is further possible to extrapolate the experimental results and perhaps numerical predictions towards the parameter range of applications.

The present work aims at highlighting the importance of numerical simulations, asymptotic analyses and experiments for obtaining a complete and reliable understanding of the physics of MHD flows at very high Hartmann numbers. Each of these methods is important to get the overall picture of the flow and to obtain results for fusion relevant parameters. As an illustrating example the flow in an expansion will be considered in more detail.

2.3 Inertialess approximation for MHD flows

The inertialess approach exploits the fact that for many applications not only the Hartmann number but also the interaction parameter is very large. The latter one may take values like $N = 10^3 - 10^5$. For very high N, or better as $N \to \infty$, the inertial terms in the momentum equation vanish and the problem becomes linear. The main balance of momentum is then established in the core by an equilibrium between pressure force and Lorentz force terms. Moreover, the variation of variables along magnetic field lines is then known so that the governing equations can be integrated analytically in the direction of the field. This reduces the problem by one dimension by generating a sort of "*projection*" of the flow onto the duct walls on which the numerical solution is obtained as a solution of a 2D problem. After that is known, it is possible to reconstruct the 3D flow in the core and even in viscous boundary and internal layers. The basic idea has been initially proposed by Kulikovskii (1974), the formulation in tensor notation and its implementation in an efficient numerical code has been described by Bühler (1995) and finally the subject was summarized by Müller and Bühler (2001). For that reason the details are skipped here but the focus is placed later on the reconstruction of viscous side layers and internal layers, which represents an extension of the mentioned analysis. As a basis for the boundary layer analysis some equations are shown below that describe the variation of key variables in the inertialess limit.

In the following analysis we suppose that the magnetic field is uniform, and we chose the coordinate system in such a way that $\mathbf{B} = \hat{\mathbf{z}}$. The electromagnetic force or Lorentz force then becomes $\mathbf{j} \times \mathbf{B} = j_y\hat{\mathbf{x}} - j_x\hat{\mathbf{y}}$ and the induced electric field is $\mathbf{v} \times \mathbf{B} = v\hat{\mathbf{x}} - u\hat{\mathbf{y}}$. In this frame of reference the three components of the momentum equation read in the inertialess limit, i.e. when $N \to \infty$,

$$\begin{array}{lll} \partial_x p & -j_y & = \frac{1}{Ha^2}\nabla^2 u, \\ \partial_y p & +j_x & = \frac{1}{Ha^2}\nabla^2 v, \\ \partial_z p & & = \frac{1}{Ha^2}\nabla^2 w. \end{array} \tag{14}$$

Ohm's law becomes

$$\begin{aligned} -\partial_x\phi & \quad +v && = j_x, \\ -\partial_y\phi & \quad -u && = j_y, \\ -\partial_z\phi & && = j_z, \end{aligned} \tag{15}$$

and conservation of mass and charge are expressed as

$$\partial_x u + \partial_y v + \partial_z w = 0, \tag{16}$$

$$\partial_x j_x + \partial_y j_y + \partial_z j_z = 0. \tag{17}$$

It is possible to reduce the number of unknowns in the basic equations (14)-(17) by eliminating current density and velocity and to decouple equations for potential and for pressure. To proceed in this direction we differentiate the x and y component of the momentum equation (14) with respect to y and x and eliminate pressure. This yields with (17)

$$-\partial_y j_y - \partial_x j_x = \partial_z j_z = \frac{1}{Ha^2}\nabla^2\left(\partial_y u - \partial_x v\right). \tag{18}$$

Application of charge conservation (17) in Ohm's law (15) leads to

$$\partial_y u - \partial_x v = -\nabla^2\phi, \tag{19}$$

so that we find from (18) with $\partial_z j_z = -\partial_{zz}\phi$ (15) the equation governing potential as

$$\frac{1}{Ha^2}\nabla^4\phi = \partial_{zz}\phi. \tag{20}$$

Similarly it is possible to derive an equation governing the pressure distribution. By applying the divergence operator on (14) and using Ohm's law (15) and mass conservation (16) we find

$$\nabla^2 p = \partial_z w. \tag{21}$$

After applying the operator ∇^2 we recover

$$\nabla^4 p = \partial_z \nabla^2 w \tag{22}$$

and using the $z-$ component of (14) we find

$$\frac{1}{Ha^2}\nabla^4 p = \partial_{zz} p. \tag{23}$$

We may also derive an equation governing the component of velocity w. Differentiation of (21) with respect to z and use of the z component of (14) yields

$$\frac{1}{Ha^2}\nabla^4 w = \partial_{zz} w. \tag{24}$$

Equations (20), (23), and (24) are exact in the inertialess limit. These equations are used later to reconstruct viscous solutions in thin boundary and internal layers after a solution for the core flow has been obtained.

The flow in the core is calculated using a numerical code based on asymptotic techniques that is able to solve the MHD equations in an almost arbitrary domain. A brief description of that code and a number of application examples has been published by Bühler (1995).

Without giving here too much details about the analysis, some specific properties of the flow are highlighted which are required later for a reconstruction of the solution in the viscous layers. Let us consider the equations (14) in the inviscid limit as $Ha \to \infty$. It follows then immediately that

- the core pressure (subscript c indicates values in the core) is uniform along magnetic field lines, i.e.

$$\partial_z p_c = 0. \tag{25}$$

We find from (20) in the inviscid limit as $Ha \to \infty$ that $\partial_{zz}\phi = 0$. The potential varies linearly along magnetic field lines. For any z-symmetric problem, as the one studied below in Sect. 3, symmetry requires that $\phi(z) = \phi(-z)$ so that

- the core potential is uniform along magnetic field lines, independent of z,

$$\phi_c = \phi_c(x, y). \tag{26}$$

It can be shown that the conditions (25) and (26) are even valid with sufficient accuracy within the viscous Hartmann layers. The error in p and ϕ introduced by the approximation is of the order $O(Ha^{-2})$ if the magnetic field is perpendicular to the wall (Moreau (1990)) or $O(Ha^{-1})$ if the magnetic field has a normal and a tangential component to the wall.

Since p_c and ϕ_c do not vary along field lines it follows directly from Ohm's law (15) that

- the component of core velocity transverse to the field is uniform along magnetic field lines,

$$u_c = u_c(x, y), \quad v_c = v_c(x, y). \tag{27}$$

3 Inertialess expansion flows at high Hartmann numbers

For many applications in fusion engineering when the magnetic field is very high, i.e. $N \gg 1$, it is possible to neglect inertia forces and to obtain a first approximation for the flow using asymptotic methods. In the following examples, geometries are considered which expand in the direction of the magnetic field into a duct of square cross section. As typical scales for length and velocity the half width a and the average velocity u_0 in the large square duct are taken. All lengths shown from now on are dimensionless and scaled with a.

A sketch of such a geometry that expands along a finite length L is shown in Fig. 5. The geometry is built by two semi-infinite rectangular ducts. Along field lines the geometry extends from $-Z < z < Z$, i.e. the Hartmann walls are at $z = \pm Z\left(x\right)$. The side walls are at $y = \pm 1$. The large duct has a square cross section with Hartmann walls at $z = \pm Z_C = \pm 1$, while the Hartmann walls of the smaller duct are at $z = \pm Z_c$. The quantity Z_C/Z_c is called the expansion ratio.

A geometry with sharp corners at $x = \pm\frac{1}{2}L$ as shown in Fig. 5 leads to the formation of three cores. One is located in the small duct for $x < -\frac{1}{2}L$, one is within the expansion for $-\frac{1}{2}L < x < \frac{1}{2}L$, and the third one forms in the large duct for $x > \frac{1}{2}L$. The cores are separated from each other by two internal layers called the Ludford layers. These layers spread from the corners at $x = \pm\frac{1}{2}L$ into the fluid along magnetic field lines. The existence of such layers and their characteristic features for 2D expansions have been shown by Hunt and Leibovich (1967). The z- component of velocity varies within the Ludford layers in such a way that the values in the cores are approached asymptotically at both sides of the layer. A typical thickness of the Ludford layers for inertialess flows is $\delta_L \sim Ha^{-1/2}$. For very short expansions, say for L of the order of δ_L the intermediate core disappears and the Ludford layers merge forming a single expansion layer of thickness $\delta_e \sim Ha^{-1/2}$.

Let us consider as an example a smooth expansion with $Z\left(x\right) = Z_c + \frac{1}{2}\left(Z_C - Z_c\right)\left(1 + \sin\frac{\pi x}{L}\right)$ in the expansion region and $Z\left(x\right) = Z_c = 0.25$ and $Z\left(x\right) = Z_C = 1$ for the small and large duct, respectively. With this choice the expansion ratio becomes $Z_C/Z_c = 4$. The family of expansions depends on the length L of the expansion section. If the corners at $x = \pm\frac{1}{2}L$ are smooth, Ludford layers are not present any more and the solution exhibits only one single core. Nevertheless, the solution for velocity varies on a typical geometric scale L and the expansion layer appears again as $L < Ha^{-1/2}$.

In the following we discuss results for flows in well conducting ducts, where $c \gg Ha^{-1/2}$. For these conditions the flow in the core but also the mass fluxes carried by parallel layers become independent of the Hartmann number and the fluid flows in the core as being inviscid. With this assumption the currents carried by the viscous layers tangential to the walls become negligible in comparison with the currents carried inside the wall, so that the solution of the problem in the cores becomes independent of the viscous details in the layers. This allows determining a core solution a priori without knowing details of the viscous flow in the layers. Later the viscous flow in the boundary and internal layers is reconstructed. The wall conductance ratio used in the present calculations as a reference value is $c = 0.05$.

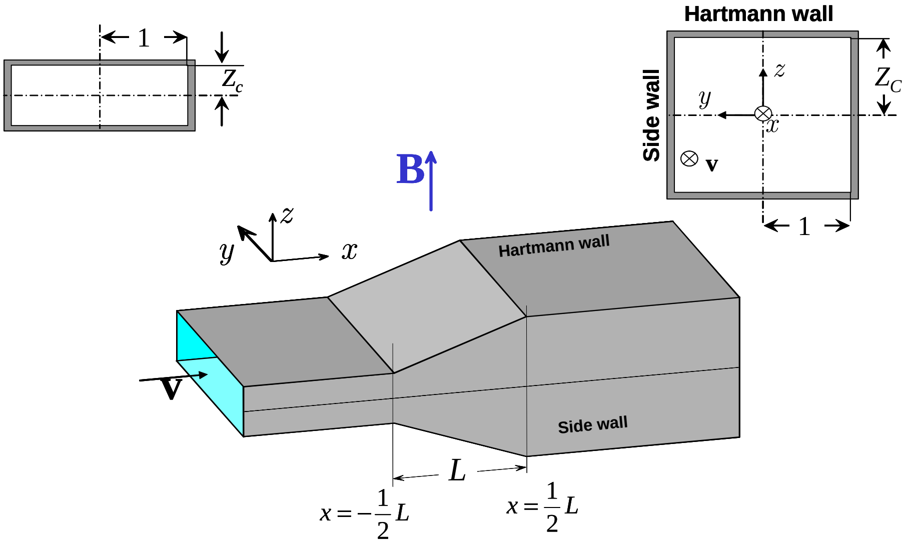

Figure 5: Sketch of an expansion. The expansion ratio is defined as Z_C/Z_c.

3.1 Core flow

MHD flows in expansions have been calculated by a combined asymptotic numeric approach for $N \to \infty$ and $c \gg Ha^{-1/2}$. The variation of pressure along the axis of the duct is shown in Fig.6. We observe the fully established MHD flow with uniform pressure gradients in both the large and the small duct at some distance from the expansion region. Fully developed conditions in ducts with $c \gg Ha^{-1/2}$ establish flow rates Q_c and Q_s, in the core and in the side layers, according to Tillack and McCarthy (1989). In the present notation these flow rates in a quarter of the duct $(y, z > 0)$ read as

$$Q_c = -\left(1 + c^{-1}Z\right) Z\, \partial_x p, \quad Q_s = -\frac{1}{3c} Z^3 \partial_x p. \tag{28}$$

In accordance with the velocity scale introduced at the beginning, where u_0 was the average velocity in the reference cross section, the total flow carried in a quarter of the duct is $Q = Q_c + Q_s = 1$. Therefore, the fully developed flow in a rectangular duct with vertical extension Z has a pressure gradient according to

$$\partial_x p = -\frac{1}{Z} \frac{\frac{c}{Z}}{1 + \frac{c}{Z} + \frac{1}{3}Z} \,. \tag{29}$$

Both (assumed) fully developed pressure distributions in the small and the large duct are indicated by the dashed straight lines in Fig. 6, which displays the pressure variation along the axial coordinate for different expansion lengths. It can be seen that the computational domain is sufficiently long that the flow can reach fully established conditions at the entrance and at the exit (see also Fig. 7a). The parametric study for the influence of different L shows, as expected, the smallest pressure drop in case of long expansions. The total pressure drop increases as the expansion length decreases, when the geometry of a sudden expansion is approached.

The axial component of pressure gradient along the axis is shown in Fig. 7a. The analytically known fully established conditions are approached perfectly after a distance of about three

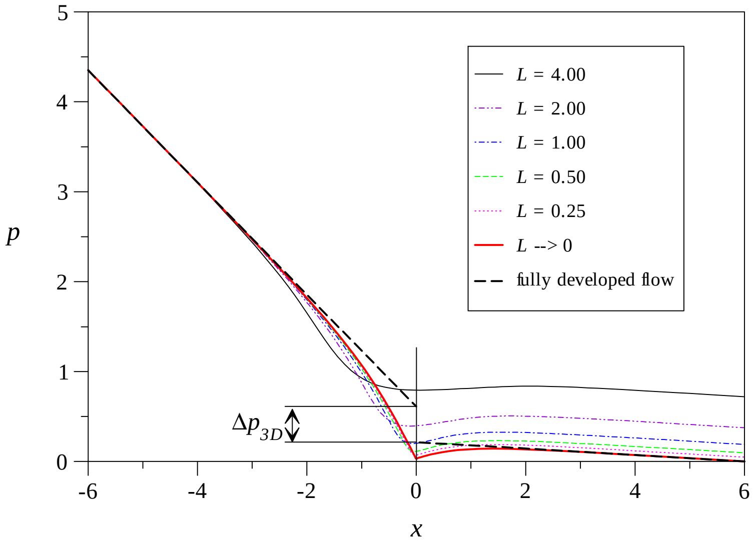

Figure 6: Pressure along the axis of the duct for different L and $c = 0.05$, $Ha = \infty$.

characteristic lengths upstream and downstream from the expansion region. The solutions exhibit a stronger pressure gradient when approaching the expansion. Within the expansion the magnitude of pressure gradient increases and near the end of the expansion and in the square duct a partial pressure recovery can be observed.

The parametric study shows further that the solution for pressure gradient develops a singularity near $x = 0$. The pressure gradient becomes discontinuous with a finite jump at $x = 0$ for infinitesimally small L. Figure 7b summarizes these results and shows clearly the different values of pressure gradient at $x = -0$ and $x = +0$ for a sudden expansion. Associated with a discontinuous pressure gradient is a discontinuity in transverse current density and velocity. Such non-physical discontinuities are a direct consequence of neglecting viscosity within the expansion layer. The viscous expansion layer becomes important for short expansion lengths, i.e. for $L \lesssim O\left(Ha^{-1/2}\right)$. A viscous solution within the expansion layer will smoothly match the solutions in both cores near $x = 0$. This point will be discussed later in more detail in Sect. 3.4.

An explanation for the observed phenomena, especially for the pressure recovery for $x > 0$, may be obtained by considering Fig. 8. In the small duct the average axial velocity $\bar{u}\left(x < -\frac{1}{2}L\right) = 1/Z_c$ is higher than the average velocity in the large duct $\bar{u}\left(x > \frac{1}{2}L\right) = 1$, due to mass conservation. As a result the induced electric field $\mathbf{v} \times \mathbf{B}$ in fully established flow is higher for the small duct, indicated in the figure by $\oplus \oplus \oplus$ and $\ominus \ominus \ominus$ in comparison with the smaller values in the large duct shown by $\oplus$ and $\ominus$. The resulting axial potential difference drives electric currents along the walls (inside the wall, but also in the fluid). Axial currents are present only for 3D flows and these extra currents are therefore called the 3D currents. These latter close their circuit through the fluid cores as shown in the sketch. In these regions the 3D currents have a transverse y component that causes additional Lorentz forces, which oppose the flow for $x < 0$ but accelerate it for $x > 0$. In the small duct, part of the mechanical energy is converted into electric energy. This energy extraction from the flow results in higher pressure drop in front of the expansion. A significant part of the electric energy is irreversibly dissipated by Ohmic heating (resulting in the 3D pressure drop Δp_{3D}), but some fraction is reconverted

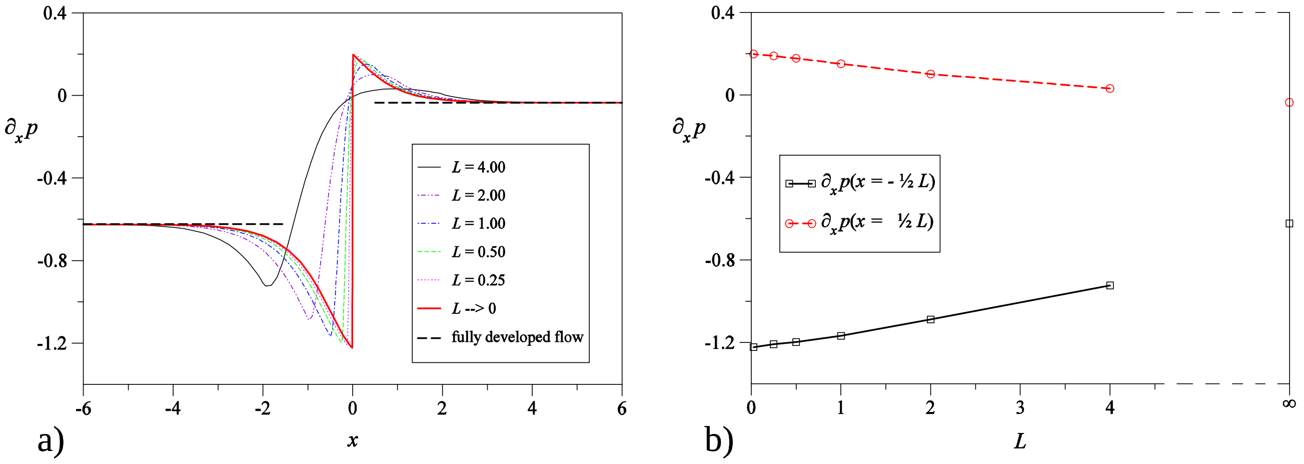

Figure 7: Axial component of pressure gradient along the axis (a) and values at the beginning and at the end of the expansion region (b) for different L and $c = 0.05$, $Ha = \infty$.

into mechanical energy for $x > 0$ as can be observed from reversed pressure gradients in Fig. 7. For very long expansions the current circuit is long and the corresponding electric resistance is high. For such conditions the additional currents and associated effects on pressure drop and flow distribution remain small. The highest 3D currents occur for a sudden expansion for which the Ohmic heating and total pressure drop reach maximum values.

Because of the presence of the strong, braking Lorentz forces the fluid tries to bypass the core at the expansion. For that reason there occurs an exchange of mass between the core and the side layers. These observations may be clarified by projecting the core mass flux as isolines of a 2D streamfunction on a plane perpendicular to the applied magnetic field. This streamfunction is defined as

$$\psi(x, y) = -\int_0^y \int_0^Z u \, dz \, dy \tag{30}$$

and core streamlines (isolines of ψ) are shown in Fig. 9 for the whole family of expansions investigated. The horizontal components of core velocity are related to ψ as

$$u_c = -\frac{1}{Z}\partial_y \psi, \quad v_c = \frac{1}{Z}\partial_x \psi. \tag{31}$$

The fluid which leaves the upstream core is collected by side layers close to the lateral walls $y = \pm 1$ and redistributed into the downstream core. The displacement of mass is favoured in addition by the Lorentz forces pointing to the sides, created by the 3D currents (compare Fig. 8). These forces push the fluid towards the side walls and support actively the exchange of mass between core and side layers. The regions over which the duct expands are indicated in Fig 9 by the red lines. The exchange of mass with the sides intensifies as L decreases. For very short expansions, as $L \to 0$, the singular behavior becomes visible by the formation of a thin *expansion layer* at $x = 0$, which is fed by the upstream core. This thin internal parallel layer forms along the expansion wall and it spreads along magnetic field lines through the whole cross section. Only a small fraction of the flow crosses the expansion layer. The major part flows

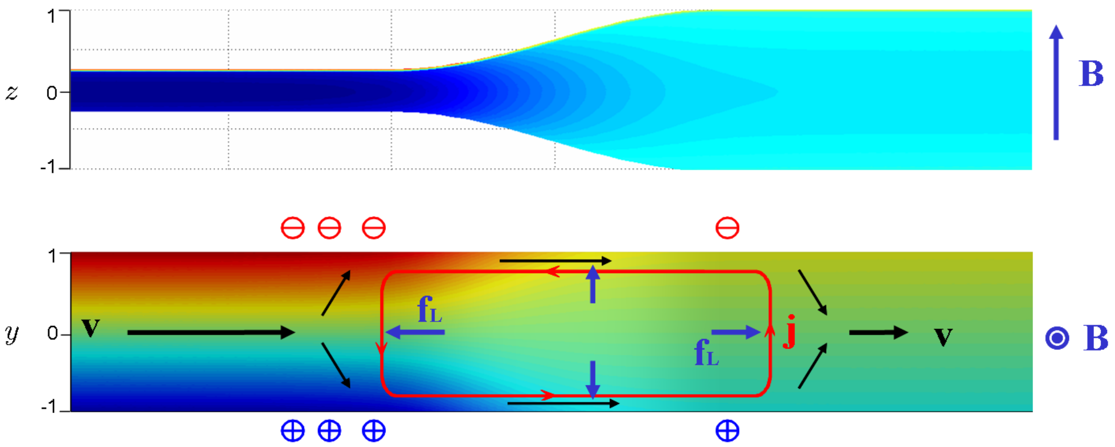

Figure 8: Sketch for explaining 3D effects in expanding MHD flows. The color indicates the magnitude of electric potential.

within the expansion layer towards the sides where it increases the side layer mass flux. Similar parallel layers, also known as *Ludford layers,* have been identified e.g. by Hunt and Leibovich (1967) for the case of 2D expansions.

Figure 10a shows the fraction of flow which is carried by the side layers. Far upstream and downstream we recover the side layer flow rate of a fully established MHD flow in conducting ducts. The fraction of flow carried by the side layers for fully developed conditions becomes with (28) and (29)

$$Q_s = \frac{\frac{1}{3}Z}{1+\frac{c}{Z}+\frac{1}{3}Z}\ . \tag{32}$$

A comparison of the numerically obtained values with the latter formula shows errors which are smaller than 2×10^{-4} for the discretization used. Approaching the expansion, the side layer flux increases continuously due to the braking of the core flow in front of the expansion caused by opposing Lorentz forces. Within the expansion region the side layer flux increases further to reach a maximum value before it decreases downstream to approach the fully established condition. As discussed already above, 3D effects become more significant for smaller L. In the limit of a sudden expansion, the side layer flow rate becomes discontinuous at $x = 0$. The discontinuity is caused by the flow that is supplied to the side layer by the expansion layer located at $x = 0$. Immediately behind the expansion nearly 80% of the flow is carried by the side layer. This flow rate reduces monotonically to about 24.5% which is the known value of a fully developed flow in electrically conducting square ducts according to (32). The side layer flow rates immediately in front and behind the expansion are displayed in Fig. 10b to show the limiting values as $L \to 0$ and the amount transferred from the core towards the sides.

The flow quantities discussed above, especially the flow rates carried by the side layers are difficult to determine experimentally. However, since flow rates are directly related to wall potentials it is useful to display this information in Fig. 11. The figure shows isolines of wall potential on the side wall and on the top or the bottom wall for the MHD flow through a sudden expansion. A comparison with the core streamfunction plotted in Fig. 9 shows that the

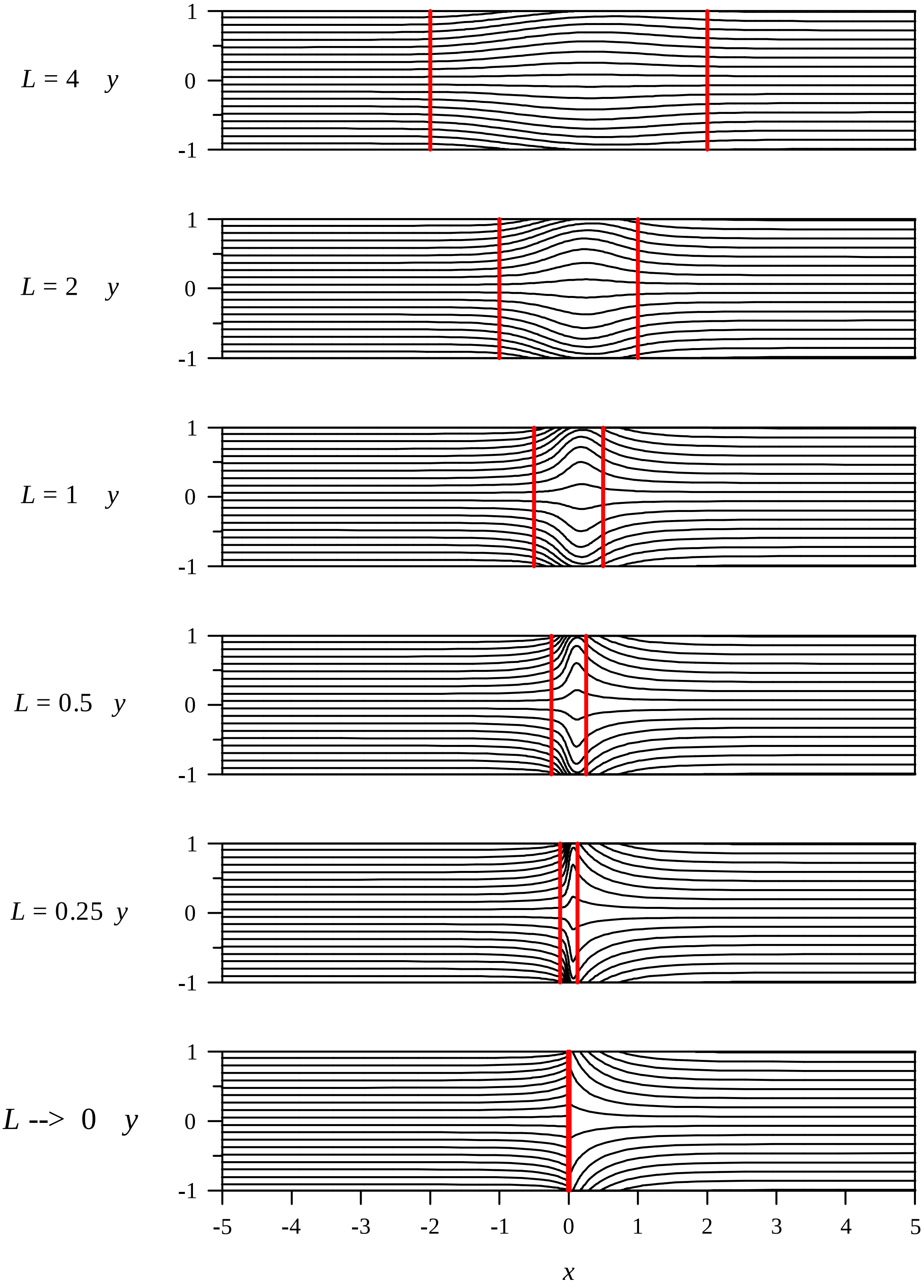

Figure 9: Streamlines for different lengths L of the expanding section.

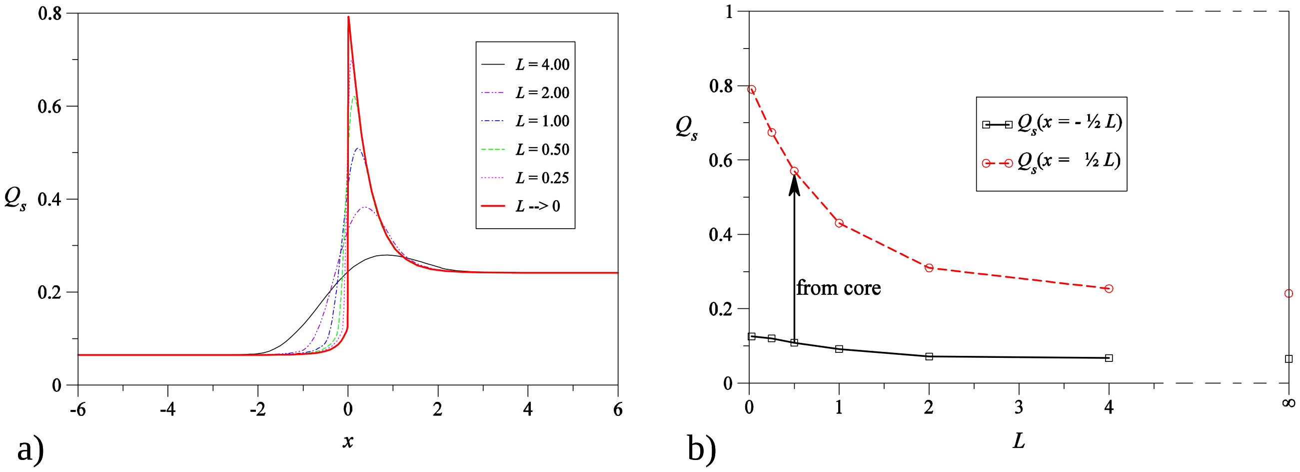

Figure 10: Fraction $Q_s(x)$ of flow carried by the side layer (a) and values Q_s at the beginning and at the end of the expansion region (b) for different L and $c = 0.05$, $Ha = \infty$. The arrow indicates the amount transferred from the core towards the side layer.

potential on the Hartmann wall may serve, after appropriate scaling (different scales in small and large duct), as an approximate streamfunction for visualizing the core flow. This means that potential measurements which are taken at the Hartmann wall measure directly flow properties like streamfunction or velocity. The reason becomes obvious if we consider Ohm's law (15). Both variables, velocity and potential, are of the order unity while currents are as small as the order of c in fully developed flows or of the order $c^{1/2}$ in 3D flows (Walker (1986a)). Neglecting the currents yields

$$u \approx -\partial_y \phi, \quad v \approx \partial_x \phi, \tag{33}$$

and we see by comparison with (31) that $\psi \approx Z_C \phi$ and $\psi \approx Z_c \phi$ in the large and in the small duct, respectively. Since the potential does not vary along magnetic field lines its isolines plotted on the top and bottom Hartmann walls give a perfect picture of the flow inside the duct, as used later in the experiments.

Finally, the influence of wall conductivity and expansion ratio on the 3D pressure drop has been analyzed in more detail (see Bühler (2007)). The 3D pressure drop Δp_{3D} has been evaluated for various values of c and a fixed expansion ratio $Z_C/Z_c = 4$. Results are summarized in Fig. 12a. For highly conducting walls the 3D pressure drop becomes very small and vanishes as $c \to \infty$. This is not surprising, since the potential difference across the small and the large duct disappears already in fully developed flows so that there is no reason for an axial potential difference at the expansion. With vanishing axial potential gradient 3D currents are not present anymore and the 3D pressure drop disappears. On the other hand, as c becomes small, values of ϕ at the side walls in the small and the large ducts asymptote towards finite values. This yields a unique potential distribution as $c \to 0$. The 3D currents are determined by this potential distribution but they depend in addition on the conductivity of the walls. Reduced conductivity of the walls leads to decreased 3D currents and pressure drop. The maximum of the 3D pressure drop is observed for c near 0.1. A similar behavior was observed also for the MHD flow in a U−bend as discussed by Molokov and Bühler (1994).

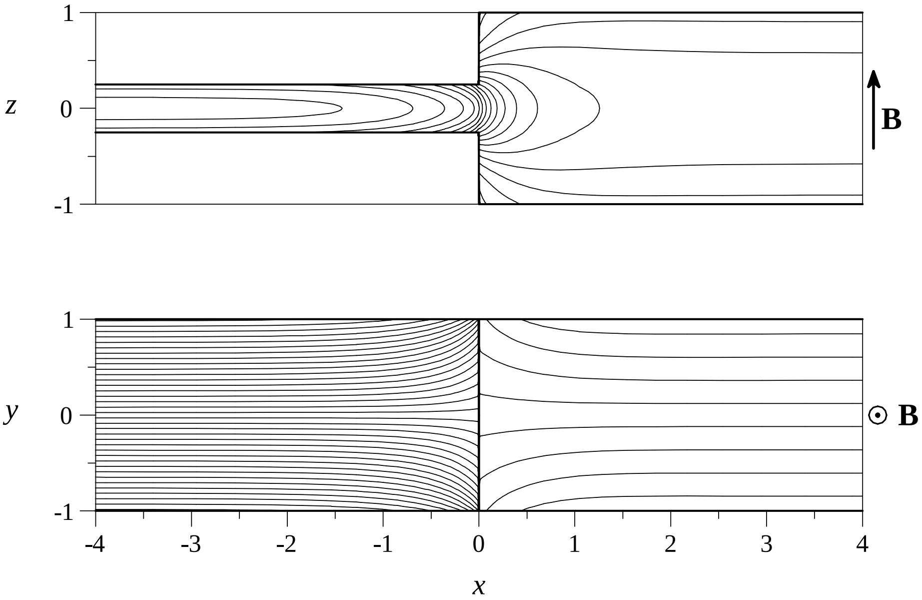

Figure 11: Isolines of wall potential on the side wall and on the top or the bottom wall. The potential difference between two isolines is 0.175.

Results for Δp_{3D} as a function of the expansion ratio are shown for a fixed wall conductance in Fig. 12b. We observe an almost linear increase of Δp_{3D} with increasing expansion ratio. Only for lower values like $Z_C/Z_c \lesssim 2$ some smaller deviations from this linear behavior exist. The observed linear relationship of Δp_{3D} for higher expansion ratio can be explained by the linear increase of the average velocity in the smaller duct. Higher velocities are associated with higher transverse potential differences in the small duct, which leads to increasing axial potential gradients, higher 3D currents and additional pressure drop Δp_{3D}.

So far we considered integral properties of the flow. Details such as velocity profiles in the side layers or in the expansion layer will be addressed in the next sections in which asymptotic techniques are used to reconstruct the flow in those layers.

3.2 Hartmann layers

We derived in the previous section inviscid solutions which are valid almost everywhere in the fluid region but require modification in viscous layers. These layers are the Hartmann layers, the side layers and the internal layers if present. We start the analysis here for the simplest case of a Hartmann layer. In a second step we consider the side layers and finally for the example of a sudden expansion we investigate flow properties in the expansion layer.

Hartmann layers occur at walls at which the magnetic field has a normal component. As already mentioned, p and ϕ are constant across the Hartmann layers up to the order $O\left(Ha^{-2}\right)$ if the magnetic field is perpendicular to the wall (Moreau (1990)) or $O\left(Ha^{-1}\right)$ if the magnetic field has a normal and a tangential component to the wall. It is further known that the tangential velocity components satisfy the no-slip condition at the wall through an exponential decay. The

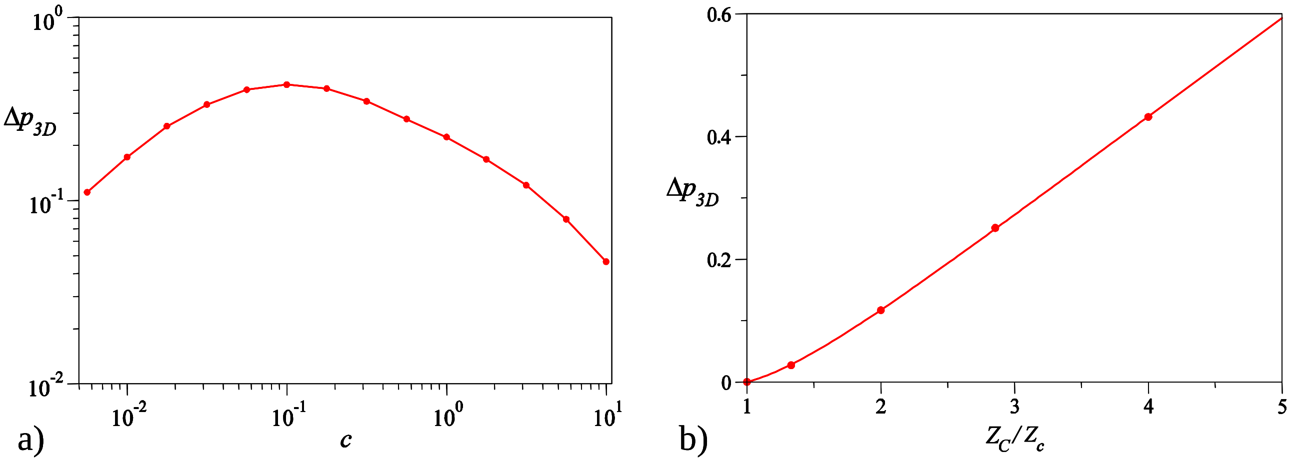

Figure 12: Three-dimensional pressure drop Δp_{3D} as a function of the wall conductance ratio c for $Z_C/Z_c = 4$ (a) and as a function of expansion ratio Z_C/Z_c with $c = 0.05$ (b) for $Ha = \infty$.

velocity in the layer is given by

$$\mathbf{v} = \mathbf{v}_c \left(1 - \exp\left(-n\right)\right), \tag{34}$$

where $\mathbf{v}_c$ is the inviscid or core solution. The variable n is the local coordinate along the inward unit normal $\mathbf{n}$, scaled by the local thickness of the Hartmann layer which is in general $\delta_H = \left(Ha \left|\mathbf{n} \cdot \mathbf{B}\right|\right)^{-1}$ and for the present case $\delta_H = Ha^{-1}$. All these properties are already implemented in the numerical method used here and need not to be discussed in more detail. For further information about the treatment of Hartmann layers in the asymptotic code see Bühler (1995).

3.3 Side layers

3.3.1 Potential and axial velocity

At walls which are exactly aligned with the magnetic field we find a second type of boundary layer. The asymptotic numerical code used above takes this layer into account in the sense that its integral properties are preserved. Especially the mass flux carried by the layer and the electric potential at the side wall is calculated precisely if the conductivity of the side wall is much higher than the conductivity of the parallel layer, i.e. when $c \gg Ha^{-1/2}$. The velocity in the layer, however, has to be reconstructed in a subsequent step from the integral quantities via a boundary layer analysis.

Let us suppose that an inviscid solution to the problem is known. We know core potentials and core velocities close to the side walls. Then we are able to derive asymptotic equations which govern the viscous flow in the side layer. For this purpose we introduce a stretched side layer coordinate in the equation for potential (20), e.g. in the layer at $y = -1$ such that

$$y + 1 = \delta_S \eta, \tag{35}$$

where δ_S stands for the thickness of the side layer (see Fig. 13). A reasonable balance of viscous and Lorentz forces requires that $\delta_S = Ha^{-1/2}$ and we find at leading order of the analysis the equation governing the potential in the side layer,

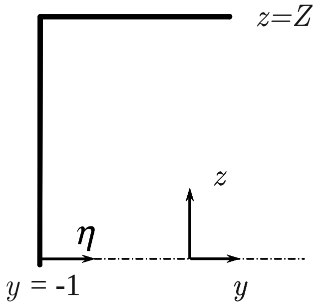

Figure 13: Stretched coordinate in the side layer at $y = -1$.

$$\partial_\eta^4 \phi = \partial_{zz}\phi. \tag{36}$$

We decompose the potential as $\phi = \phi_c + \phi_s$, into an inviscid core solution ϕ_c that does not vary across the viscous side layer plus a viscous side layer correction $\phi_s(\eta, z)$. It can be shown that the thin wall condition (11) at Hartmann walls, formulated in stretched side layer coordinates

$$\partial_z \phi = c\,(\partial_{xx}\phi + \partial_{yy}\phi) \approx cHa\,\partial_{\eta\eta}\phi \quad \text{at} \quad z = Z \tag{37}$$

results in a uniform potential along the stretched direction, i.e. the Hartmann wall acts as a perfect conductor in this direction, if $c\,Ha \gg 1$. For that reason the potential equals the core potential at the Hartmann wall and the viscous correction ϕ_s vanishes at $z = \pm Z$. As $\eta \to \infty$ the solution must match the core solution, which is equivalent to the requirement that viscous corrections to the core potential vanish (see also Walker (1981)).

Equation (36) has the z-symmetric solution that does not grow indefinitely as $\eta \to \infty$:

$$\phi_s = \sum_{k=0}^{\infty} (a_k \cos \alpha_k \eta + b_k \sin \alpha_k \eta) \exp \alpha_k \eta \, \cos \beta_k z, \tag{38}$$

where

$$\beta_k = \frac{2k+1}{2}\frac{\pi}{Z}, \quad \alpha_k = -\sqrt{\beta_k / 2}. \tag{39}$$

In the next step we decompose the velocity as $u = u_c + u_s$, where u_c and u_s stand for the core velocity and the viscous correction in the side layer. Introduced into Ohm's law (3), the viscous correction for velocity in the side layer is evaluated at this order of approximation according to

$$\begin{aligned} u_s &= -Ha^{1/2}\partial_\eta \phi_s \\ &= -\sum_{k=0}^{\infty} Ha^{1/2}\alpha_k \left[(b_k + a_k)\cos\alpha_k\eta + (b_k - a_k)\sin\alpha_k\eta\right] \exp\alpha_k\eta \, \cos\beta_k z. \end{aligned} \tag{40}$$

Boundary conditions $\phi = \phi_w$ and $u = 0$ provide matching conditions at the side wall $\eta = 0$ for determining the unknown coefficients a_k and b_k from

$$\left.\begin{aligned} \phi_w = \phi_c + \phi_s &= \qquad \phi_c + \sum a_k \cos \beta_K z \\ 0 = u_c + u_s &= \quad u_c - \sum \underbrace{Ha^{1/2}\alpha_k\,(b_k + a_k)}_{u_k} \cos \beta_k z \end{aligned}\right\} \text{ at } \eta = 0. \tag{41}$$

The coefficients a_k and u_k correspond to the Fourier coefficients of viscous potential and velocity taken at the position $y = -1$ ($\eta = 0$). Details about their determination by using orthogonality of trigonometric functions can be found in the appendix. Once a_k and u_k are known it is straightforward to determine b_k.

The axial component of wall shear stress or skin friction is obtained by differentiation of axial velocity at the wall with respect to the wall-normal coordinate y, or here with respect to η, as

$$\tau_x = -Ha \sum_{k=0}^{\infty} \beta_k b_k \cos \beta_k z.$$

Results for electric potential on the wall are shown as colored contours on the surface of an expansion, and velocity profiles at three different axial positions are displayed in Figs. 14-15 for $Ha = 10^3$. Far downstream and upstream of the expansion we observe the typical velocity profiles of fully established rectangular duct flows with a flat uniform core and high-velocity jets along the side walls. Approaching the expansion the core becomes deformed. In the center of the core the velocity is reduced and closer to the sides it is increased. In addition the flux carried by the viscous side layer increases due to the exchange of flow with the core. This leads to higher velocities in the side layers close to the expansion as can be observed from the figures.

With decreasing expansion length the 3D effects become stronger. The velocity in the core is progressively reduced and the side layer flux increases as L reduces. The strongest effects are observed for a sudden expansion ($L \to 0$). Immediately behind the expansion, as shown in Fig. 15, the major fraction of the flow is carried by the side layers, which have received from the flow upstream the expansion and from the expansion layer about 80% of the total flux. The velocity profile in side layers is no longer parabolic along field lines as known for fully developed flows. There exists even a reversed flow closer to the outer corners of the duct. The back flow disappears downstream after some length and the fluid finally approaches fully developed conditions at the exit of the computational domain.

3.3.2 Vertical velocity

For deriving an equation for vertical velocity in the side layer we use (24) in stretched side layer coordinates as

$$\partial_\eta^4 w = \partial_{zz} w. \tag{42}$$

No-slip at the wall and the fact that the viscous corrections vanish in the core requires that

$$v = w = 0 \text{ at } \eta = 0 \text{ and } w = \partial_\eta w = 0 \text{ as } \eta \to \infty. \tag{43}$$

The boundary conditions at Hartmann walls and symmetry imply that

$$w = 0 \text{ at } z = Z \text{ and at } z = 0. \tag{44}$$

By separation of variables we find a viscous solution for w, which vanishes at large distance from the side wall and which satisfies no-slip at the wall in the form of

$$w = Ha^{1/2} \sum_{k=1}^{\infty} w_k \sin \alpha_k \eta \, \exp \alpha_k \eta \, \sin \beta_k z, \tag{45}$$

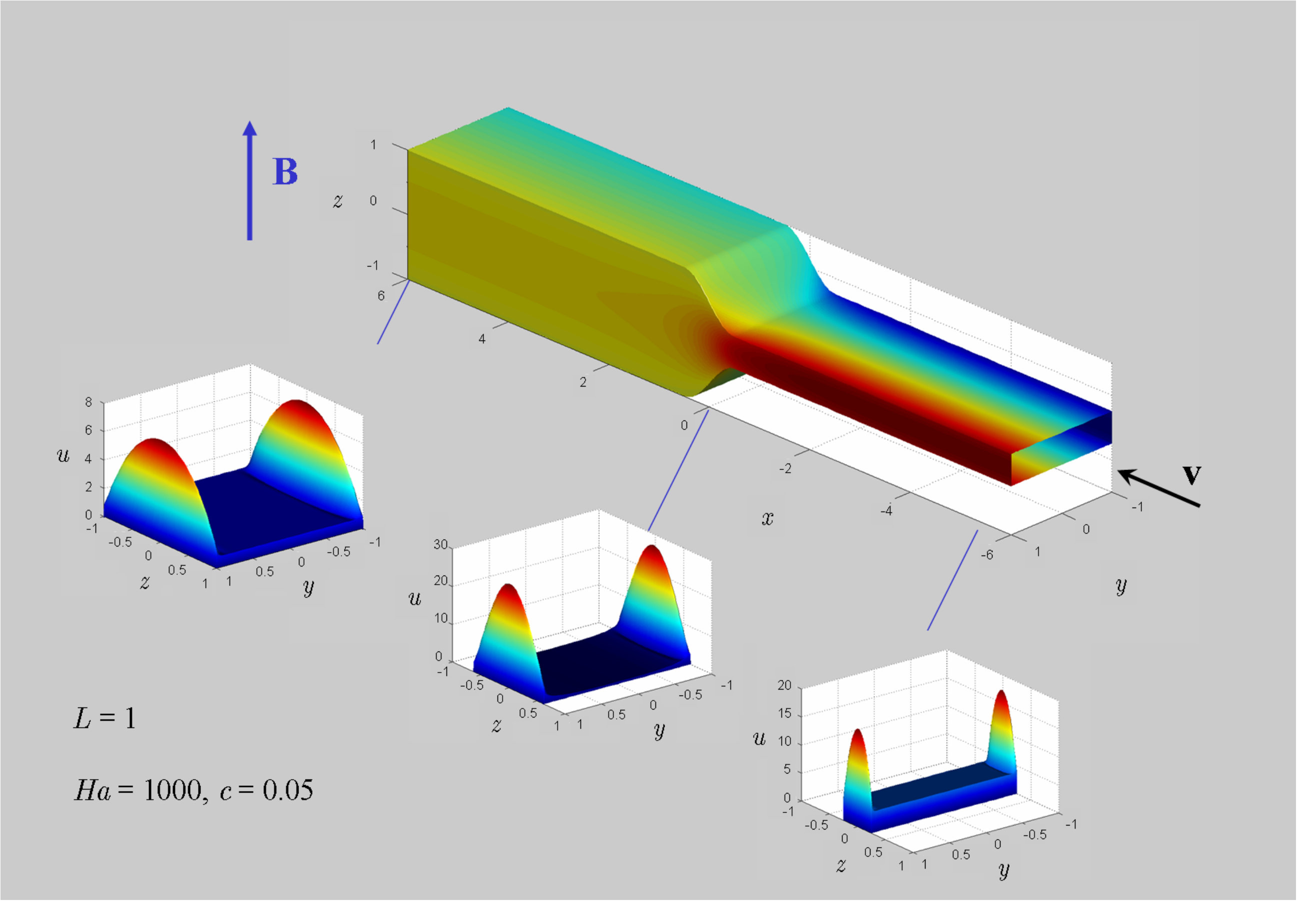

Figure 14: Contours of potential shown on the surface of a smooth expansion for $Ha = 1000$, $c = 0.05$, $L = 1$. Axial velocity profiles upstream ($x < 0$), at the expansion ($x = 0$) and downstream ($x > 0$).

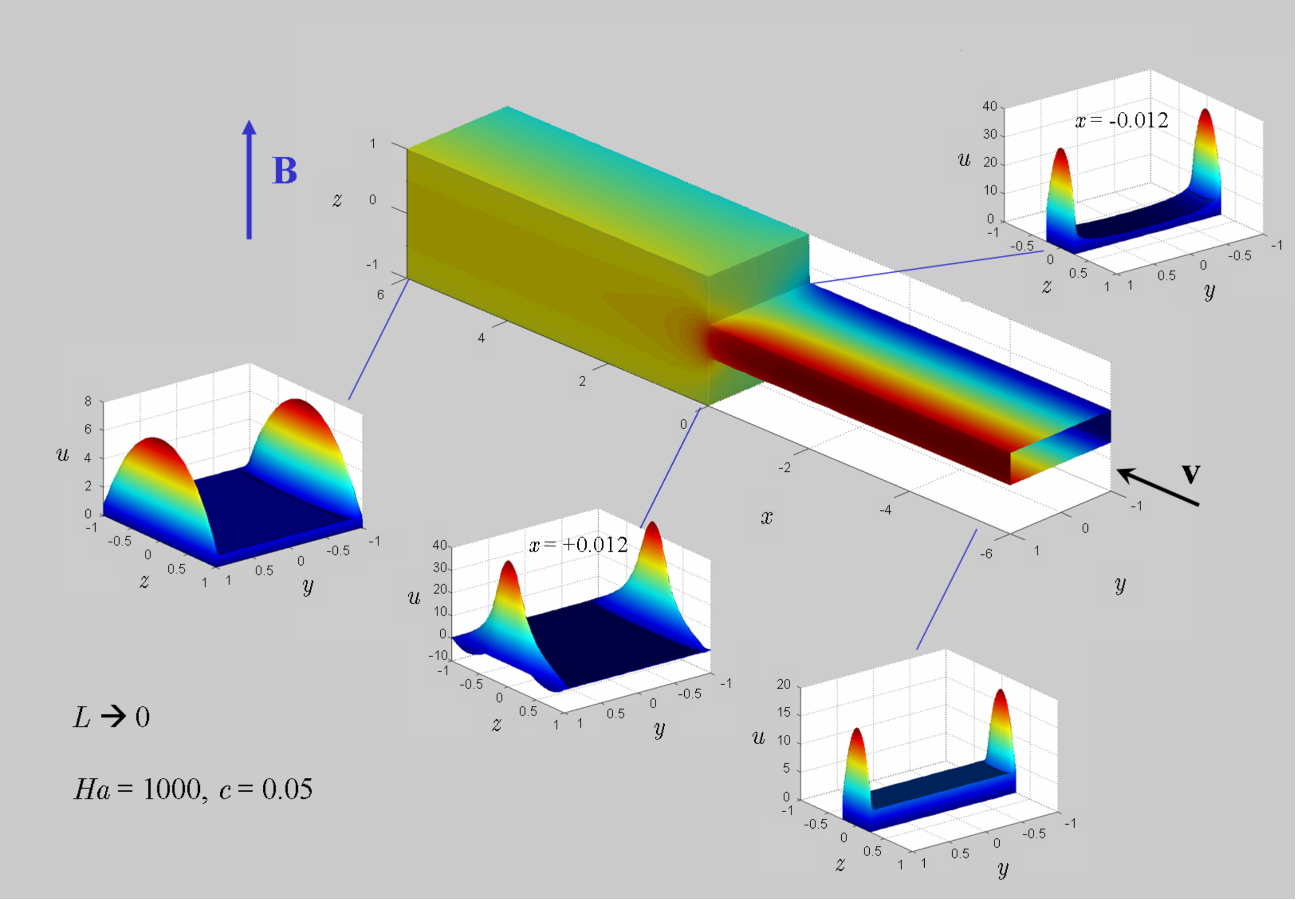

Figure 15: Contours of potential shown on the surface of a sudden expansion for $Ha = 1000$, $c = 0.05$, $L \to 0$. Axial velocity profiles upstream ($x < 0$), close to the expansion ($x = \pm 0.012$) and downstream ($x > 0$).

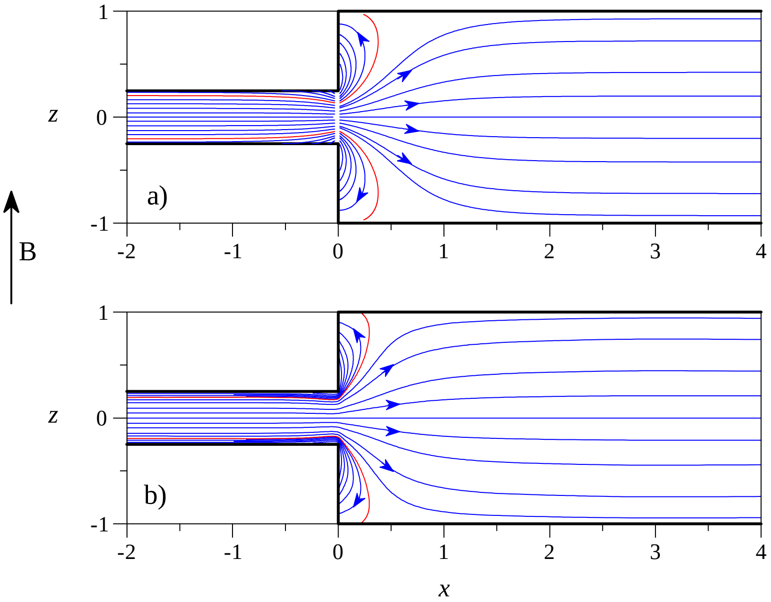

Figure 16: Limiting streamlines at the side wall for $Ha = 1000$, $c = 0.05$. Comparison of asymptotic theory for $N = \infty$ (a) with numerical simulations at $N = 10^5$ (b).

where as a scale for the order of magnitude of side layer velocity the factor $Ha^{1/2}$ has been introduced and

$$\beta_k = k\frac{\pi}{Z}, \qquad \alpha_k = -\sqrt{\beta_k/2}. \tag{46}$$

The evaluation of the coefficients w_k is outlined in the appendix.

The vertical component of wall shear stress is obtained by differentiation of vertical velocity at the wall with respect to the wall-normal coordinate y or here with respect to η to yield

$$\tau_z = Ha \sum_{k=1}^{\infty} \alpha_k w_k \sin \beta_k z. \tag{47}$$

3.3.3 Limiting streamlines

For visualization of the flow it is illustrating to show the tangential velocity close to the wall. This may be done by plotting so-called *limiting streamlines* along a surface whose distance from the wall vanishes. They may be obtained directly from skin friction (Délery (2001)) and at the side walls $y = \pm 1$ they are defined as

$$\frac{dx}{\tau_x} = \frac{dz}{\tau_z}. \tag{48}$$

With the knowledge of wall shear stress components τ_x and τ_z it is now possible to show a complete picture of limiting streamlines on the side wall as displayed in Fig. 16a. A comparison with those obtained by numerical simulations (b) at large but finite interaction parameter shows that the asymptotic theory yields quite good results and constitute therefore an efficient mean for reconstruction of viscous solutions in parallel layers.

When approaching the expansion, the flow close to the side wall converges slightly towards the symmetry plane $z = 0$. The reason for that lies in the fact that the core with a uniform velocity profile along field lines (along z) exchanges fluid with the side layer, in which the axial velocity profile exhibits rather a parabolic distribution along z with reduced flux close the Hartmann walls. This forces the fluid to move from regions near the Hartmann walls towards places closer to the symmetry plane.

For $x > 0$ the side layer flow expands into the larger duct, creating there regions of reversed flow. The backward streamlines that end at the expansion wall indicate that there exists an exchange of flow with the expansion layer that will be considered in more detail in the next subsection. The expansion layer is fed by fluid from the side layer in regions $|z| \gtrsim 0.4$. This picture indicates clearly the axial extension of the fluid domain that is involved in the recirculating motion. The reversed flow was already visible in Fig. 15 showing an axial velocity profile immediately behind the expansion at $x = 0.012$. It should be noted that the back-flow region indicated in the figure is present only very close to the side wall. At some distance from the side wall the sign of velocity reverses and the back-flow disappears.

3.4 Expansion layer

Expansion layers occur if $L \lesssim Ha^{-1/2}$ as in the case of a sudden expansion. In the analysis we use the same ideas as for the solution of the side layer problem. Let us suppose that an inviscid solution to the problem is known, i.e. we know core potentials and velocities upstream and downstream of a sudden expansion, and the wall potential along the expansion wall.

3.4.1 Potential and transverse velocity

Since the expansion layer is very thin we introduce a stretched axial coordinate in (20) for the layer such that

$$x = \delta_e \xi, \tag{49}$$

where δ_e stands for the thickness of the expansion layer. A reasonable balance of viscous and Lorentz forces requires that $\delta_e = Ha^{-1/2}$ and we find at leading order of our analysis the equation governing the potential in the expansion layer,

$$\partial_\xi^4 \phi = \partial_{zz} \phi. \tag{50}$$

The separable partial differential equation (50) is solved on the domain shown in Fig. 17, assuming symmetry with respect to $z = 0$. As already discussed for the side layers, the thin wall condition (11) formulated in stretched coordinates results in a uniform potential along the stretched direction, i.e. the Hartmann walls act here as perfect conductors along the axial direction if $c\,Ha \gg 1$. For that reason the potential equals the core potential at the Hartmann walls and the viscous corrections vanish at these walls. As $\xi \to \pm\infty$ the solution must match the core solution which is equivalent to the requirement that viscous corrections to the core potential and velocity vanish as $\xi \to \pm\infty$. In addition the potential along the vertical expansion wall equals the wall potential and the velocity vanishes along this wall at $\xi = 0$. For the solution we split the domain into two parts, one for $\xi < 0$, in which the duct has a dimension along magnetic field lines up to $Z(\xi) = Z_c$ and a second part for $\xi \geq 0$ where $Z(\xi) = Z_C = 1$.

Let us start the analysis for $\xi \geq 0$. We decompose the potential as $\phi = \phi_C + \phi_E$, into an inviscid core solution ϕ_C and into a viscous correction ϕ_E. Similarly we decompose the velocity

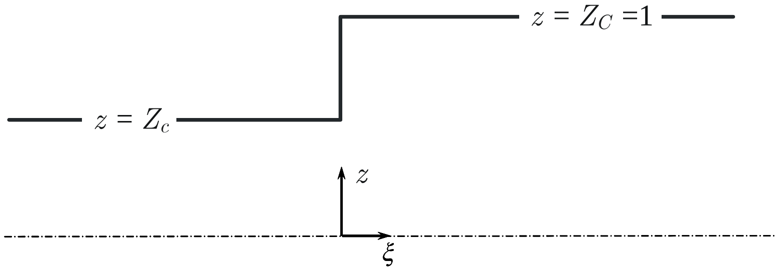

Figure 17: Coordinates and geometry in the upper half of the expansion layer.

as $v = v_C + v_E$, where v_C and v_E stand for the transverse core velocity and the viscous correction in the expansion layer.

Equation (50) has the z- symmetric solution that does not grow indefinitely as $\xi \to \infty$:

$$\phi_E = \sum_{K=0}^{\infty} (A_K \cos \alpha_K \xi + B_K \sin \alpha_K \xi) \exp \alpha_K \xi \, \cos \beta_K z, \tag{51}$$

where

$$\beta_K = \frac{2K+1}{2} \frac{\pi}{Z_C}, \quad \alpha_K = -\sqrt{\beta_K / 2}. \tag{52}$$

The transverse velocity in the layer is related at this order of approximation to the potential as

$$v_E = Ha^{1/2} \partial_\xi \phi_E =$$

$$= \sum_{K=0}^{\infty} Ha^{1/2} \alpha_K \left[(B_K + A_K) \cos \alpha_K \xi + (B_K - A_K) \sin \alpha_K \xi \right] \exp \alpha_K \xi \, \cos \beta_K z. \tag{53}$$

Potential and velocity at $\xi = 0$ are later used to determine the unknown coefficients A_K and B_K by using

$$\left. \begin{aligned} \phi = \phi_C + \phi_E = & \quad \phi_C + \sum A_K \cos \beta_K z \\ v = v_C + v_E = & \quad v_C + \sum \underbrace{Ha^{1/2} \alpha_K (B_K + A_K)}_{V_K} \cos \beta_K z \end{aligned} \right\} \text{ at } \xi = 0. \tag{54}$$

The coefficients A_K and the groups V_K correspond to the Fourier coefficients of viscous potential and velocity taken at the position $\xi = 0$. While the core values are independent of the field aligned coordinate according to (26) and (27), the values ϕ and v at $\xi = 0$ do depend on z.

For $\xi < 0$ we perform a similar analysis and decompose the electric potential as $\phi = \phi_c + \phi_e$, into an inviscid core solution ϕ_c and into a viscous correction ϕ_e. Similarly we decompose the velocity as $v = v_c + v_e$, where v_c and v_e stand for the core velocity and the viscous correction in the expansion layer for $\xi < 0$. In this part of the geometry the extension of the duct along field lines is between $-Z_c < z < Z_c$.

Equation (50) has the solution that does not grow indefinitely as $\xi \to -\infty$, i.e.

$$\phi_e = \sum_{k=0}^{\infty} (a_k \cos \alpha_k \xi + b_k \sin \alpha_k \xi) \exp \alpha_k \xi \, \cos \beta_k z, \tag{55}$$

where

$$\beta_k = \frac{2k+1}{2}\frac{\pi}{Z_c}, \quad \alpha_k = +\sqrt{\beta_k/2}. \tag{56}$$

The velocity here is given by

$$\begin{aligned} v_e &= Ha^{1/2}\partial_\xi \phi_e \\ &= \sum_{k=0}^{\infty} Ha^{1/2}\alpha_k \left[(a_k + b_k)\cos\alpha_k\xi + (b_k - a_k)\sin\alpha_k\xi\right]\exp\alpha_k\xi\, \cos\beta_k z. \end{aligned} \tag{57}$$

The potential and velocity at $\xi = 0$ are represented now as

$$\left.\begin{array}{rr} \phi = \phi_c + \phi_e = & \phi_c + \sum a_k \cos\beta_k z \\ v = v_c + v_e = & v_c + \sum \underbrace{Ha^{1/2}\alpha_k\,(a_k + b_k)}_{v_k} \cos\beta_k z \end{array}\right\} \text{ at } \xi = 0\,. \tag{58}$$

By smoothly matching both representations (54) and (58) at $\xi = 0$ it is possible to evaluate the unknown coefficients A_K and B_K together with a_k and b_k as outlined in the appendix.

As a result, isolines of transverse velocity are plotted in Fig. 18 together with a velocity distribution for the expansion layer at a position close to the side wall near $y = 1$. The Hartmann number is $Ha = 1000$ for the present case. Far upstream the transverse velocity is equal to v_c. Approaching the expansion we observe a weak local minimum of the transverse velocity near $\xi \approx -1.5$. Then, the velocity increases strongly along the axis and the maximum is reached near $\xi \approx 0.7$. Later the velocity decays and approaches via a local minimum, not visible in the figure, the core value v_C. The profile of transverse velocity plotted along the duct axis is shown in Fig. 19a.

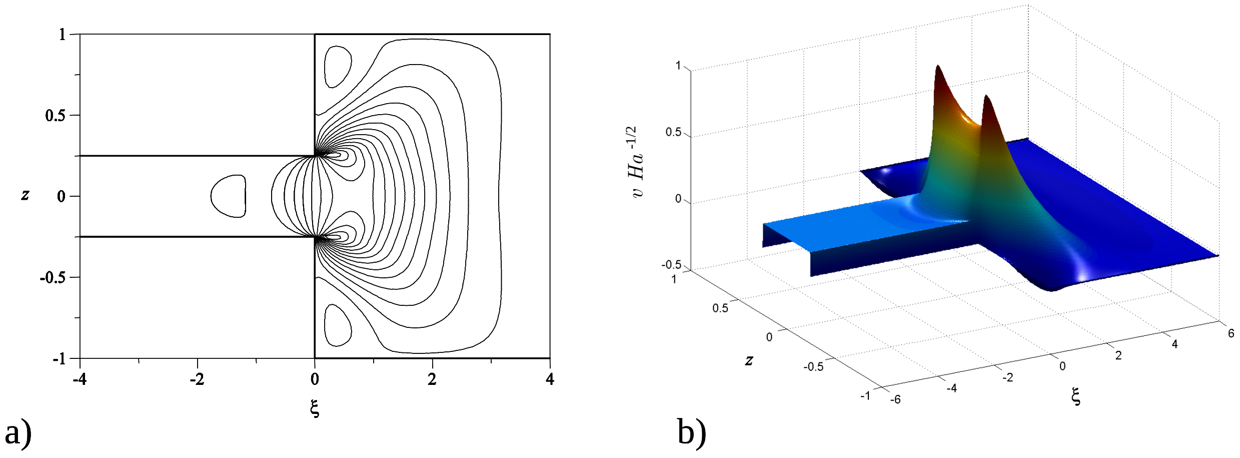

Figure 18: Isolines of transverse velocity v (a) and velocity distribution (b) in the e-layer close to the side wall $y \approx 1$ for $Ha = 1000$, displayed by using the velocity scale $v\,Ha^{-1/2}$.

The most interesting observation is that the maximum of the $e-$ layer velocity is located not on the axis at $z = 0$, as one could expect. Instead we find two maxima close to the positions $z \approx \pm Z_c$. While the major fraction of the flow in the layer is carried towards the sides, the

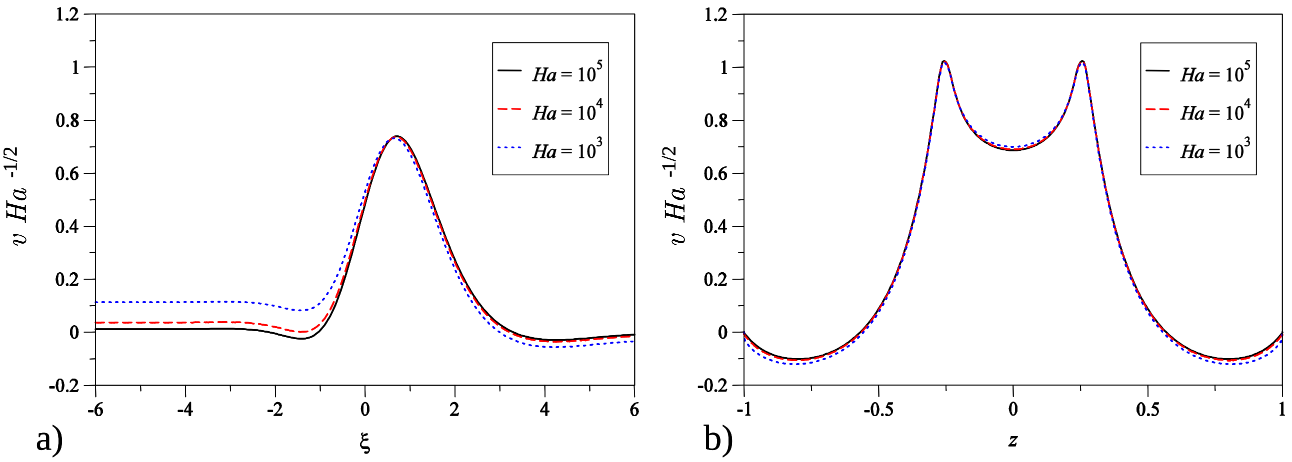

Figure 19: Transverse velocity close to the side wall $y \approx 1$, plotted along the axial direction $v\left(\xi, z=0\right)$ (a), and plotted along field lines $v\left(\xi=0.4, z\right)$ (b).

solution exhibits also regions closer to the outer corners, in which the direction of velocity is reversed. In these regions fluid is sucked from the side layer and transferred towards the center of the duct. The two maxima and the reversed flow are clearly visible in Fig. 18 and in Fig. 19b. These findings are consistent with the axial velocity profile behind the expansion as shown in Fig. 15, where near the corners zones of reversed flow are also present.

To continue the analysis let us consider integral quantities of the layer and compare them with the solutions in the cores. In general the inviscid axial mass flux is discontinuous across the expansion layer. Therefore the layer must carry an $O\left(1\right)$ flow rate transverse to the axis towards the sides. Since we are interested in the amount of flow carried by the layer at position y we integrate the velocity profile and find the local flow rate

$$q_y\left(y,z\right) = Ha^{-1/2}\left(\int_{-\infty}^{0} v_e \, d\xi + \int_{0}^{\infty} v_E \, d\xi\right) = -\Delta\phi \, .$$

with

$$\Delta\phi = \left\{ \begin{array}{c} \phi_w - \phi_C \\ \phi_c - \phi_C \end{array} \right. \text{ for } \begin{array}{c} Z_c < z < Z_C \\ 0 < \ z \le Z_c \end{array} . \tag{59}$$

The amount of fluid carried by the upper half of the e- layer at position y evaluates from the latter quantity as

$$Q_e\left(y\right) = \int_{0}^{Z_C} q_y \, dz = -\int_{0}^{Z_C} \Delta\phi \; dz. \tag{60}$$

This means that the flow rate is determined by the difference between the core potential in the large duct and the potential along the vertical wall and in the small core. It is possible to compare the potential-driven transverse flow rate with the fluxes calculated by the numerical code, i.e. $Q_e = \psi_C - \psi_c$. A comparison shows that the difference between both quantities is

$$\psi_C - \psi_c + \int_{0}^{Z_C} \Delta\phi \; dz = 0 + \varepsilon, \tag{61}$$

which is as small as the (numerical) error of the current approximation, $\varepsilon \lesssim 10^{-2}$.

3.4.2 Vertical velocity

For deriving an equation for vertical velocity in the expansion layer we use (24) in stretched coordinates as

$$\partial_\xi^4 w = \partial_{zz} w. \tag{62}$$

At large distance from the expansion viscous contributions vanish so that $w = \partial_\xi w = 0$ as $\xi \rightarrow \pm\infty$. The boundary conditions at Hartmann walls at $z = Z_c, Z_C$ are $w = 0$, and symmetry implies that $w = 0$ at $z = 0$. At the vertical wall of the expansion at $\xi = 0$, for $Z_c < z < Z_C$, we have no-slip and zero normal component of velocity, $w = 0$ and $u = 0$.

As before we split the expansion domain in two regions and define the vertical velocity as

$$w = \left\{ \begin{array}{lcl} Ha^{1/2} w_e & & \xi < 0 \\ & \text{for} & \\ Ha^{1/2} w_E & & \xi > 0\ . \end{array} \right. \tag{63}$$

By separation of variables we find viscous solutions for w, which vanish at large distance from the expansion in the form

$$w_E = \sum_{K=1}^{\infty} \left(A_K \cos \alpha_K \xi + B_K \sin \alpha_K \xi \right) \exp \alpha_K \xi \, \sin \beta_K z, \tag{64}$$

$$w_e = \sum_{k=1}^{\infty} \left(a_k \cos \alpha_k \xi + b_k \sin \alpha_k \xi \right) \exp \alpha_k \xi \, \sin \beta_k z, \tag{65}$$

where

$$\begin{array}{ll} \beta_K = \frac{1}{Z_C} K\pi, & \alpha_K = -\sqrt{\beta_K / 2}, \\ \beta_k = \frac{1}{Z_c} k\pi, & \alpha_k = \sqrt{\beta_k / 2}. \end{array} \tag{66}$$

At $\xi = 0$ we smoothly match both solutions up to the second derivatives. The fourth condition for matching is obtained by consideration of vertical fluxes. Details of the analysis can be seen in the appendix.

From the results obtained above we may evaluate the local vertical flow rate in the layer as

$$q_z(y, z) = \int_{-\infty}^{\infty} w d\xi. \tag{67}$$

Results are shown in Fig. 20. At all walls $w = 0$ is satisfied. At $y = 0$ the highest vertical velocities occur near $\xi \approx 0.62$, $z \approx 0.45$. Approaching the side wall the vertical velocity increases in magnitude. This is a result of the fact that the flow coming from the small duct has to be distributed both to the internal layer (in the transverse direction) and to the large core. The flow rate supplied to the expansion layer by the small core increases towards the sides as was shown already in Fig. 15 and therefore the magnitude of vertical velocity increases too. The flow rate carried by the layer increases also towards the sides which leads additionally to higher velocities in the layer. We observe that the location of maximum vertical velocity shifts to positions closer to the expansion, i.e. to $\xi \approx 0.45$, $z \approx 0.3$.

Profiles of vertical velocity at $\xi = 0.4$ (position indicated by the dashed lines) are displayed in Fig. 20c for different transverse positions in the duct. The vertical component of velocity scales as $Ha^{1/2}$. It shows maximum values in the range $w \sim 0.14\, Ha^{1/2}$ for $y = 0$ and $w \sim 0.5\, Ha^{1/2}$ at a position close to the side wall.

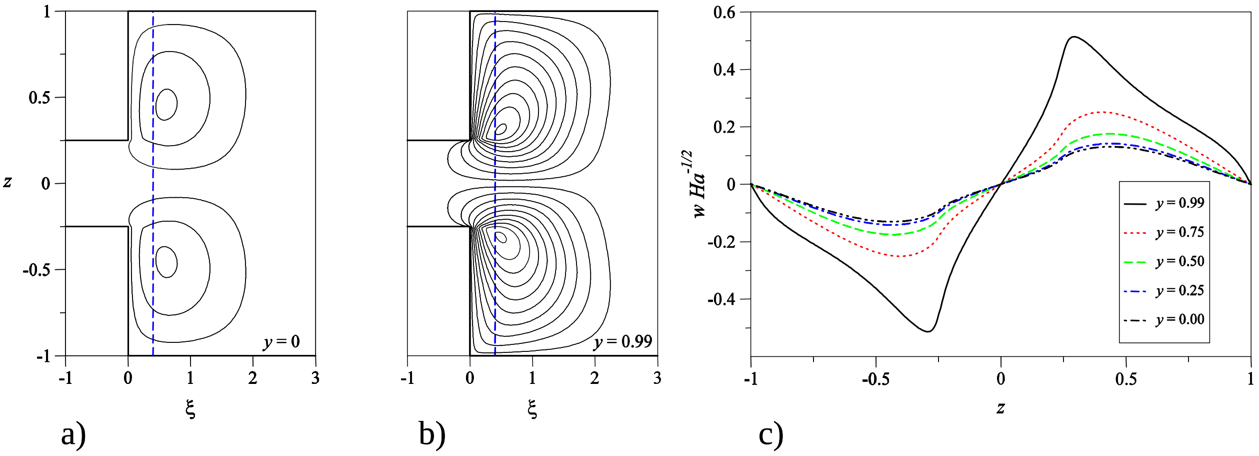

Figure 20: Contour plots of vertical velocity w in the e-layer at the symmetry plane $y = 0$ (a), close to the side wall at $y = 0.99$ (b), and profiles of w at axial position $\xi = 0.4$ (c).

3.4.3 Mass flux along the layer

In order to get an overview how the flux carried by the e- layer is distributed we consider the two-dimensional vector field $\mathbf{q} = q_y\hat{\mathbf{y}} + q_z\hat{\mathbf{z}}$ in the plane of the expansion layer as shown in Fig. 21. It can be seen how the net flux, which is collected by the layer, is distributed towards the sides of the duct. Regions of reversed flux (flux from the side towards the center) are not present. This means that the reversed velocities observed in Fig. 19 are at least compensated by a flow in opposite direction towards the sides (for larger ξ) so that no reversed net flux carried by the layer is present.

3.4.4 Flow paths

In this section we describe the main flow pattern or paths involving the cores, the side layers and the e- layer. For simplicity we restrict the discussion to one quarter of the symmetric expansion as shown in Fig. 22. We have seen already in Fig. 9 that there is an intense exchange of flow between cores, side layers and the internal layer. Before reaching the internal layer the mass flux in the side layer increases because of an exchange between upstream core and upstream side layer. When the flow approaches the expansion the side layer carries already 13% of the total flux. This flow is transferred to the downstream side layer. Possible flow paths for this fraction of flow are shown as red lines in Fig. 22, starting at positions (1) – (3).

A second type of streamline is shown in blue. These paths start in the upstream core, e.g. passing through positions (4) – (6), they enter the e- layer, and stay there until they meet the downstream side layer. This part of flow continues its path through this side layer before part of it is redistributed to the downstream core. It has been shown above that behind the expansion region the downstream side layer carries about 80% of the flow.

The streamlines shown in Fig. 9 indicate also that there exists a minor fraction of fluid (less than 20%) that is able to cross the internal layer from upstream to downstream core. Such

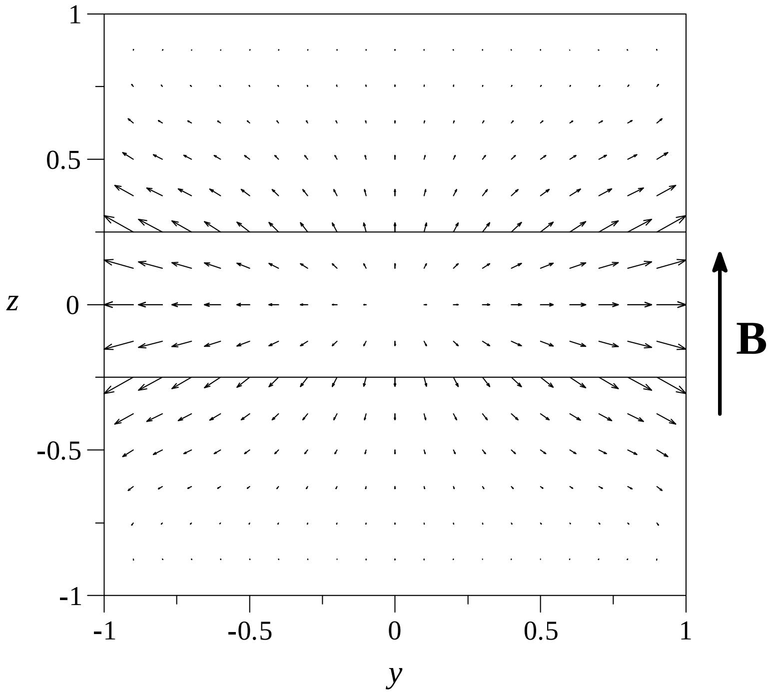

Figure 21: Vector plot of local flow rate $\mathbf{q} = q_y \hat{\mathbf{y}} + q_z \hat{\mathbf{z}}$ in the expansion layer.

a path is indicated in Fig. 22 by the green line passing through position (7). The one shown here lies just in the symmetry plane. All other lines of this type (not shown here explicitly) are shifted upwards but also towards the sides during their path across the e-layer before they reach the downstream core.

The axial velocity profile just behind the e-layer, shown in Fig. 15, exhibits regions of reversed flow in the side layers close to the corners. The transverse velocity distribution plotted in Fig. 18 and the profile in Fig. 19b show also regions of locally reversed flow. A flow path consistent with these results is drawn in magenta. A comparison with numerical predictions (shown later) or with Fig. 16 indicates that this path should originate very close to the Hartmann - side wall corner in the small duct at position (8). It should be noted that the magenta loop operates close to the walls and that streamlines of the blue type, (5) and (6), exist just at a slightly larger distance from the wall.

Further downstream the side layer is rearranged. The downstream core sucks monotonically fluid from this layer until fully developed conditions establish.

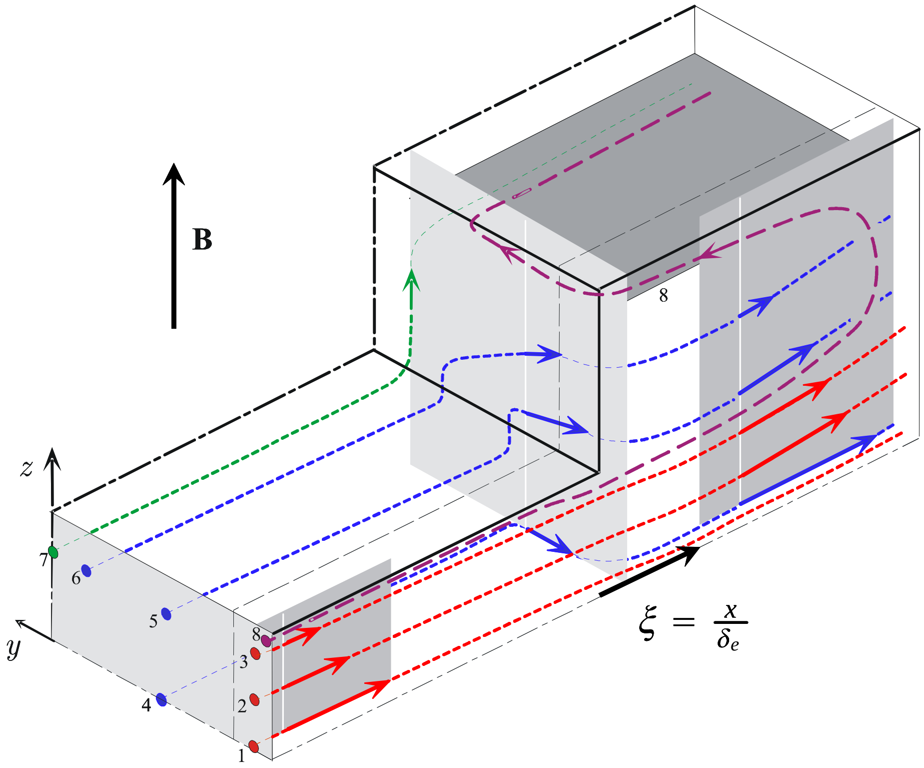

Figure 22: Flow paths in the e-layer. Red lines (1)-(3): flow stays within side layer; blue lines (4)-(6): flow from upstream core enters the e-layer and is transferred into the downstream side layer; green line (7): flow from upstream core crosses the e-layer and enters downstream core; magenta line (8): flow from upstream side layer is involved in recirculation in the downstream side layer. It enters the large duct, turns backward, meets the e-layer in which it is transferred towards the center before it moves downstream.

4 Inertial flows in sudden expansions

Results shown in previous sections have been obtained for flows in very strong magnetic fields, where inertia forces are negligible in comparison with Lorentz forces, i.e. when $N \to \infty$. For weaker fields, when N takes finite values, inertia forces may become comparable with Lorentz forces and they can influence the flow pattern, namely the topology, and the pressure drop. For such cases the asymptotic theory is no longer applicable and results have to be obtained by numerical simulations. The influence of inertia on MHD expansion flows is therefore discussed based on results of numerical simulations.

Results presented here describe major transitions of the flow field when, at a constant Reynolds number, the magnetic field is gradually reduced until the flow reaches the hydrodynamic state, where no magnetic field is present. For more details see e.g. Mistrangelo and Bühler (2007), Mistrangelo (2005). This investigation is of particular interest since the flow paths and the flow topology found for very strong magnetic fields differ substantially from those of hydrodynamic flows. The discussion starts with the case of a strong magnetic field, with $Ha = 1000$, for which the topology of the flow is compared with results from asymptotic considerations. In a sequence of steps the Hartmann number, or equivalently the interaction parameter, is reduced, which results in an increasing complexity of the flow pattern.

In general, the 3D topology of the flow can be illustrated quite efficiently by *skin friction lines* or *limiting streamlines* on the fluid-wall interface. They are defined at the side wall and at the Hartmann wall by

$$\frac{dx}{\tau_x} = \frac{dz}{\tau_z} \text{ at } y = \pm 1 \text{ and } \frac{dx}{\tau_x} = \frac{dy}{\tau_y} \text{ at } z = \pm Z, \tag{68}$$

respectively. Limiting streamlines are defined on the entire walls by (68), except at the singular points, also called the *critical points*, where both components of skin friction vanish (Délery (2001)). The topology of the flow may be characterized by these critical points on the surface like the *nodes* which may act as *sources* ⊙ or as *sinks* or *foci* ⊗ for a 2D flow along the wall, and the *saddle points* ×. The lines shown in red in the following figures mark the *bifurcation lines* (Chong, Perry and Cantwell (1989)) on the walls. The latter are also known as *separation lines* or as *attachment lines* if skin friction lines converge or diverge from them, respectively. The concept of critical points had been introduced by Legendre (1956), and summarized later e.g. by Délery (2001) or by Oertel (2004). Limiting streamlines represent somehow the traces of the 3D flow features in typical planes of the geometry like the walls or the symmetry planes.

4.1 Flow topology and streamlines

As an example let us consider the flow at a constant Reynolds number of $Re = 100$. Numerical results obtained for strong magnetic fields, shown in Fig. 23 for a Hartmann number of $Ha = 1000$, confirm the flow topology derived from the asymptotic analysis. In particular we may identify the same typical flow paths (compare the numbers with those in Fig. 22). There are the paths (4), (6) and (7) starting in the upstream core. When crossing the expansion layer path (4) directly turns towards the side, it meets the side layer in which it remains downstream. Path (6) turns towards the side and upwards along the expansion wall. It comes close to the side but later it redistributes into the downstream core. Path (7) starts also in the upstream core, turns in the expansion layer along magnetic field lines and continues close to the upper

Hartmann wall. Path (8) is the most interesting one. It starts upstream in the side layer close to the Hartmann wall. After the expansion it turns upwards and then it flows even backward towards the expansion wall. Finally it moves along the expansion wall before it makes another turn in downstream direction. One can observe that the expansion layer collects fluid from the upstream core, and distributes it among the downstream core and the side layer. Further downstream excessive side layer flow is redistributed into the core. All these phenomena are conform with the asymptotic predictions.

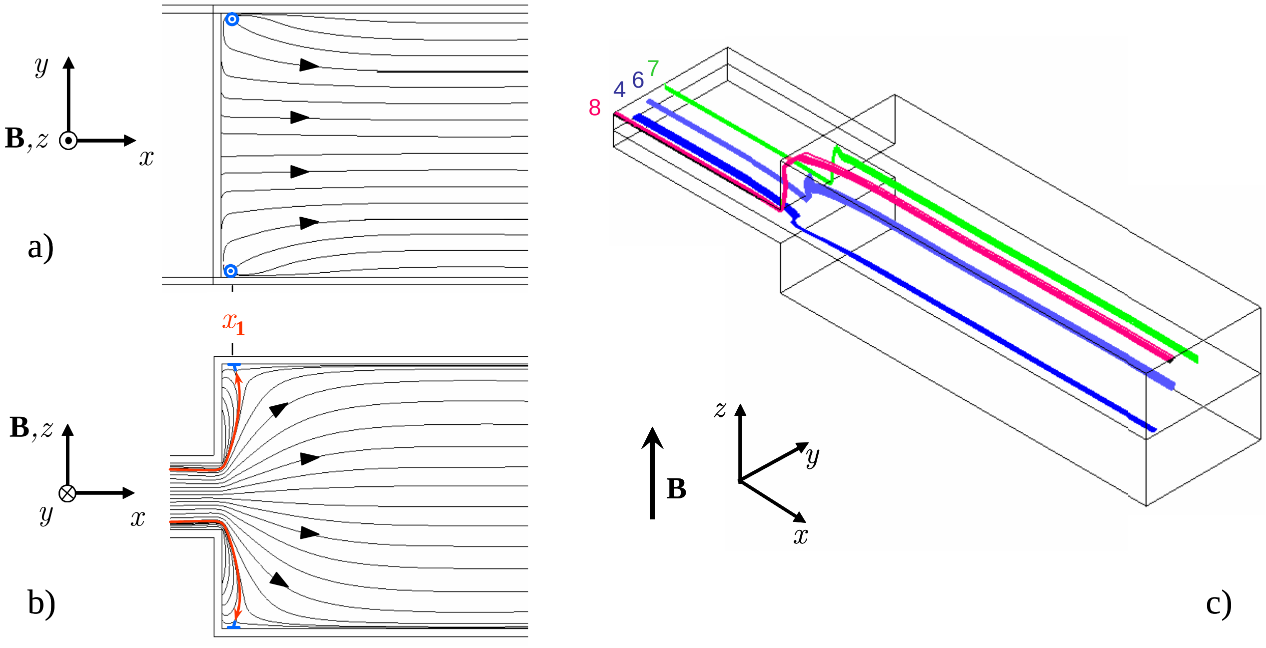

Figure 23: Surface topology shown by limiting streamlines on the Hartmann wall (a) and side wall (b), and 3D streamlines (c) in a sudden expansion for $Ha = 1000$, $N = 10^4$, $Re = 100$, $c = 0.1$. The role of the critical points at the Hartmann walls (a) becomes more obvious from Fig. 24.

For strong magnetic fields the topology of the flow in the large duct at each Hartmann wall is characterized by two nodes or sources located very close to the sides (see Fig. 23a) and by two half saddle points at $x = x_1$ at the common edge between the side and the Hartmann wall. Since source and saddle points are located very close for high Hartmann numbers they cannot be distinguished from the figure, but their role will become obvious later when, for cases with smaller magnetic fields, they can be clearly observed. The corresponding other half saddle points are located at the same positions x_1 but on the side walls, where the bifurcation lines (shown in red) meet the common edge between the side and the Hartmann wall. The nature of the singular points and their role for the 3D flow can be seen from Fig. 24, in which the stagnation streamline (blue) is plotted, ending at the Hartmann wall and creating there the source ⊙ for limiting streamlines along that wall. In the other quarters of the duct, not explicitly shown here, the same structure repeats symmetrically with respect to the horizontal and vertical symmetry planes.

Limiting streamlines plotted at the side wall exhibit regions of reversed flow as already predicted by the asymptotic theory (compare Fig. 16). The fluid that is involved in this backward motion is separated from that moving simply downstream by the red bifurcation streamlines that meet the Hartmann walls in the half saddle points shown in Fig. 23b. The backward flow feeds the expansion layer in which the fluid flows towards the center of the duct. It is found that the recirculations or flow separations, which can be observed at the side wall, occur only in the side layers close to the expansion wall. At some distance from the side wall they are not present anymore and the flow behaves there similarly to that shown in Fig. 24 for the vertical symmetry plane $y = 0$ where no recirculation is present.

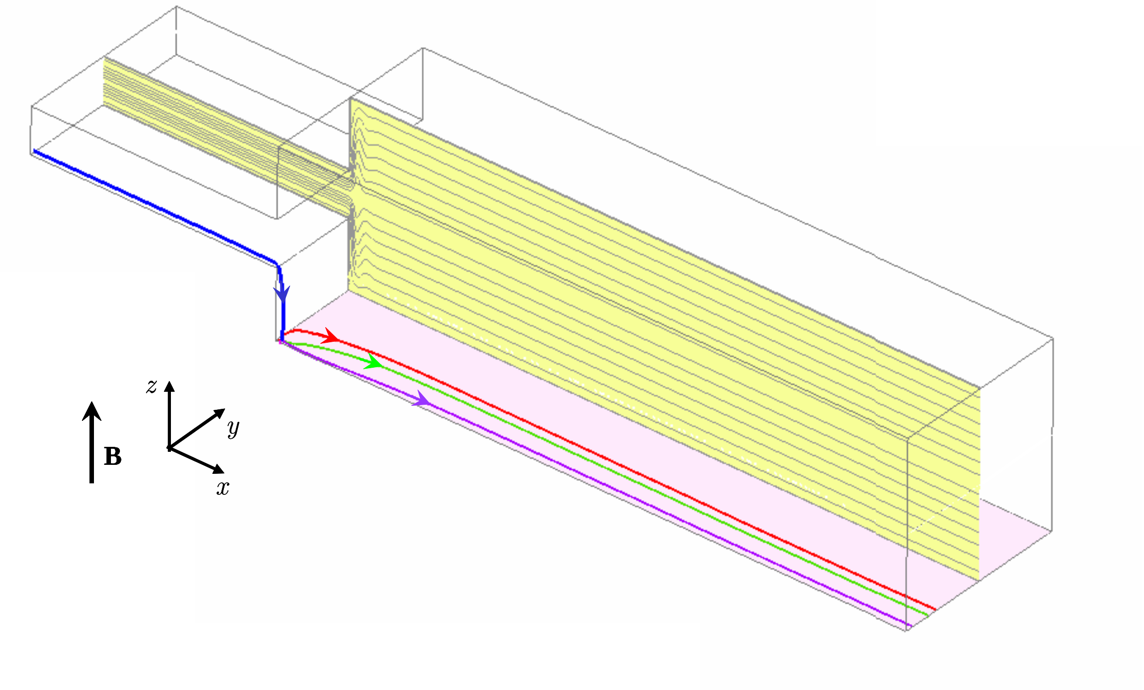

Figure 24: Streamlines in the symmetry plane $y = 0$ and stagnation streamline (blue) towards the singular point at the Hartmann wall for $Ha = 1000$, $Re = 100$, $c = 0.1$. This point is a source for a group of limiting streamlines along the Hartmann wall. Some of them are shown here in different colors.

In the following we investigate the modifications of flow pattern when the magnetic field is reduced. It is found that the situation remains qualitatively as described above. What changes is the position of the half saddle point x_1 that moves downstream when the magnetic field gets weaker. Results for x_1 are shown in Fig. 25 for a given Reynolds number $Re = 100$. For strong fields one can observe a typical dependence of x_1 on the interaction parameter that is close to

$$x_1 \sim N^{-1/3} \quad \text{for} \quad N \gtrsim 12. \tag{69}$$

Scaling laws of this type have been proposed e.g. by Hunt and Leibovich (1967) for an inertial electromagnetic balance in parallel layers and we may interpret this result as an indication that inertia effects are confined either to the internal layer or to the side layers and that inertia forces in the cores are still negligible in comparison with Lorentz forces.

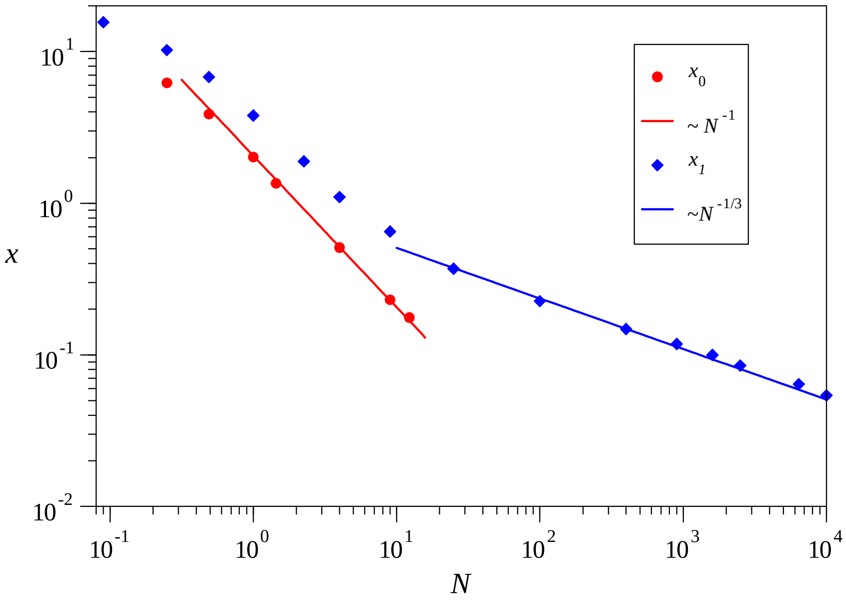

Figure 25: Positions of flow separation x_0 and x_1, measured in the center and at the side of the Hartmann wall, for $Re = 100$, $c = 0.1$.

This behavior remains valid until the interaction parameter falls below a threshold of $N \approx 12$. Below this value the topology on the Hartmann wall changes and there appear two new singular points, a sink close to the expansion wall, and a saddle point, the latter one marks the axial position x_0 of the reattachment line on the symmetry plane as shown in Fig. 26a. The typical variation of x_0 with the interaction parameter is also shown in Fig: 25. It is found that x_0 (and similarly x_1) depends on N as

$$x_0 \sim N^{-1} \quad \text{for} \;\; 0.5 < N < 12. \tag{70}$$

Such a dependence indicates that now inertia forces even in the core become increasingly more important for weaker magnetic fields, when $N < 12$.

Now the expansion layer is thicker and one can observe vortical structures (see Fig. 26c). There exists a spiralling motion around so-called *vortex core lines* that are indicated as the red lines in the sub-plot (c). The vortex core lines start at the side wall in the critical points located here immediately at the inner expansion corners. The fluid is spiralling towards the center of the duct and the singular points at the side walls behave like foci. The vortex core lines extend towards the vertical symmetry plane but since the vortical motion is not present any more at $y = 0$ they end already at some distance from that plane. More details about the topology of the flow at $y = 0$ can be seen from Fig. 27.

The role of the sources at the Hartmann walls remains as before but they move a bit further downstream for lower magnetic fields. This can be seen from Fig. 27a, in which the (blue) stagnation streamline is depicted that ends in the source point at the wall from which limiting streamlines along the Hartmann wall emerge. Some of them like the one shown in green move first backwards, turn then in transverse y direction to approach finally the vertical symmetry plane. Here they turn upwards until they meet and enclose the expanding stream of fluid that passes from the small into the large duct without contributing to the spiralling motion. The

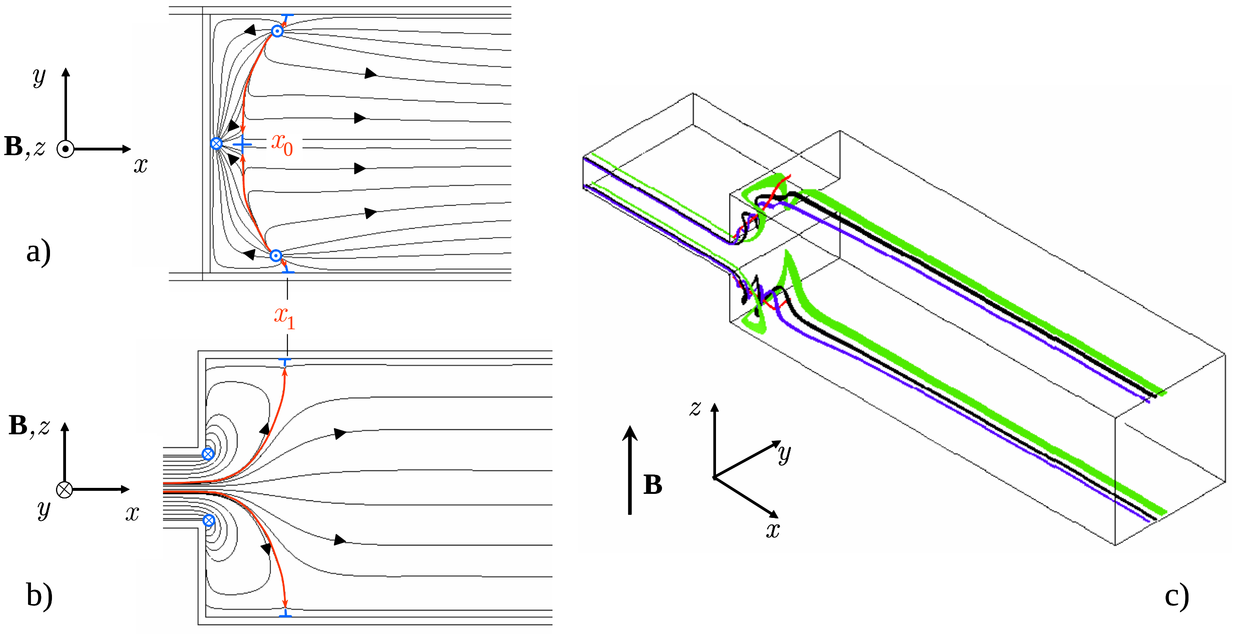

Figure 26: Surface topology shown by limiting streamlines on the Hartmann wall (a) and side wall (b), and 3D streamlines (c) for $Ha = 30$, $N = 9$, $Re = 100$, $c = 0.1$.

vortical structures mentioned above are located in the corner between the expansion wall and the Hartmann wall, enclosed by the stagnation streamline. As shown in Fig. 27b, the vortical motion starts close to the side wall and flow paths involved in that motion spiral around the vortex core lines that have their origin in the attached foci. When spiralling inward the vortical motion is damped out already before the fluid reaches the symmetry plane, at which no vortical streamlines can be observed.

If the magnetic field is further reduced one observes that the focus that was initially attached to the inner corner, now starts to move downstream. While for $Ha = 15$ the focus is still located at the corner, for $Ha = 10$ it is already detached from it. This new topology is shown in Fig. 28 for the example with $Ha = 7$ and $N = 0.49$. It can be seen that the attachment line moves downstream and the distance between positions x_0 and x_1 increases when the magnetic influence becomes weaker. While the two bifurcation lines on the side wall move downstream for weaker fields, they approach each other. When they merge, two new singular points, a source and a saddle point, are created in the horizontal symmetry plane. Now all fluid originating close to the upstream side wall is involved in the vortical motion.

Now at each side wall there exist two detached stable foci, which absorb all the limiting streamlines from their neighborhood. This flow collected by the foci is then transferred towards the center of the duct along the vortex core line until it meets the vertical symmetry plane in an *unstable focus*. From this critical point it spirals outward until it meets the expanding stream of flow from the small duct as shown in Fig. 29b. Streamlines that start at a small distance from the side wall follow similar paths, now spiralling at some distance around the vortex core line.

The role of the critical points at the Hartmann walls remains as before. A stagnation

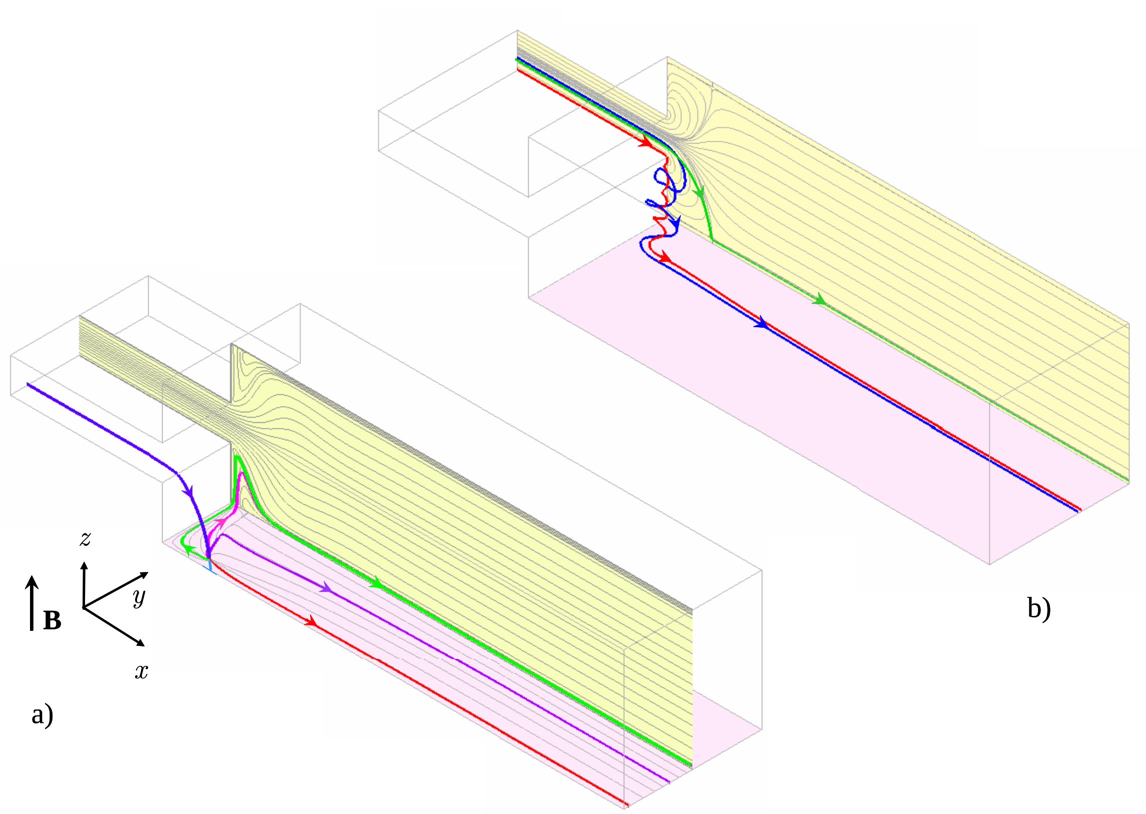

Figure 27: Flow paths and topology for $Ha = 30$, $N = 9$, $Re = 100$. a) Streamlines in the symmetry plane $y = 0$ and stagnation streamline (blue) towards the singular point at the Hartmann wall. The stagnation point acts as a source for limiting streamlines along that wall. Some of them are colored to show typical paths. b) Limiting streamlines on the side wall $y = 1$ and two streamline examples (red and blue) spiralling (closer and at some distance) around the vortex core line, from the attached stable focus at the side into the core. Finally they approach the Hartmann wall.

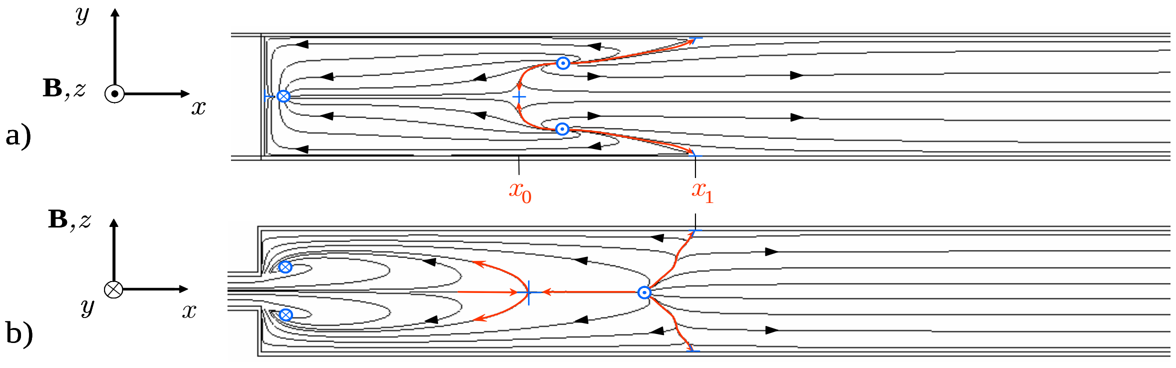

Figure 28: Surface topology shown by limiting streamlines on the Hartmann wall (a) and side wall (b), for $Ha = 7$, $N = 0.49$, $Re = 100$, $c = 0.1$.

streamline (blue) that ends in a source is depicted in Fig. 29a. The fluid along this line simply flows over the vortical structures that are embedded in the corner between the expansion wall and the Hartmann wall. From the source two types of limiting streamlines emerge. One type involves lines associated with a backward motion and the other one the streamlines along which the fluid moves downstream. Both types are separated from each other by the reattachment line which ends at the side walls in two half saddle points at x_1 and which passes through another saddle point x_0 at the vertical symmetry plane. The interesting thing is that all fluid that is involved in the backward motion along the Hartmann wall is found later in the vertical symmetry plane.

With another reduction of the magnetic field, x_0 and x_1 move further downstream. The source and the saddle point at the side wall merge and cancel. The flow remains symmetric with respect to the vertical and horizontal symmetry planes $y = 0$ and $z = 0$, at least down to $Ha = 5$ ($N = 0.25$) as displayed in Fig. 30. The 3D flow topology inside the duct remains very similar to that shown in Fig. 29.

For a Hartmann number of $Ha = 3$ ($N = 0.09$), however, the magnetic influence is so weak that an initially symmetric flow becomes unstable. It looses finally its symmetry with respect to the horizontal symmetry plane $z = 0$ and exhibits a topology very similar to the pure hydrodynamic case that is known to be non-symmetric (Mistrangelo (2005)) for the current value of $Re = 100$. This case is shown in Fig. 31. For these parameters the axial extension of the 3D flow region becomes so large that a complete 3D view on the topology, as shown above for higher magnetic fields, would be not very instructive.

Results shown so far give a good overview about the changes in flow topology when the magnetic field varies in magnitude at the given Reynolds number $Re = 100$. For higher Re the overall picture remains similar but inertial effects within the expansion layer introduce there even a more rich variety of flow pattern. Numerical simulations yield also results for pressure drop, velocity profiles and surface potential distribution as described e.g. by Mistrangelo and Bühler (2007) or Mistrangelo (2005). Such results are skipped here for the moment but some are presented later when they are compared with experimental data.

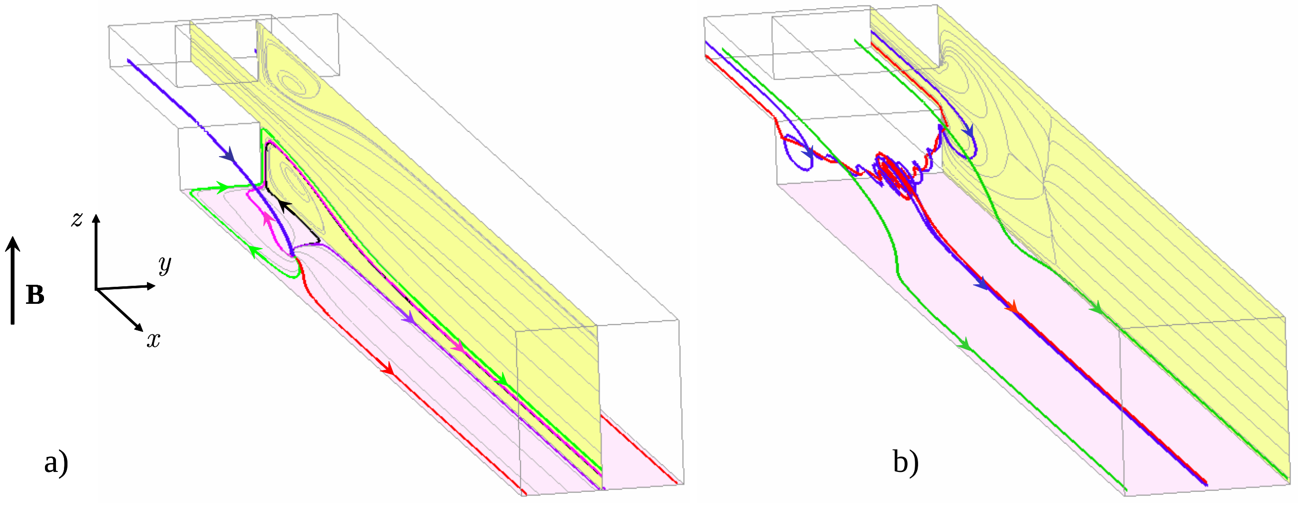

Figure 29: Flow paths and topology for $Ha = 7$, $N = 0.49$, $Re = 100$. a) Streamlines in the symmetry plane and stagnation streamline (blue) towards the singular point at the Hartmann wall. The stagnation point acts as a sources for limiting streamlines along that wall. Some of them are colored to show typical paths. b) Limiting streamlines on the side wall and sketch of two streamline examples (red and blue) spiralling (closer and at some distance) around the vortex core line, from the detached stable foci at the sides towards the unstable focus at the symmetry plane, from which the fluid spirals outward.

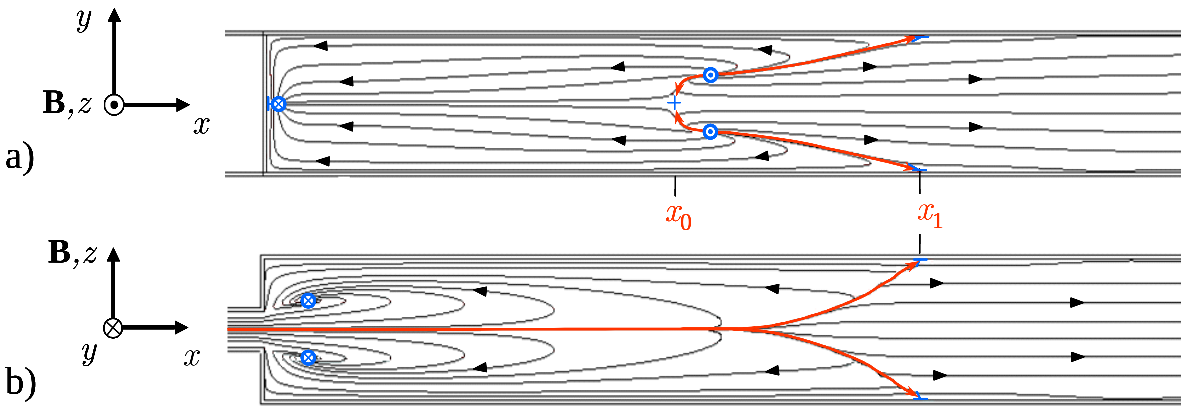

Figure 30: Surface topology shown by limiting streamlines on the Hartmann wall (a) and side wall (b), for $Ha = 5$, $N = 0.25$, $Re = 100$, $c = 0.1$.

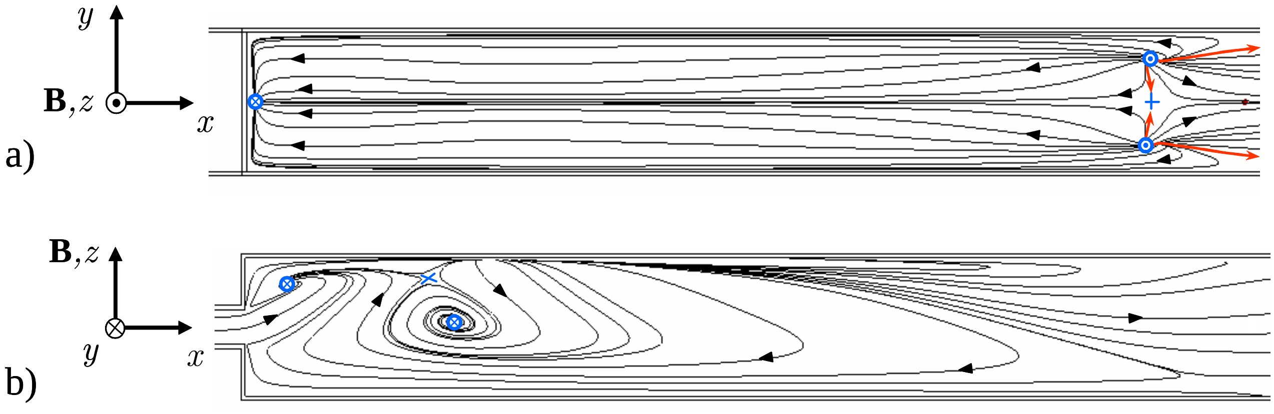

Figure 31: Surface topology shown by limiting streamlines on the Hartmann wall (a) and side wall (b), for $Ha = 3$, $N = 0.09$, $Re = 100$, $c = 0.1$.

5 Experiments

As outlined above, theoretical tools like asymptotic theory or numerical simulations are still not capable of predicting 3D MHD flows for the entire parameter range of interest. The asymptotic approach applies best for very strong magnetic fields where $N \gg 1$, and numerical simulations can cover only the range of small to moderate magnetic fields with $Ha \lesssim 1000$. The current experiment has been designed as a link between both methods with the aim of supporting and validating both these tools by a well defined example of a 3D flow under the influence of an externally applied magnetic field. Of particular engineering interest is here the distribution of pressure along the axis of the ducts, the local electric potential inside the flow as well as the distribution of potential on the surface of the ducts. These quantities have been measured and compared with theoretical predictions. The influence of the Hartmann number Ha and the interaction parameter N on pressure drop and potential is investigated. It is possible to highlight the decreasing influence of inertia forces with increasing magnetic field and to give bounds for the governing parameters beyond which the asymptotic theory is fairly valid.

5.1 The experimental test section

The conceptual design of the experiment and the coordinate system used is shown in Fig. 32. The typical length scale a has been chosen as large as possible but constrained in such a way that the test section with instrumentation fits into the gap of the available magnet. For the present experiment a characteristic length scale of $a = 0.047\,\mathrm{m}$ is used. The duct walls have a thickness of $t_w = 0.003\,\mathrm{m}$ as a compromise between the controversial goals of having thin walls with high electric resistance and walls with sufficient mechanical stiffness. The experiment considers the flow that expands from a small duct of nondimensional cross section $2 \times 2Z_c$ into a square duct of size 2×2. The expansion ratio in the experiment is $1/Z_c = 4$ and it measures the aspect ratio of large and small ducts. The test section has been manufactured from solid pieces of stainless steel by spark erosion in order to avoid welding at the corners. Moreover this procedure yields high precision and sharp internal corners. The entire geometry is composed from several pieces. Some of them are shown in Fig. 33. Three flow straighteners for flow homogenization are installed at distances of $14a$, $15.5a$, $17a$ from the expansion, both at the entrance and the exit of the test section. For measurement of axial pressure distribution a number of pressure taps has been foreseen on the upper Hartmann wall with higher spatial resolution close to the expansion.

The test section has been manufactured from stainless steel *Mat.No.*1.4571 with electric resistivity $\rho_w = 0.791 \cdot 10^{-6}\,\Omega\,\mathrm{m}$ at 20 °C according to Stahl-Eisen-Werkstoffblätter (1992). This results in a specific electric conductivity of $\sigma_w = 1/\rho_w = 1.264\,2 \cdot 10^6\ 1/\,\Omega\,\mathrm{m}$. Considering the fluid conductivity of NaK at the same temperature, $\sigma = 2.88 \cdot 10^6\ 1/\,\Omega\,\mathrm{m}$ (Foust (1972)) we arrive at a wall conductance parameter of

$$c = \frac{\sigma_w t_w}{\sigma a} = 0.028. \tag{71}$$

The test section was installed into the liquid metal NaK loop of the MEKKA laboratory (see Sect.5.2). As a first step, all pressure taps were closed as shown in Fig. 34 and the test section was thermally insulated for the initial wetting procedure, performed at temperatures above 300 °C, for removing impurities and oxide layers from the test section in order to minimize the electric contact resistance between fluid and walls.

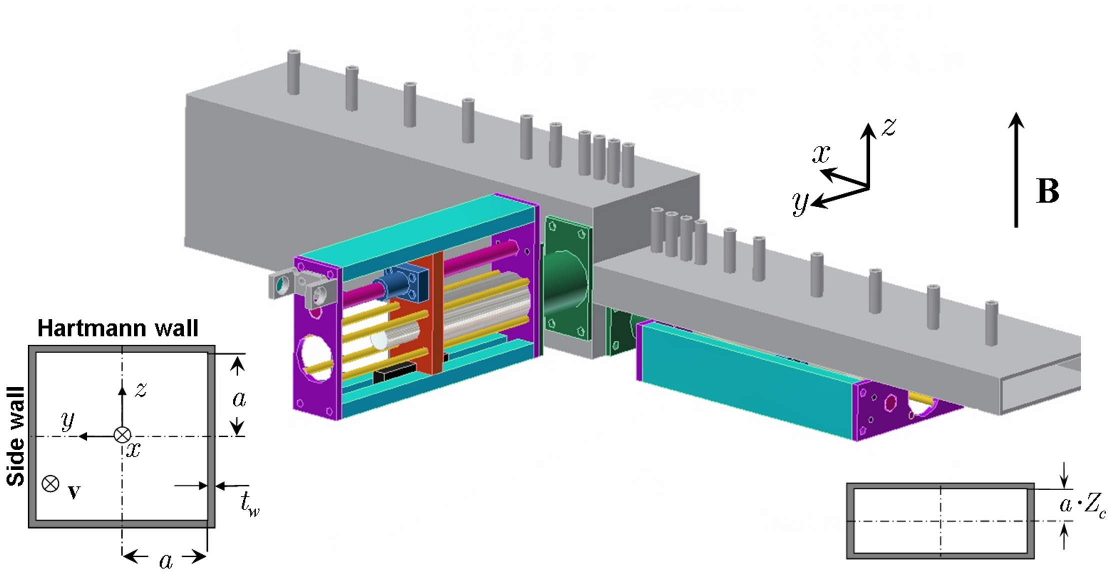

Figure 32: Conceptual design of the expansion test section showing pressure taps at the upper Hartmann walls and mechanical drives for traversable potential gradient probes. The expansion ratio is $1/Z_c = 4$, the characteristic length scale is $a = 0.047\,\mathrm{m}$ and the wall thickness is $t_w = 0.003\,\mathrm{m}$.

After all wetting runs were finished, the thermal insulation was removed and the pressure taps were connected to the measuring piping system as shown in Fig. 35. The loop has been pressurized by argon inert gas and a leak detection spray was used to check tightness. All 16 pressure lines were connected to a unipolar pressure-difference measuring system with 5 entrance pipes for the higher pressure level (H) and 14 entrances for the lower one (L). During pressure measurements a remotely controlled valve system connects always one H pipe and one L pipe with a series of four capacitive pressure transducers of different sensitivity. The reading of the most sensitive transducer, which has not yet reached saturation, is chosen as the pressure value. More details about the pressure measuring system are described in the appendix in Sect. A.2.3.

In a second step the test section was covered by insulating plates, which carry more than 300 spring-loaded probes for detecting the electric potential on the duct walls. Since the walls are thin, the potential measured on the outer surface equals approximately the potential at the fluid-wall interface with errors of the order of $O\left((t_w/a)^2\right)$. Potential measurements give essential information on the flow structure in the ducts, since according to (33), the potential can be interpreted as an approximate streamfunction for the fluid flow and it can be directly compared with theoretical potential data. Figure 36 shows the test section with all surface potential probes installed. After all instrumentation is completed the experiment is moved into the magnet.

After these measurements were completed, traversable probes had been inserted at different axial positions in order to obtain data for local potential, potential gradients, and velocity from

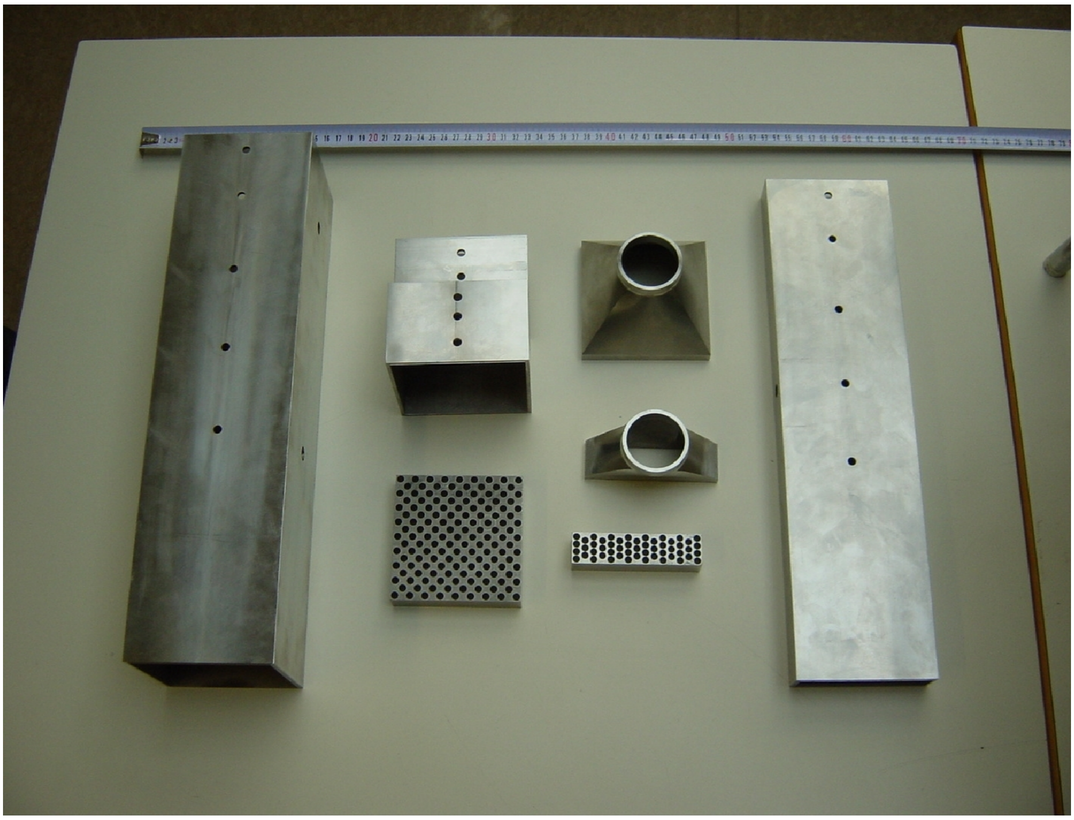

Figure 33: Main parts of the test section before assembling. From left to right: one piece of the large duct, expansion and large flow straightener, fittings for connection with pipes and small flow straightener, one part of the small duct.

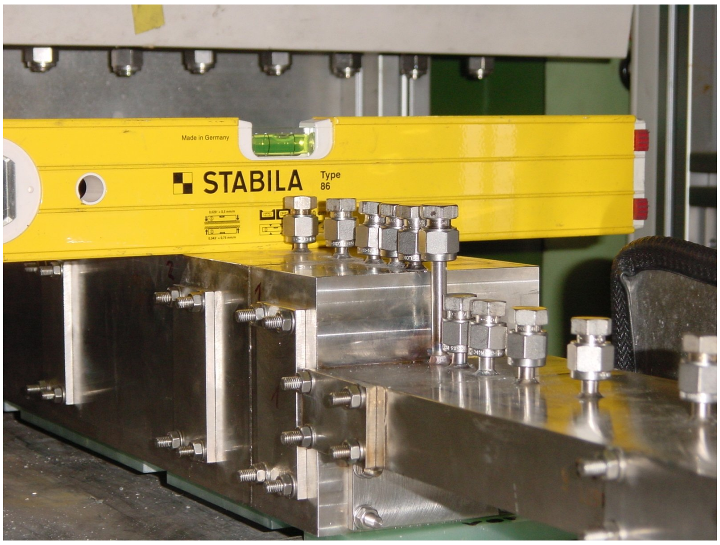

Figure 34: Test section during installation into the liquid-metal loop. All pressure taps are closed.

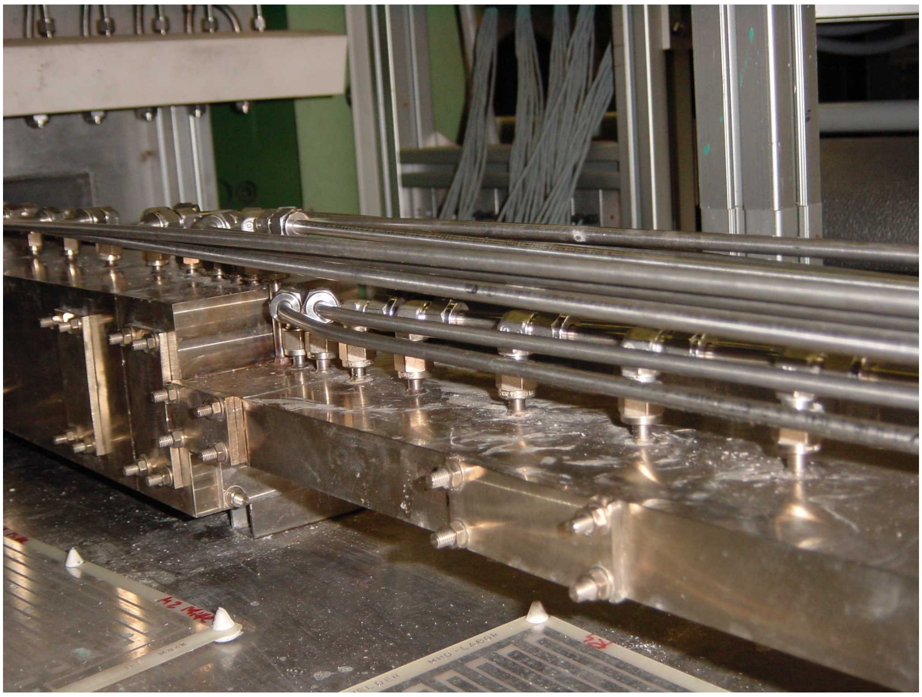

Figure 35: Test section installed in the MEKKA loop. Pressure taps are connected by pipes with the measuring system and covers on the side walls close the openings used for traversable probes.

the interior of the flow. In the present experiment a four-pole probe was used to measure the local potential and its gradient. This probe was moved through the duct by a traversing mechanism whose mechanical part is shown in Fig. 37. The traversing mechanism was driven through a long rotating axis by a stepping motor located outside the magnetic field. The components of potential gradient $\nabla\phi$ in a plane perpendicular to the applied magnetic field, $\nabla_{\perp}\phi$, are directly proportional to the two components of velocity $\mathbf{v}_{\perp}$ in the same plane since according to Ohm's law (3) we have

$$\nabla\phi = \mathbf{v}\times\mathbf{B}\ + ..., \tag{72}$$

where higher order current terms are usually ignored. This assumption is fairly valid for fully developed flows, when $\mathbf{j} = O\left(c\right) \ll 1$, and here we have walls with relatively low conductance $(c = 0.028)$. Then we may approximate the velocity in the plane perpendicular to the field as

$$\mathbf{v}_{\perp} \approx -\frac{\partial\phi}{\partial y}\hat{\mathbf{x}} + \frac{\partial\phi}{\partial x}\hat{\mathbf{y}}.$$

For 3D flows the current density may not be negligibly small and therefore an approximate relationship of $\nabla\phi$ with $\mathbf{v}_{\perp}$ can not be assumed in general. Nevertheless, the measured $\nabla\phi$ can be compared with $\nabla\phi$ obtained by calculations. With a typical distance l between the sensing tips of the probe of $l = 1.5\,\mathrm{mm}$ and an accuracy of the potential difference measuring chain of $\pm 1\,\mu\mathrm{V}$, it is possible to measure velocities or potential gradients with errors of the order $\Delta v_{\perp} = \pm\left(0.3 \div 1.3\,\mathrm{mm/\,s}\right)$ depending on the strength of the applied magnetic field.

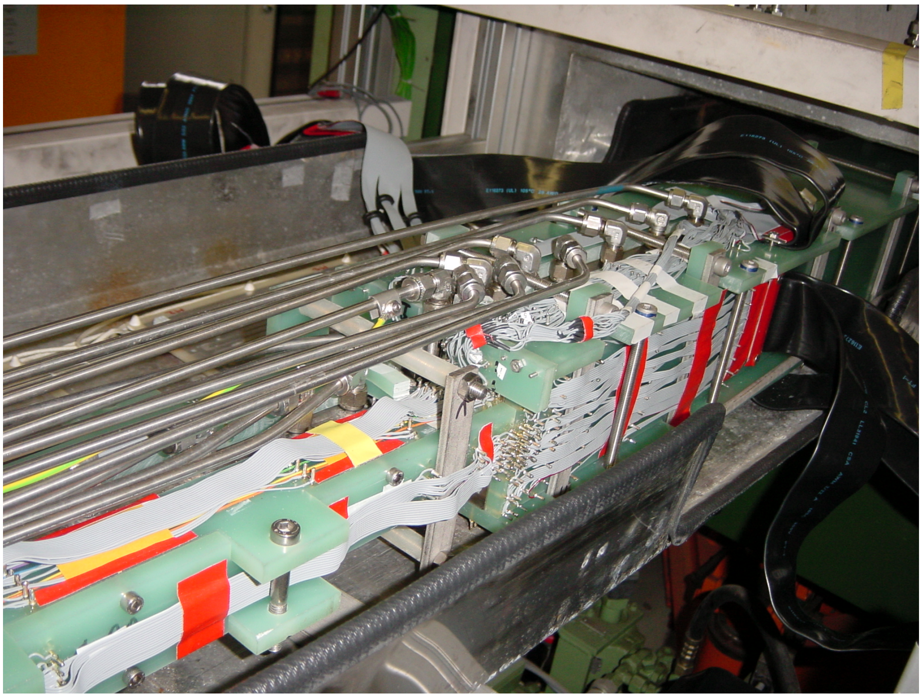

Figure 36: Test section covered with insulating plates that carry more than 300 spring-loaded probes for detection of surface potential. The whole assembly is moved into the magnet after final instrumentation.

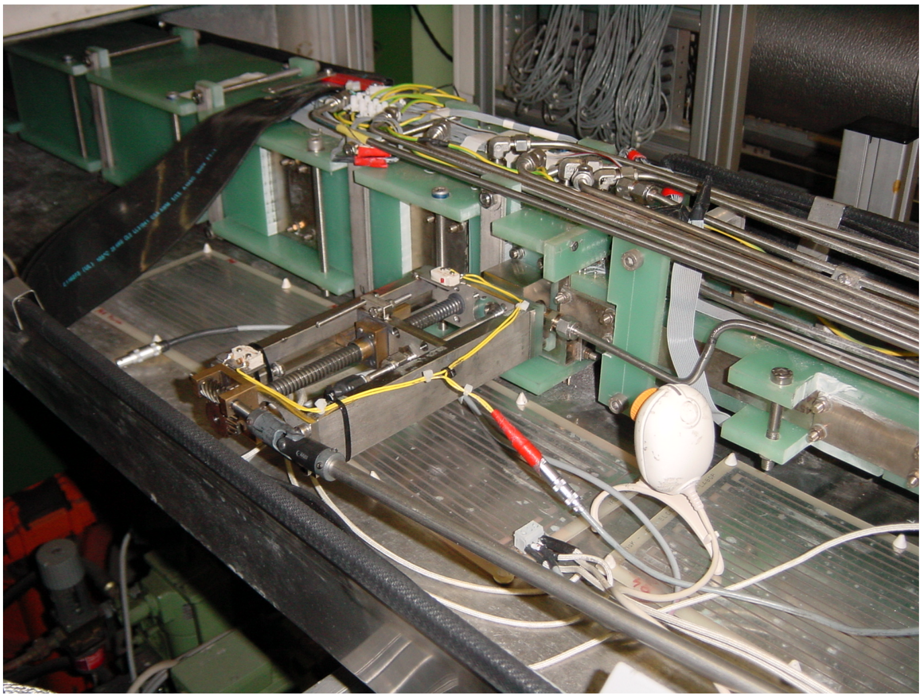

Figure 37: Traversing mechanism for movable potential probes here positioned at the expansion.

5.2 MEKKA laboratory and liquid metal loop

The present MHD expansion experiment is performed in the MEKKA laboratory of the Forschungszentrum Karlsruhe. The measuring techniques used in the MEKKA-facility have been described previously in a detailed report by Barleon, Mack and Stieglitz (1996). Here we summarize and restrict our description to the most relevant parts. A photograph of the MEKKA-facility, in which the expansion test section has been inserted, is shown in Fig. 38.

An eutectic sodium-potassium alloy (Na22K78) is used in the liquid metal loop with fluid properties as (Foust (1972)):

T [°C]	ρ [kg/m^3]	ν [10^{-6} m^2/s]	σ [10^6 1/Ω m]
20	868.4	1.05	2.88
40	863.2	0.902	2.79
60	858.1	0.834	2.70

NaK has a lower density and a higher electrical conductivity compared to a lead-lithium alloy $Pb - 17Li$ foreseen in the blanket design. This allows in the present experiments to reach, with the available magnet of about 2T, high Hartmann numbers up to $Ha = 5800$, which are not too far from fusion applications.

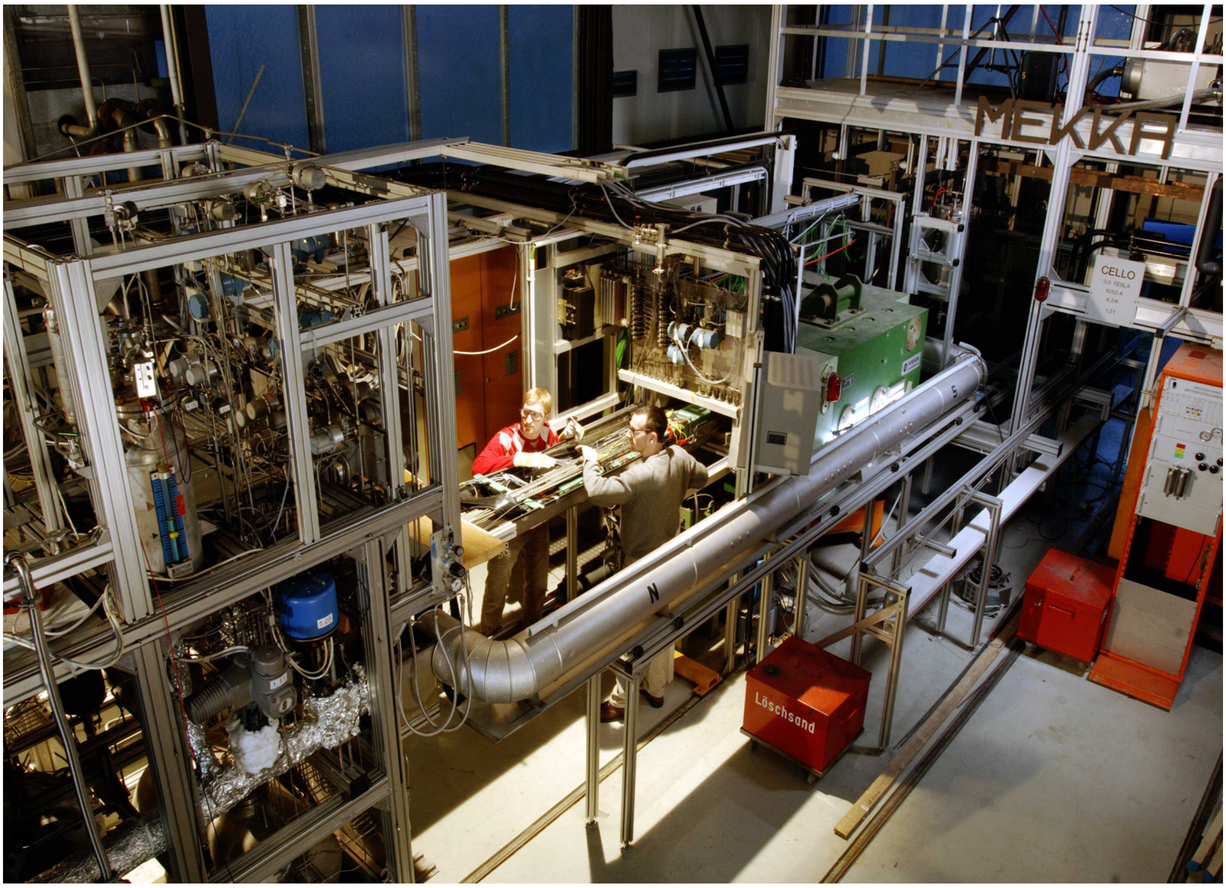

Figure 38: View on the liquid-metal NaK loop of the MEKKA laboratory.

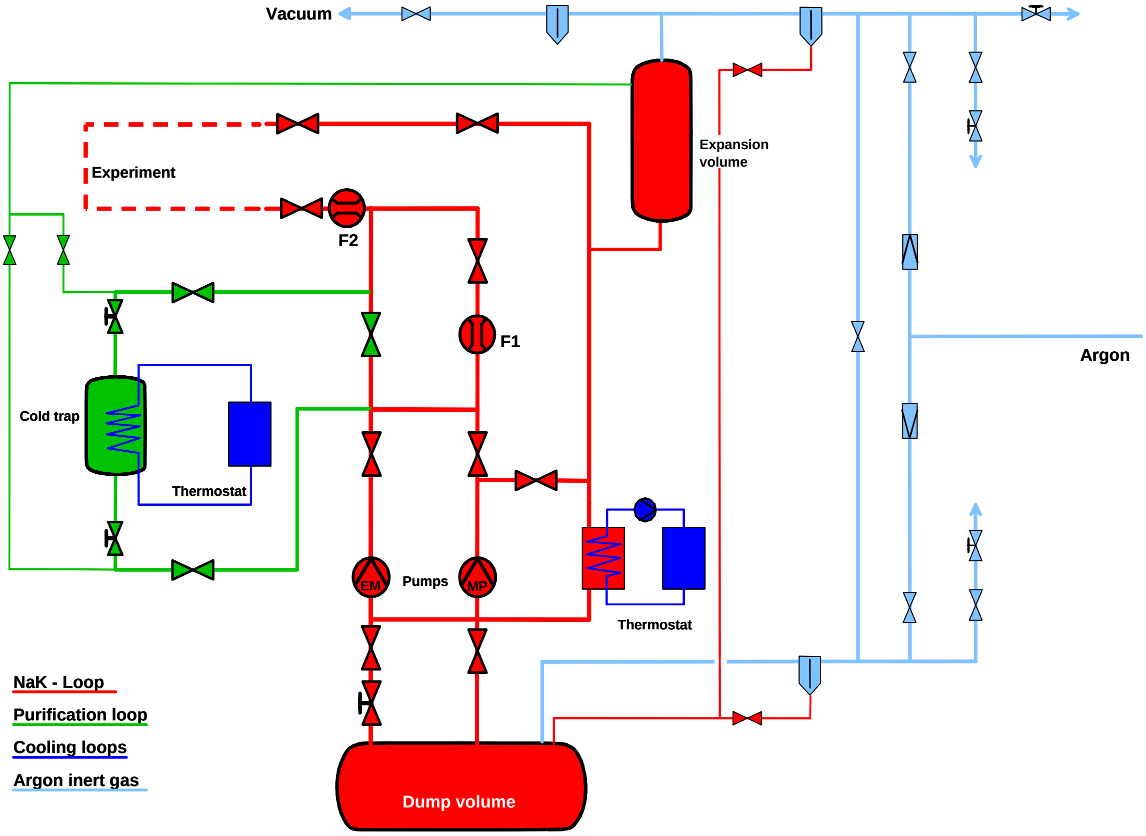

Figure 39: Schematic of the liquid metal NaK loop in the MEKKA laboratory. The different colors indicate different parts of the total system. Red: liquid metal loop; green: purification loop; blue: oil cooling loops (water cooling loops are not shown); light blue: inert gas system.

Figure 39 shows a sketch of the liquid metal loop. A canned motor pump with a maximum pressure head of 0.9 MPa and a flow rate of $25\,\mathrm{m}^3/\,\mathrm{h}$ circulates the liquid metal at temperatures below 150 °C. A second electromagnetic pump is used for low flow rates and for high temperature runs. Due to the technical features of the loop and the magnet, the MEKKA facility is capable of attaining interaction parameters in the range of $N = 10^2 \div 10^5$, which are appropriate for applications in liquid-metal fusion blankets.

The whole liquid metal loop with pumps, dump volume, expansion tank, heat exchanger, cold trap, pressure transducers, controlling valves etc. is mounted in a rack, which is movable on rails. The arrangement of a movable loop with connected test section enables the operator to place the test section at any desired position relative to the fixed magnet. This allows a good manual access to the instrumented locations of the test section and variable positioning of the experiment within the magnet. Thus, special measurement positions of the test section within the magnetic field can be realized.

The loop with all its systems is totally remote controlled from the operation room. All critical components are connected via alarm sensors to the input gates of a programmable logic controller that takes appropriate reaction.

The uniform transverse magnetic field is provided for this experiment by a normal conducting dipole magnet. Its maximum field strength is 2.1 T. The magnetic field has a vertical orientation and is directed perpendicular to the axis of the channel. The magnetic gap used for the experiment has a cubic shape and within a region of 800 mm × 480 mm × 165 mm the field is quite uniform with deviations from the core value smaller than 1%. More technical details concerning the magnet, measurements of flow rate, pressure differences, and electric potential are shifted to the appendix.

5.3 Results

5.3.1 Pressure

The pressure has been measured along the upper Hartmann wall at 16 pressure taps for various mean velocities, varying in the large duct in the range $1\,\mathrm{mm/\,s} \lesssim u_0 \lesssim 0.7\,\mathrm{m/\,s}$ and for magnetic fields within $0.18\,\mathrm{T} \lesssim B_0 \lesssim 2\,\mathrm{T}$. As already outlined, all dimensions are scaled with the half width a of the duct and the pressure values shown in the following are scaled with the pressure scale $p_0 = \sigma a u_0 B_0^2$. The results shown in Figs. 40-43 were taken in the range between some few mbar and several bar, depending on mean velocity and magnetic field. They condense into a unique nondimensional representation, confirming the validity of the used pressure scaling.

The measured data far upstream ($x \ll 0$) and downstream ($x \gg 0$) from the expansion approach perfectly the predicted pressure gradients for fully developed MHD flows in accordance with (29) and with the asymptotic theory for $N \to \infty$ as indicated by the dashed lines in the diagrams. This shows that the entrance and exit lengths of the experiment are sufficiently long to reach (with the used flow homogenizers at $x \approx \pm 14$) fully established conditions.

The upstream pressure gradient of the fully established flow is considerably higher than that of the downstream flow. This has its origin partly in the fact that the velocity is higher in the small duct. Another reason is that the relative conductance of the wall in comparison with the conductance of the fluid (ratio of wall thickness to local Hartmann length) is higher in the small duct than in the large one. This results in higher currents in the fluid with associated larger pressure drop at upstream positions.

Near the expansion the pressure drops more rapidly due to three-dimensional recirculating electric currents, associated with additional Joule dissipation. A small fraction of this extra pressure drop is recovered behind the expansion in the downstream duct but a major part, called Δp_{3D} remains irreversibly lost.

As a first example let us consider results for a moderate magnetic field, i.e. for $Ha = 500$ and $N = 50$ as shown in Fig. 40. In the figure experimental observations are compared with results of a numerical simulation. The agreement is quite good so that we may conclude that the numerical code is able to predict the essential phenomena and in particular the pressure drop in a correct way at least up to this Hartmann number.

Experimental results for higher Hartmann numbers in the range $1000 \leq Ha \leq 5000$ are shown in Figs. 41-43 and compared with predictions by the asymptotic theory. Each figure displays results for flows at a fixed magnetic field, i.e. for a constant Hartmann number Ha, while the velocity or equivalently the interaction parameter N or the Reynolds number Re have been widely varied by more than two orders of magnitude. All results show that with increasing interaction parameter N, the measured distribution of pressure converges monotonically towards the red solid line that has been obtained by asymptotic-numeric analysis as outlined in Sect. 3. These measurements confirm quite well the accuracy of the computational approach which is valid in the inertialess limit as $N \to \infty$.

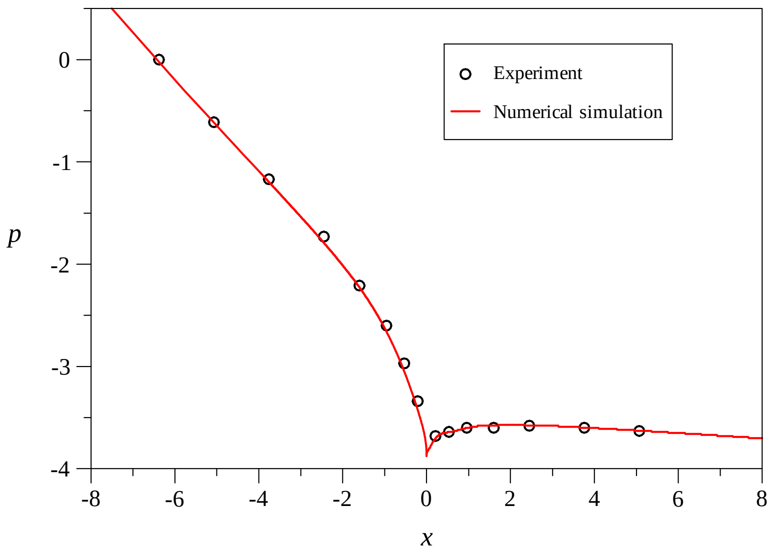

Figure 40: Pressure along the upper Hartmann wall for $Ha = 500$ and $N = 50$. Comparison of measured values and numerical simulation.

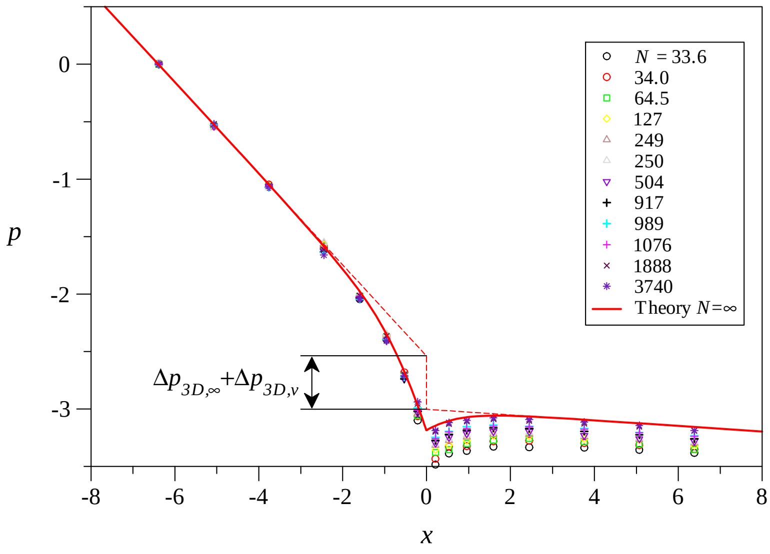

Figure 41: Pressure along the upper Hartmann wall for $Ha = 1000$ and various interaction parameters N.

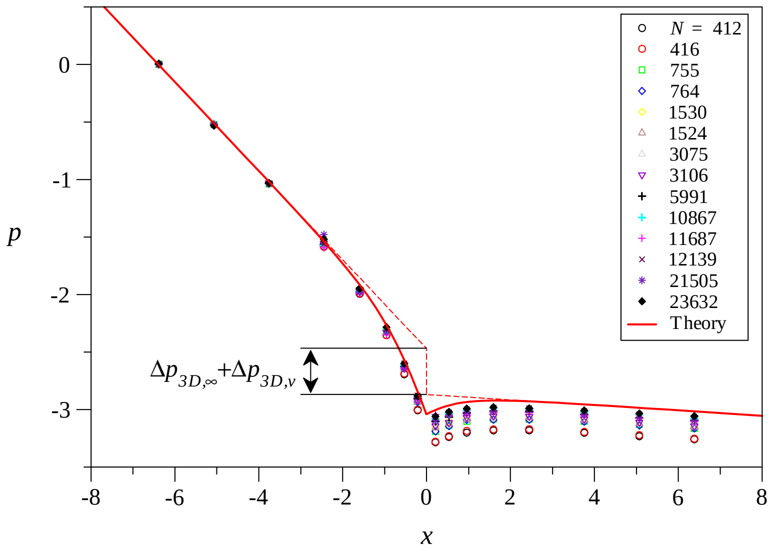

Figure 42: Pressure along the upper Hartmann wall for $Ha = 3000$ and various interaction parameters N.

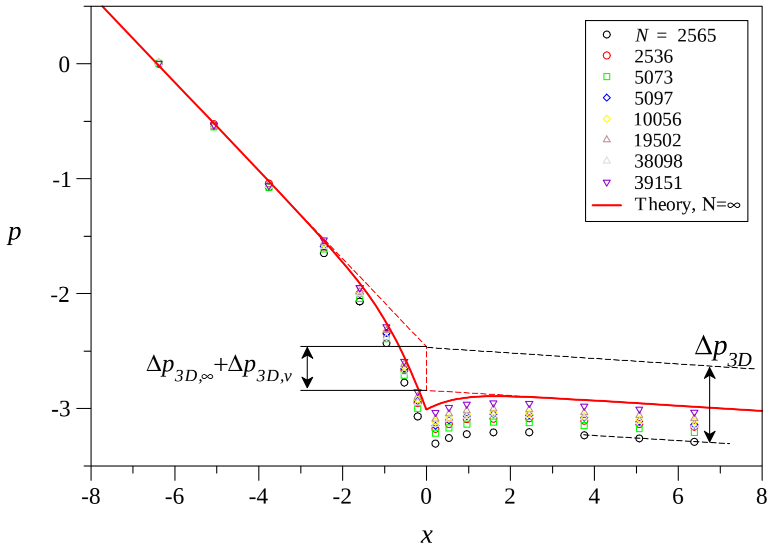

Figure 43: Pressure along the upper Hartmann wall for $Ha = 5000$ and various interaction parameters N.

As indicated in Fig. 43 the total pressure drop is composed by several different contributions. The two most obvious parts arise from the fully established flows in the small and large ducts, which are well known from literature (Chang and Lundgren (1961), Walker (1981), Bühler (2003)). The fully developed pressure gradients are indicated in the figures by the red dashed lines that extrapolate the entrance and exit conditions towards the position $x = 0$. As mentioned above, near the expansion there appears an additional pressure drop caused by 3D effects due to velocity redistribution and extra current flow. This part Δp_{3D} depends in general on all parameters that govern the flow, namely on the Hartmann number Ha and on the interaction parameter N (or the Reynolds number Re).

Results for Δp_{3D} can be analyzed in more detail. For further investigations we decompose it as

$$\Delta p_{3D} = \Delta p_{3D,\infty} + \Delta p_{3D,v} + \Delta p_{3D,i}. \tag{73}$$

Here $\Delta p_{3D,\infty}$ and $\Delta p_{3D,v}$ are the inertialess inviscid and viscous contributions, respectively, as indicated in Figs. 41-43, and $\Delta p_{3D,i}$ is the inertial part.

The first two terms have their origin in 3D current loops that close their paths through the cores, the conducting walls and the viscous layers and they can be perfectly described by the inertialess asymptotic theory. The viscous part $\Delta p_{3D,v}$ depends on the interaction of viscous and electromagnetic forces, i.e. it depends, for a given geometry, exclusively on the Hartmann number Ha. From the results shown in Fig. 44 we conclude that the 3D viscous pressure drop scales for high Hartmann numbers as

$$\Delta p_{3D,v} = 4.76\ Ha^{-1/2}. \tag{74}$$

This result has been obtained theoretically. A comparison with the experimental data shown in Fig. 44 confirms these calculations. With increasing Hartmann number the viscous layers become progressively thinner so that their contribution to the current path vanishes as $Ha \to \infty$. A detailed study of this effect is displayed in Fig. 44, which shows clearly the linear dependence of $\Delta p_{3D,v}$ on $Ha^{-1/2}$. In the asymptotic limit, as $Ha \to \infty$, the 3D pressure drop approaches the value $\Delta p_{3D,\infty}$ where viscous contributions are not present any more. This part of pressure drop depends only on the geometry and conductivity of the ducts and scales most sensitively with the expansion ratio Z_C/Z_c and with the wall conductance parameter c as discussed above or shown by Bühler (2007). For the present experiment with $Z_C/Z_c = 4$ and $c = 0.028$ a value

$$\Delta p_{3D,\infty} = 0.315 \tag{75}$$

has been found.

A dependence of flow properties on $Ha^{-1/2}$ is typical for flows in which viscous parallel layers are important. The results indicate that the parallel layers in the present experiment play a key role in the understanding of the physics at the expansion and for the prediction or simulation of abruptly expanding MHD flows. Such parallel layers are present along the side walls of the ducts and their thickness in the inertialess limit is known to scale as $\delta_s \sim Ha^{-1/2}$. In addition, at the expansion, an internal parallel layer develops along the expansion wall and spreads through the fluid along magnetic field lines. For finite values of Ha, 3D current loops find additional paths through these layers, which increases the total current density near the expansion and creates increased pressure drop proportional to these currents. The possibility for an intense exchange of flow between cores, expansion layer and side layers has been addressed already in Sect. 3.4.1,

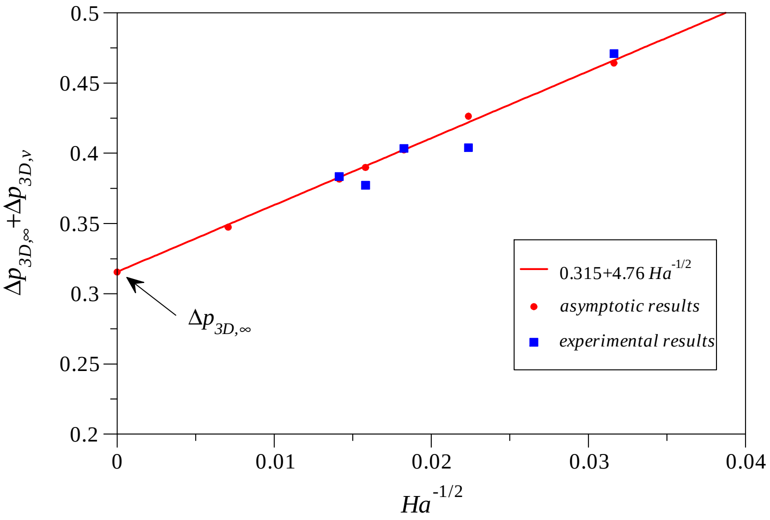

Figure 44: Inertialess parts of the three-dimensional pressure drop as a function of $Ha^{-1/2}$. $\Delta p_{3D,\infty}$ stands for the 3D pressure drop of MHD flows in the expansion with $Ha \to \infty$ and $N \to \infty$ and $\Delta p_{3D,v}$ is the viscous contribution. Experimental points have been obtained from data as shown e.g. through Figs. 41-43, extrapolated towards $N \to \infty$ as displayed in Fig. 45.

by Bühler (2003) or by Mistrangelo (2005). The experimental investigation of this point will be outlined later in a separate subsection.

As mentioned above, in addition to the discussed pressure drop contributions, it is possible to identify another part that has its origin in inertial effects, which become increasingly important for flows at higher velocities, i.e. at higher Reynolds numbers. The magnitude of the inertial part $\Delta p_{3D,i}$ depends in general on the Hartmann number Ha, the Reynolds number Re or the interaction parameter N. The inertial fraction $\Delta p_{3D,i}$ is plotted in Fig. 45 for several Hartmann numbers. The figure supports the idea that the inertial part of pressure drop scales linearly with $N^{-1/3}$ as $\Delta p_{3D,i} = m\,N^{-1/3}$. For higher Hartmann numbers one can observe a stronger dependence on N, i.e. a bigger slope of the lines that fit the data points. The slope can be correlated with the Hartmann number as $m = 0.62 \cdot 10^{-3} Ha$ as shown in Fig. 46. From these data it is now possible to construct a correlation as

$$\Delta p_{3D} = 0.315 + 4.76\; Ha^{-1/2} + 0.62 \cdot 10^{-3} Ha\, N^{-1/3}, \tag{76}$$

or in terms of the Reynolds number as

$$\Delta p_{3D} = 0.315 + 4.76\; Ha^{-1/2} + 0.62 \cdot 10^{-3} \left(Ha\, Re\right)^{1/3}. \tag{77}$$

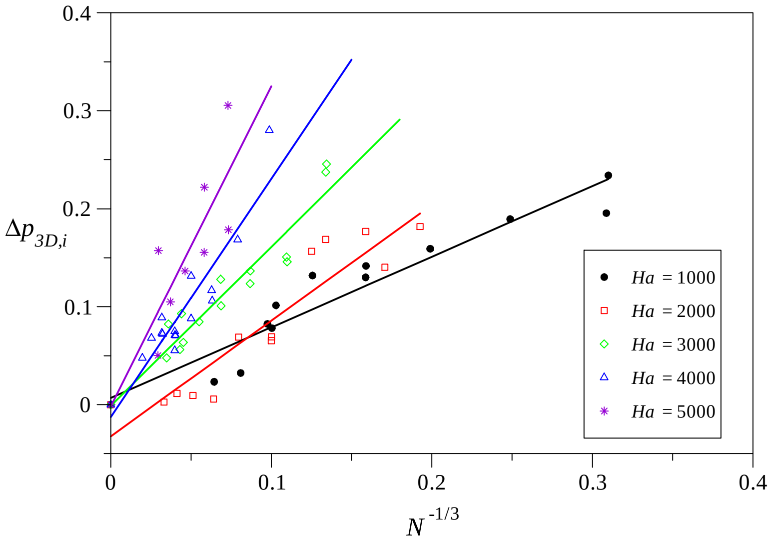

Figure 45: Inertial part $\Delta p_{3D,i}$ of three-dimensional pressure drop displayed as a function of $N^{-1/3}$. The values $\Delta p_{3D,i}$ represent deviations from inertialess calculations at a downstream position where fully developed flow is established. See Figs. 41-43.

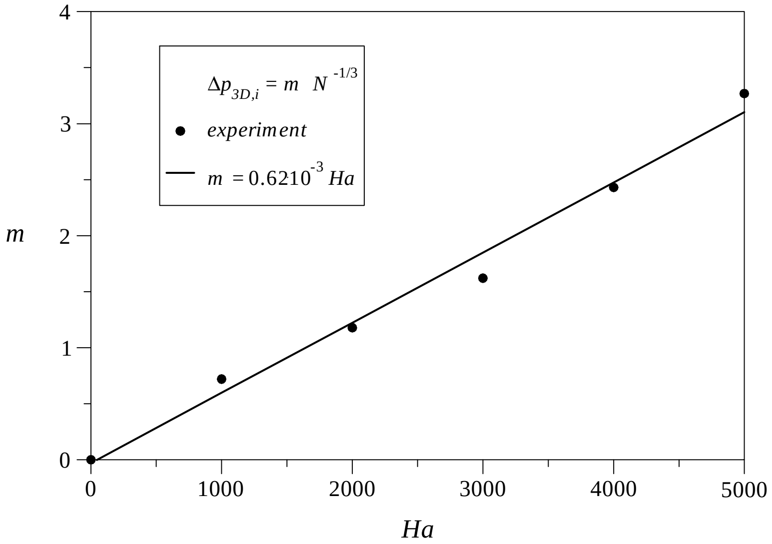

Figure 46: Dependence of 3D pressure drop coefficient m on the Hartmann number Ha.

5.3.2 Velocity

Data for local velocity may be extracted from measurements of local potential or to be more precise by the measurement of local potential gradients. For that reason traversable potential probes have been moved through the duct at different axial positions. A sketch of the traversable probe is shown in Fig. 47. The potential gradient may be directly interpreted as a velocity signal since, according to Ohm's law (3), velocity may be derived from

$$-\nabla\phi + \mathbf{v} \times \hat{\mathbf{z}} = \mathbf{j} = 0 + O\left(c\right),$$

which leads to an approximation of axial and transverse velocity components as

$$u \approx -\frac{\partial\phi}{\partial y}, \quad v \approx \frac{\partial\phi}{\partial x}. \tag{78}$$

The potential gradient approximates the velocity usually quite well if current density is small. This is the case e.g. for fully developed flows in ducts with thin walls when $c \ll 1$ or in insulating straight ducts. Near the expansion, where additional 3D currents are present, the velocity according to (78) might require a correction, but still the transverse gradient of potential, which has been recorded correctly, may serve as validation data for numerical tools.

The probe has been used to measure the absolute value of potential ϕ, i.e. the potential difference between the point **a** and the ground **g** (reference potential, $\phi_{\mathrm{g}} \equiv 0$) that is located on the upper Hartmann wall at the symmetry plane

$$\phi\left(y_{\mathrm{a}}\right) = \phi_{\mathrm{a}} - \phi_{\mathrm{g}}. \tag{79}$$

The horizontal components $\nabla_{\perp}\phi$ of the potential gradient (transverse and axial, in the plane perpendicular to $\mathbf{B}$) are obtained by recording the following three potential differences:

$$\Delta\phi_{\mathrm{ab}} = \phi_{\mathrm{a}} - \phi_{\mathrm{b}}, \quad \Delta\phi_{\mathrm{bc}} = \phi_{\mathrm{b}} - \phi_{\mathrm{c}}, \quad \Delta\phi_{\mathrm{ca}} = \phi_{\mathrm{c}} - \phi_{\mathrm{a}}. \tag{80}$$

For details of the geometry see Fig. 47. The transversal and axial potential gradients are then calculated using the known positions of the sensing tips of the probes located at

$$\mathbf{a} = \left(x_{\mathrm{a}}, y_{\mathrm{a}}, 0\right), \quad \mathbf{b} = \left(x_{\mathrm{b}}, y_{\mathrm{b}}, 0\right), \quad \mathbf{c} = \left(x_{\mathrm{c}}, y_{\mathrm{c}}, z_{\mathrm{c}}\right). \tag{81}$$

The probe was initially designed in such a way that $x_{\mathrm{a}} = x_{\mathrm{b}}$. However, because of difficulties during fabrication both axial positions differ slightly and this small difference is taken into account during evaluation of the data. The electrode at position **c** is located slightly out of the symmetry plane, shifted by the small quantity $z_{\mathrm{c}} \ll 1$. Nevertheless its recorded value can be directly used as the potential value at $z = 0$ since $\phi_{\mathrm{c}} \approx \phi\left(x_{\mathrm{c}}, y_{\mathrm{c}}, 0\right) + \partial\phi/\partial y\left(x_{\mathrm{c}}, y_{\mathrm{c}}, 0\right) z_{\mathrm{c}}$, where the last term vanishes due to symmetry. Although two potential differences were sufficient to determine the horizontal components of potential gradient, all the three were measured. This allows checking the quality of the measurements since

$$\Delta\phi_{\mathrm{ab}} + \Delta\phi_{\mathrm{bc}} + \Delta\phi_{\mathrm{ca}} = \varepsilon, \tag{82}$$

where ε should be theoretically zero. For practical measurements ε was about $0.2 \div 1.5\%$ of the measured data for $\Delta\phi_{\mathrm{ab}}$. The horizontal potential gradient $\nabla_{\perp}\phi = \partial_x\phi\,\hat{\mathbf{x}} + \partial_y\phi\,\hat{\mathbf{y}}$ is then obtained from the system of equations

$$\Delta\phi_{\mathrm{ab}} = \nabla_{\perp}\phi\cdot(\mathbf{a}-\mathbf{b}) = \frac{\partial\phi}{\partial x}(x_{\mathrm{a}}-x_{\mathrm{b}}) + \frac{\partial\phi}{\partial y}(y_{\mathrm{a}}-y_{\mathrm{b}})\,, \tag{83}$$

$$\Delta\phi_{\mathrm{ca}} = \nabla_{\perp}\phi\cdot(\mathbf{c}-\mathbf{a}) = \frac{\partial\phi}{\partial x}(x_{\mathrm{c}}-x_{\mathrm{a}}) + \frac{\partial\phi}{\partial y}(y_{\mathrm{c}}-y_{\mathrm{a}})\,, \tag{84}$$

where all horizontal coordinates of the sensing tips are taken into account.

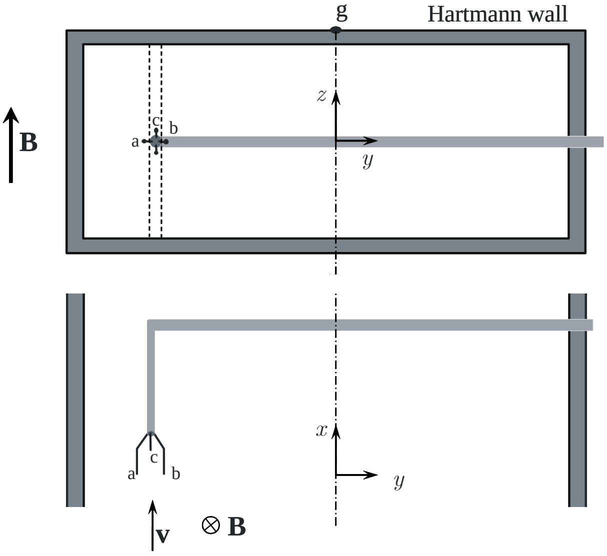

Figure 47: Sketch of traversable potential probe.

Profiles of upstream potential Let us start the discussion of local flow properties for a cross section located upstream of the expansion at $x = -5.6$ in the region of fully developed flow. The Figs. 48 - 50 display nondimensional values of potential according to relation (79), recorded for different Hartmann numbers ranging from $Ha = 1000$ up to $Ha = 5000$. For each Hartmann number the flow rate (Reynolds number Re or interaction parameter N) was varied over a wide range. The lower bound of Re was restricted by the accuracy of the measuring system (lower limit of u_0, upper limit for N). The upper one was given by the power of the pump and the mechanical strength of the test section (upper limit of u_0, lower limit for N). We observed here, as expected for unidirectional MHD flows, a linear variation of potential in the center of the duct, i.e. in the core. This is another indication that fully developed conditions are well established at $x = -5.6$ before the flow approaches the expansion. Deviations from the linear law are present only near the side wall at $y = -1$. Unfortunately there exist no data points in the vicinity of the other side wall near $y = 1$ because it was not possible, for geometrical restrictions of the traversing mechanism, to move the probe closer to this wall.

Profiles of upstream axial velocity After the potential is known, it is straightforward to evaluate the local transverse potential gradient, which approximates the axial velocity in fully developed flows as $u \approx -\partial\phi/\partial y$, by differentiation of potential with respect to y. On the other

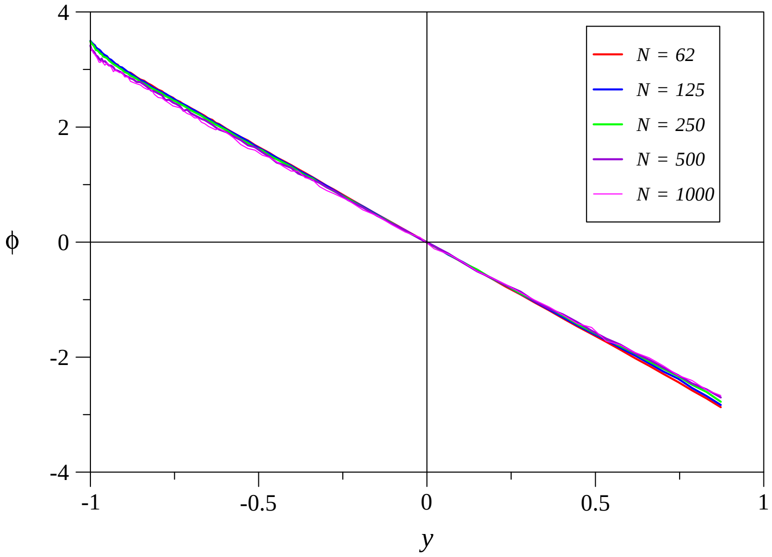

Figure 48: Potential $\phi(y)$ at $x = -5.6$, $z = 0$ for $Ha = 1000$ and different N.

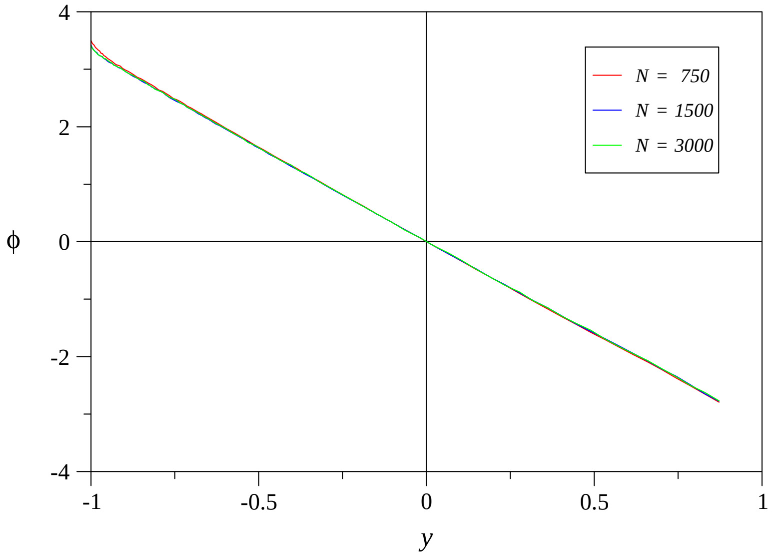

Figure 49: Potential $\phi(y)$ at $x = -5.6$, $z = 0$ for $Ha = 3000$ and different N.

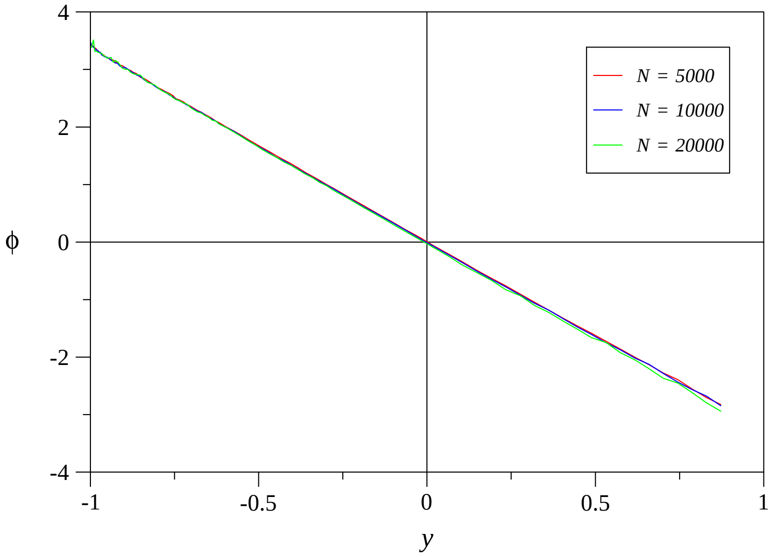

Figure 50: Potential $\phi\,(y)$ at $x = -5.6$, $z = 0$ for $Ha = 5000$ and different N.

hand it is possible to compare these values with those derived from direct measurements of local potential gradient according to (83) and (84). For higher and moderate velocities both sets of data are in good agreement and confirm thus the quality of the current experiments. For smaller velocities, however, the local potential gradients measured directly by the probe underestimate the real potential gradient as calculated from the absolute values of potential. Therefore those results have been rescaled in order to fit the potential gradient data obtained by differentiation of ϕ. The moderate disagreement is most probably caused by the fact that the probe itself disturbs the local flow field. Especially for high Hartmann numbers, the probe generates a wake type depression of the velocity profile by the formation of internal parallel layers that spread along magnetic field lines from the probe towards the Hartmann walls. Results for various Hartmann numbers and interaction parameters are shown in Figs. 51-53.

This type of internal parallel layer forms not only in the vicinity of the tip of the probe but also along its whole shaft through part of the duct cross section from the side wall $y = 1$ to the tip at $y = y_\mathrm{a}$. For that reason the flow is weakly reduced in $y_\mathrm{a} \lesssim y < 1$ and as a result increased in $-1 < y \lesssim y_\mathrm{a}$. This fact explains the slight slope of core velocity. For stronger magnetic field, i.e. for higher Ha, this systematic disturbance of the flow increases.

As a result of all measurements at the upstream position $x = -5.6$ we observe a flat uniform value of velocity or potential gradient in the core with a strong increase towards the side walls where the high-velocity jets are present. Since these jets are very thin and the size of the probe is finite, it is not possible for the largest Hartmann numbers under consideration to resolve the region of viscous decay towards the side wall. Nevertheless it is possible to investigate the behavior of the flow in the side layer at some distance from the wall. In general one can summarize the results as follows: for the highest investigated interaction parameters the side layers are found to be very thin. This is in accordance with the theoretical predictions which suggest that the side layers are as thin as $Ha^{-1/2}$. With increasing Reynolds number (decreasing

N) the mean thickness of the side layers becomes suddenly larger. This effect is caused by the occurrence of instabilities of the jet flow along the side walls. The laminar flow becomes unstable, shows time-dependent variations with increased exchange of momentum with the core. As a result, the side layers become thicker on a temporal average. A complete description of this observation is out of the scope of the present work and will be described separately.

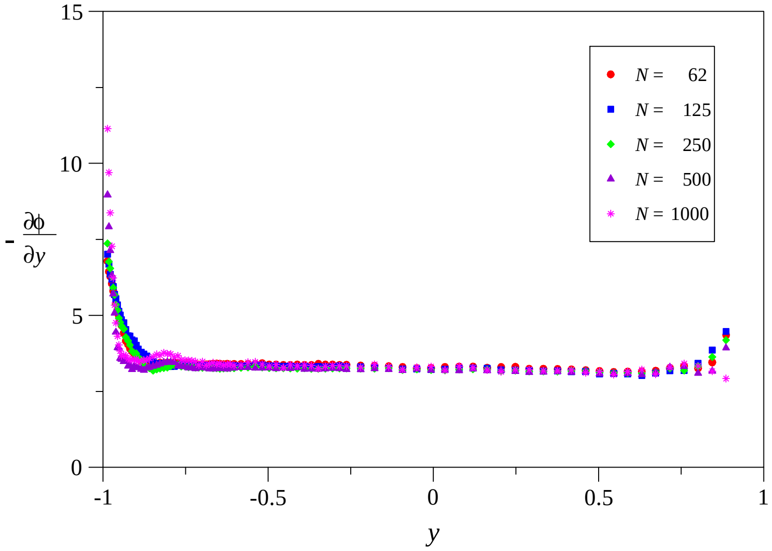

Figure 51: Velocity $u(y) \approx -\partial\phi/\partial y$ at $x = -5.6$, $z = 0$ for $Ha = 1000$ and different N.

Profiles of axial velocity at the expansion When approaching the expansion, the initially flat core velocity profile becomes deformed. Figures 55-57 display this behavior at $x = 0$, i.e. in the expansion layer.

The transverse potential gradients as shown through Figs. 55-57 are usually a good indication of axial velocities in the horizontal symmetry plane $z = 0$. However, one has to keep in mind that 3D currents at this position are not necessarily small so that $-\partial\phi/\partial y$ may differ even by a significant amount from the axial velocity u at $x = 0$. Nevertheless, measured transverse potential gradients can be used for a comparison with theoretical predictions for inertial flows as shown e.g. in Fig. 54. The agreement between measured values (red symbols) and results of numerical simulations (red solid line) is quite good. This confirms the validity of the numerical model and its capability for correctly predicting the strong gradients in the side layers. The calculated axial velocity (black line) has been added to the figure for comparison, to show the similarity with the profile of transverse potential gradient but also to show where deviations from potential gradients may occur. Close to the sides velocity and potential gradients are almost equal but in the core they may deviate by a factor of two.

Compared with the upstream flow distribution shown in the previous subsection the velocity at $x = 0$ is reduced in the center and increased closer to the sides. What appears here as relatively thick side layers is just a result of the deformation of axial velocity profiles in the expansion layer. This deformation is caused by Lorentz forces due to 3D currents and by the fact that the upstream and downstream cores have to be matched across the expansion layer.

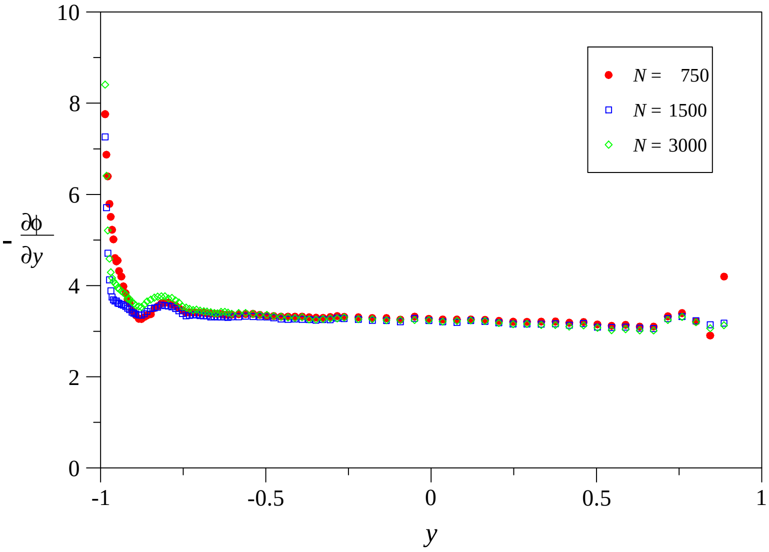

Figure 52: Velocity $u(y) \approx \partial\phi/\partial y$ at $x = -5.6$, $z = 0$ for $Ha = 3000$ and different N.

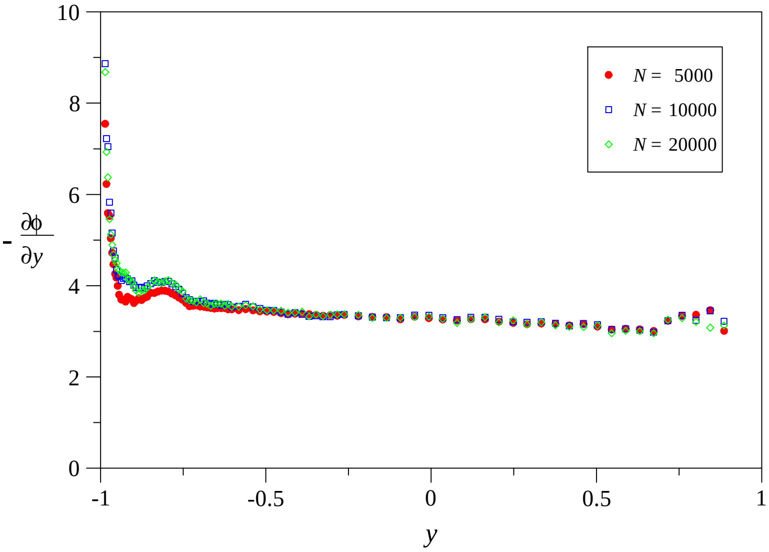

Figure 53: Velocity $u(y) \approx -\partial\phi/\partial y$ at $x = -5.6$, $z = 0$ for $Ha = 5000$ and different N.

Let us consider for the moment the flow at a constant magnetic field e.g. for $Ha = 1000$ as shown in Fig. 55. We observe a deformed profile in the core with a depression in the center and increased potential gradient near the sides. With increasing magnetic field the volume flux near the sides increases and the maximum gradient of potential in the layers increases. For the investigated interaction parameters one can notice a clear dependence of the side layer values on N, while the dependence of the core values is not so evident. At this Hartmann number the measured transverse potential gradient (indication of axial velocity) in the side layer, measured at the smallest possible distance to the wall, exceeds the mean velocity u_0 in the large duct by a factor of 16. All these observations are in accordance with the common understanding of 3D MHD flows, where the 3D extra currents brake the flow in front of the expansion and favor an intense exchange of flow with the side layers.

For stronger magnetic fields, with increasing Hartmann numbers, the side layers become thinner and the influence of inertia effects is not so strong anymore, at least in the investigated range of interaction parameters shown in Fig. 56 for $Ha = 2000$.

By further increasing the Hartmann number to a value of $Ha = 4000$ the side layers become even thinner. Associated with that fact, the values in the layer close to the wall should increase further. Unfortunately the maximum of the jet velocity is located so close to the side walls that the peak can not be resolved with the present probe of finite dimension. What can be observed from Fig. 57 is that the side layers depend not so strongly on inertia as for $Ha = 1000$. In the center of the duct, however, some inertial influence remains for $1000 \leq N \leq 4000$. In this range of N the velocity in the center reduces with increasing N. For $N \geq 16000$ inertia seems not to play a significant role any more, since curves through the symbols for $N = 16000$ and $N = 32000$ practically coincide in this range.

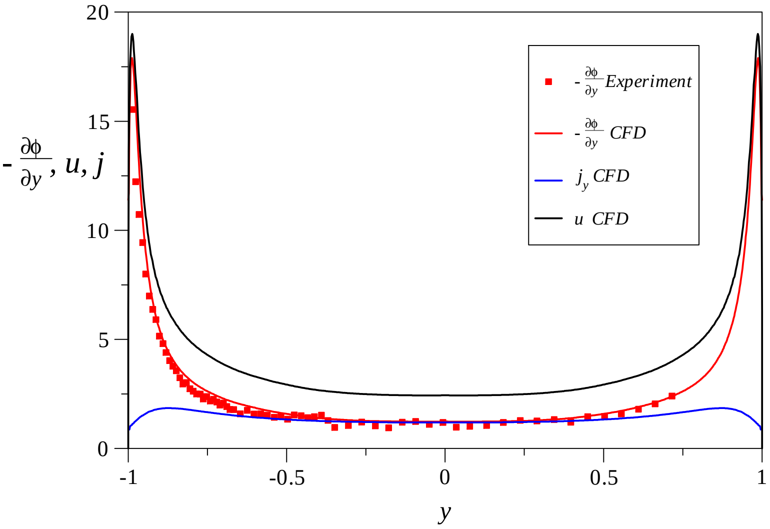

Figure 54: Comparison between experimentally and numerically obtained transverse potential gradient for $Ha = 1000$, $N = 2000$. The calculated velocity $u = -\partial\phi/\partial y - j_y$ close to the side walls is almost equal to the potential gradient but in the core the velocity is about twice as high as $-\partial\phi/\partial y$ due to strong induced 3D transverse current density j_y.

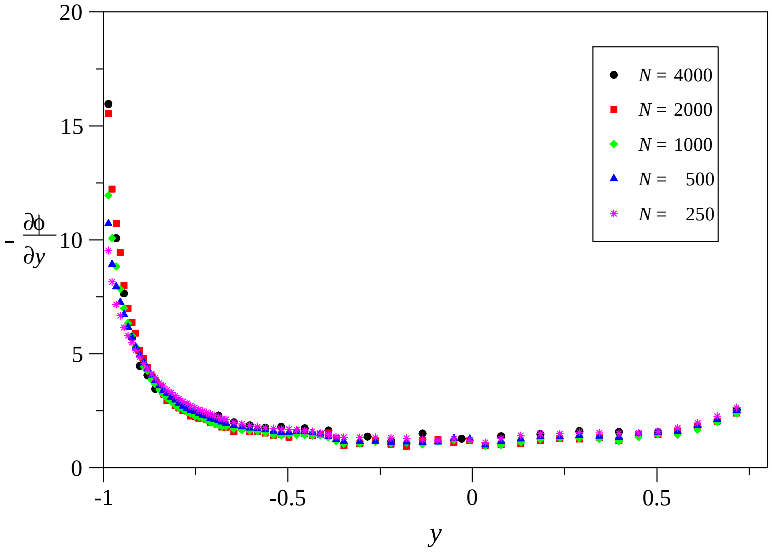

Figure 55: Profiles of transverse potential gradient $-\partial\phi/\partial y$ (indication of axial velocity) at $x = 0$, $z = 0$ for $Ha = 1000$ and different N.

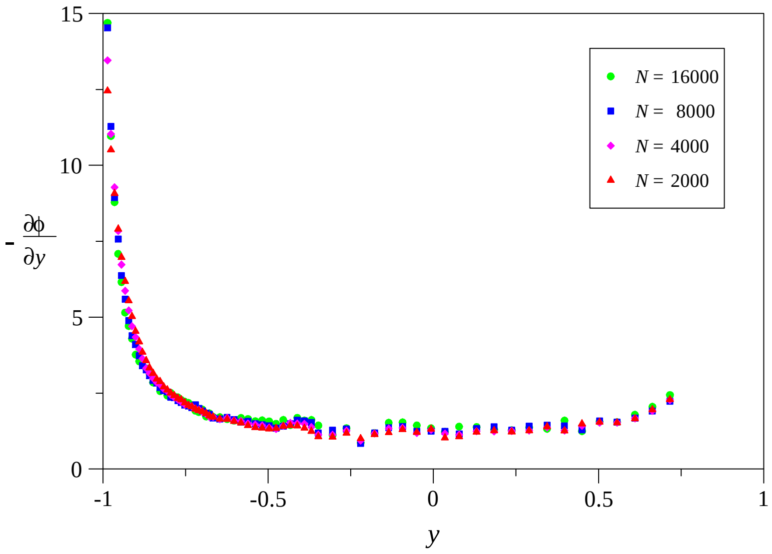

Figure 56: Profiles of transverse potential gradient $-\partial\phi/\partial y$ (indication of axial velocity) at $x = 0$, $z = 0$ for $Ha = 2000$ and different N.

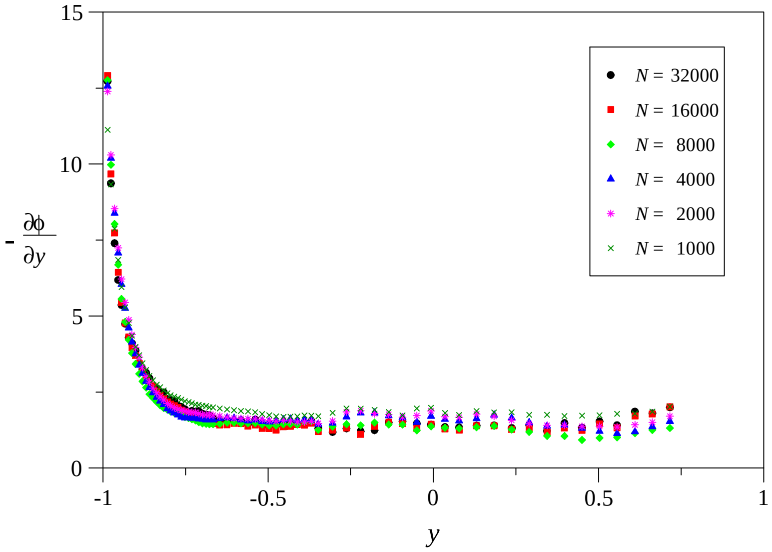

Figure 57: Profiles of transverse potential gradient $-\partial\phi/\partial y$ (indication of axial velocity) at $x = 0$, $z = 0$ for $Ha = 4000$ and different N.

Profiles of transverse velocity at the expansion So far we analyzed the behavior of the axial velocity component u at $x = 0$ in the expansion layer. With the potential probe as shown in Fig. 47, however, it is possible to investigate in addition the flow component v transverse to the main flow direction. Information about the transverse velocity v may be derived from the axial component of potential gradient $\partial\phi/\partial x$. Due to the geometry of the probe the axial position at which the transverse velocity is measured is slightly shifted downstream with respect to the expansion. It corresponds approximately to the nondimensional position $x \approx 0.01$. As predicted by the asymptotic theory and as confirmed by numerical analysis (Mistrangelo (2005)) the expansion layer carries an order one flow rate. Since the layer may be very thin for strong magnetic fields, the transverse velocity can reach considerable magnitude.

In Figs. 58-60 the axial component of potential gradient $\partial\phi/\partial x$ (indication of transverse velocity v) is shown for various Hartmann numbers and interaction parameters. As expected according to theoretical predictions, high transverse velocities are found already for $Ha = 1000$. We observe here that $v < 0$ for $y < 0$ and $v > 0$ for $y > 0$ which is reasonable since the expansion layer collects a large fraction of the incoming core flow of the small duct and transfers it in a symmetric manner towards the right and left side layers. This leads to an approximately linear behavior of v near the center. Closer to the sides the input from the upstream core rises, which leads to a much stronger increase in transverse velocity than in the center of the duct. The highest values of v are observed close to the side walls.

With increasing the interaction parameter the magnitude of the velocity component v becomes larger. The maximum transverse velocity v depends clearly on the interaction parameter and $\partial\phi/\partial x$ reaches, for the considered range of N, values up to $v \approx \pm 4$ which is already four times larger than the mean velocity u_0. For the highest N (the smallest Re), for which it was possible to obtain reliable data, the flow in the expansion layer is still inertial since $\partial\phi/\partial x$ depends essentially on N. Moreover, it is not even possible to estimate or predict the existence of an asymptotic limit for the maximum value of $\partial\phi/\partial x$ as $N \to \infty$.

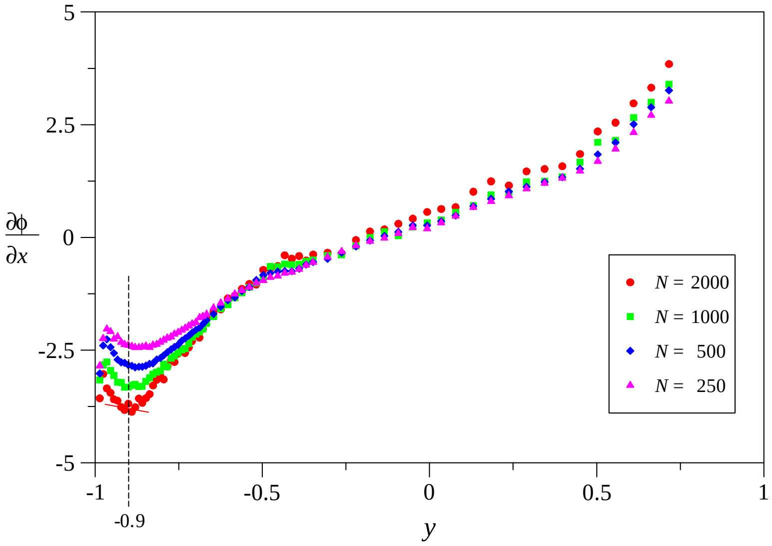

Figure 58: Profiles of axial potential gradient $\partial\phi/\partial x$ (indication of transverse velocity v) at $x \approx 0.01$, $z = 0$ for $Ha = 1000$ and different N.

For higher Hartmann numbers e.g. $Ha = 2000$ or 4000 the maximum axial potential gradient (transverse velocity) in the expansion layer increases further and exceeds even values which are more than 13 times larger than the mean velocity u_0 (see Figs. 59, 60).

In order to quantify our observations, let us consider the absolute value of axial potential gradient (transverse velocity v) at a position $y = -0.9$ near the side wall and collect all results for different Ha and N in a single diagram as shown in Fig. 61. One can observe that the magnitude of the axial potential gradient (transverse velocity) increases monotonically with increasing N and it seems the Hartmann number does not play an important role here in the range of investigated parameters. It appears as if the data vary as $N^{0.25}$ for $N < 5000$ (dashed line) while a variation proportional to $N^{0.37}$ (solid line) seems to approximate better the experimental data for $N > 5000$. The most important result here is that even for the highest interaction parameter of $N = 64000$ the flow in the expansion layer remains inertial. Indeed, inertia effects are expected to become negligible, according to order of magnitude arguments discussed e.g. by Hunt and Leibovich (1967) or Bühler (2003), only if $N \gg Ha^{3/2}$, which is not the case for any of our measurements. For that reason the balance of forces in the layer is dominated here by electromagnetic and inertial forces with the consequence that the layer thickness, its electric conductance, and the ability to carry mass flux is purely determined by N, independent of the Hartmann number Ha.

Profiles of downstream axial velocity In the following we consider the axial velocity profiles at the position $x = 1.91$ downstream of the expansion. This position is located not too far from the expansion so that inertia effects, caused by the strong 3D redistribution of the flow at the expansion, are still visible at least for the cases where the Reynolds numbers are high or the interaction parameters are moderate. The influence of inertia can be observed e.g. for $Ha = 1000$ in Fig. 62. In this figure we notice relatively small core velocities u_{core}, which vary between $0.25 < u_{\text{core}} < 0.5$ and as a result, depending on the interaction parameter, most of the

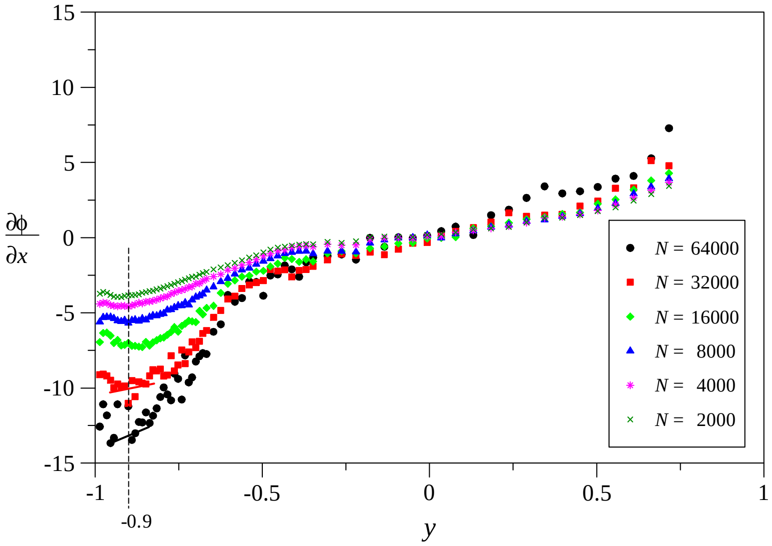

Figure 59: Profiles of axial potential gradient $\partial\phi/\partial x$ (indication of transverse velocity v) at $x \approx 0.01$, $z = 0$ for $Ha = 2000$ and different N.

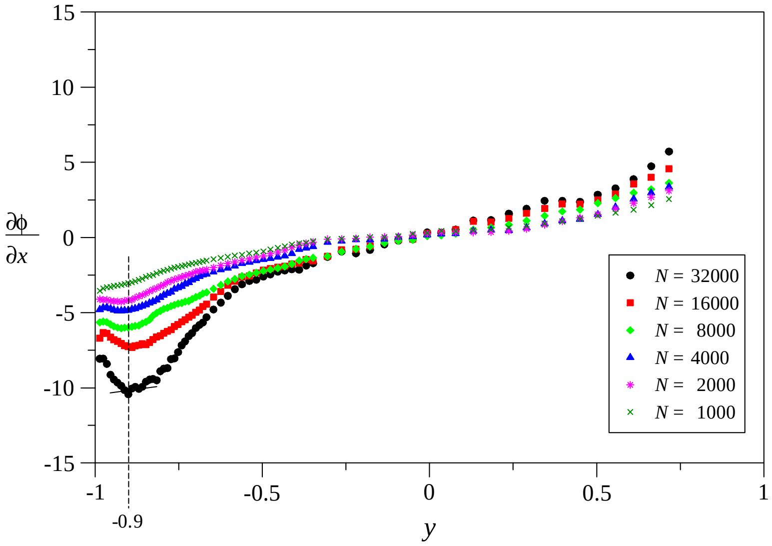

Figure 60: Profiles of axial potential gradient $\partial\phi/\partial x$ (indication of transverse velocity v) at $x \approx 0.01$, $z = 0$ for $Ha = 4000$ and different N.

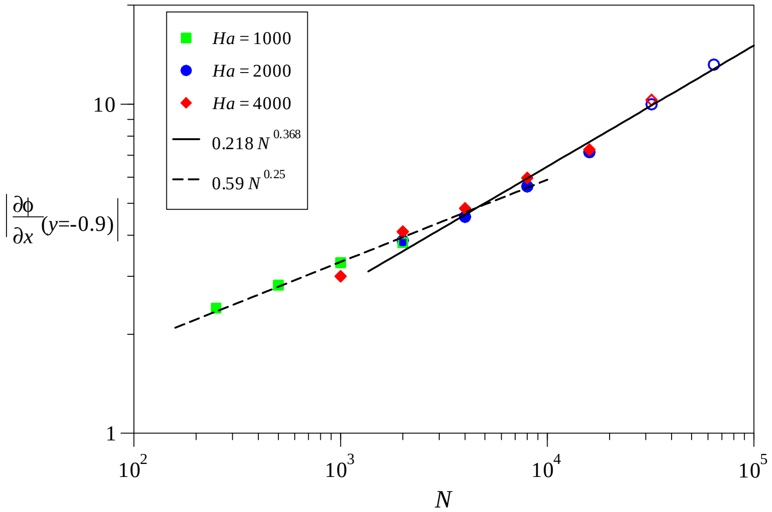

Figure 61: Absolute value of axial potential gradient $|\partial\phi/\partial x|$ (indication of transverse velocity v) at $x \approx 0.01,\ y = -0.9,\ z = 0$ as a function of N for different values of Ha.

flow is then carried by two jets along the side walls. The lower values for u_{core} are found mainly in the range of moderate N since for these parameters the inertial side layers are quite thick so that they are able to carry a larger amount of flow rate. The flow rate carried by the layers is here close to $Q_s \approx 0.75$. With increasing N the side layers become progressively thinner and approach an asymptotic thickness for $N \geq 1000$ as indicated by the fact that the near wall layers close to $y = -1$ do not differ significantly for $N = 1000$ and $N = 2000$. While the layers become thinner, the maximum velocity in the layers increases so that the flow rate carried by the side layers remains close to $Q_s = 0.5$, i.e. roughly half of the flow is still carried by the layers even for the highest N investigated. The velocity signals for u at $N = 500$ showed a very large scattering so that they can not be exploited here. The reason for that reproducible behavior remains unclear since both the results for $N \leq 250$ and for $N \geq 1000$ behave much better. One possible reason could be an instability that occurs just close to $N = 500$.

For $Ha = 2000$ one can observe the above described tendency, i.e. the fact that with increasing N the thickness of the side layers becomes smaller. This situation is shown in Fig. 63. At the transition between the side layers and the core a weak reversed flow can be detected. This latter is even more pronounced for the higher Hartmann number of $Ha = 4000$ as shown in Fig. 64. The thickness of the side layers for large interaction parameters $N \gg 1$ reduces with increasing Hartmann number as can be seen by a comparison of Figs. 62-64.

5.3.3 Surface potential

The instrumentation for measurement of surface potential is described in Sect. A.2.4. In the following, precise measurements of electric potential on one half of the duct surface i.e. for $y < 0$ are supplemented and shown for the entire geometry by assuming symmetry with respect to the vertical plane $y = 0$. The assumption of symmetry has been checked by comparison of two surface potential values on the other half of the duct for $y > 0$, for each cross section. The measured potential values have been scaled by the reference potential $\phi_0 = a u_0 B_0$ and plotted in Figs. 67-71. The results of all measurements can be shortly summarized as follows.

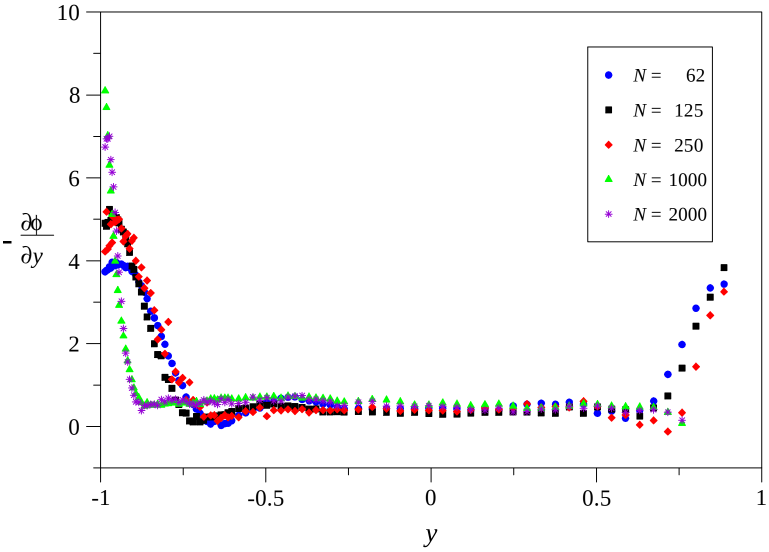

Figure 62: Velocity $u(y) \approx -\partial\phi/\partial y$ at $x = 1.91$, $z = 0$ for $Ha = 1000$ and different N.

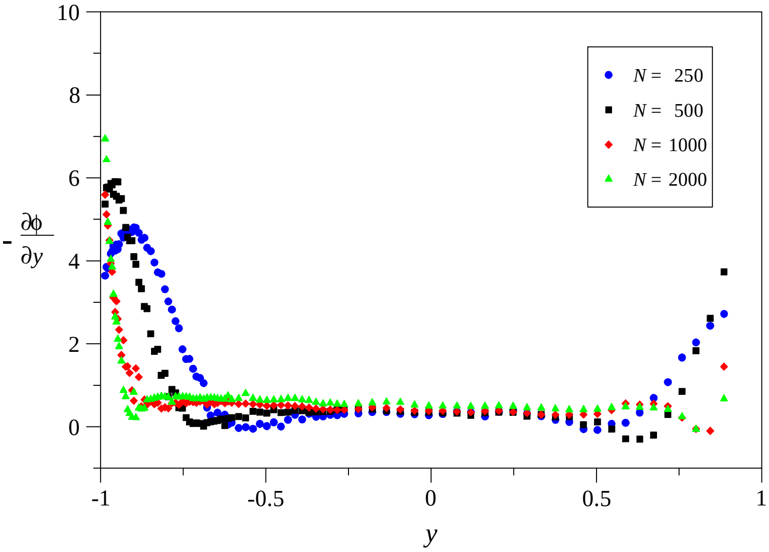

Figure 63: Velocity $u(y) \approx -\partial\phi/\partial y$ at $x = 1.91$, $z = 0$ for $Ha = 2000$ and different N.

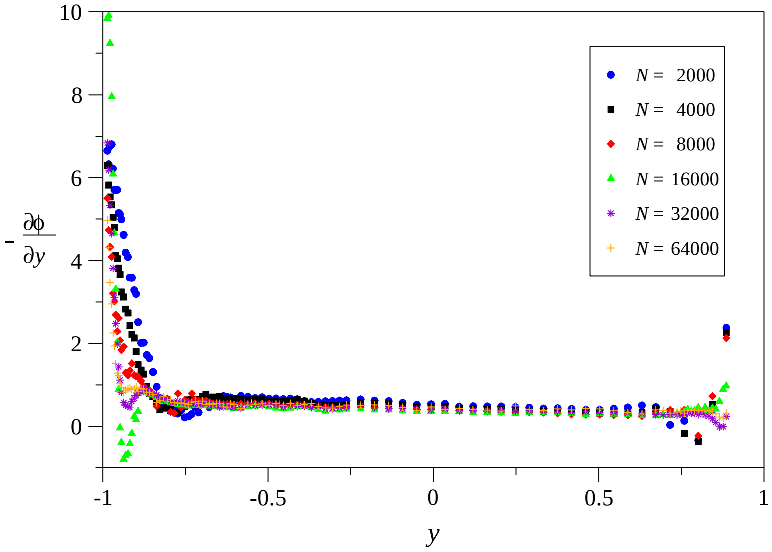

Figure 64: Velocity $u\,(y) \approx -\partial\phi/\partial y$ at $x = 1.91$, $z = 0$ for *Ha* = 4000 and different N.

In the small duct the velocity is four times higher than in the large duct. For that reason the induced transverse potential gradient in the small duct is higher than that in the large one. Far upstream the flow is fully developed. This can be seen by isolines of potential that are perfectly aligned with the flow in Figs. 67-71. When the flow approaches the expansion the transverse potential gradient is reduced and one can observe the 3D distortion of the flow in the vicinity of the expansion on the Hartmann walls and preferentially at the side walls. Further downstream the flow reaches again fully developed conditions where isolines of potential are aligned with the flow. What can be seen from all the figures is that the surface potential, represented in the current scaling, does not vary sensitively changing the magnetic field (*Ha*) or the flow rate (N).

Since the potential may serve as an approximate streamfunction of the flow, its surface contours give a good overall impression of how the flow redistributes at the expansion. The flow follows mainly lines of constant color shown on the Hartmann walls. One can observe that at the expansion the flow is pushed towards the side walls from where it is partly redistributed to the core of the large duct. All these observations are in accordance with measurements of local flow quantities and with theoretical predictions.

Results from a first measuring campaign are shown in Fig. 67(top) for *Ha* = 1000, $N = 1000$. During this campaign potential differences had been measured with reference to a single ground that was connected through a separate cable to the nano-voltmeter. The electric noise that was trapped by the wire loop yielded results that loose their meaning at least behind the expansion, where the signals are very weak. For that reason the wiring was changed in essential parts. In particular the ground was carried through each individual measuring cable and switched also during measurements by a multiplexer. With the new wiring the signal/noise ratio could be improved by far more than an order of magnitude. Results, obtained from a second measuring campaign using the improved wiring, are shown in Fig. 67(middle) for comparison.

In the following we consider in more detail the surface potential of a flow at a moderate Hartmann number *Ha* = 500 and compare the results with numerical simulations in Fig. 66.

The axial positions at which a quantitative comparison is shown are marked in Fig. 65. One can observe the higher potential in the small duct at $x = -3.08$ (higher velocity) and lower values in the large one. All side wall potentials are predicted quite well by the numerical solution, even in the region of strong transition at $x = 0$. Therefore we can conclude that the numerical simulations describe the potential distribution of the MHD flow in an appropriate way, at least up to the Hartmann number of $Ha = 500$.

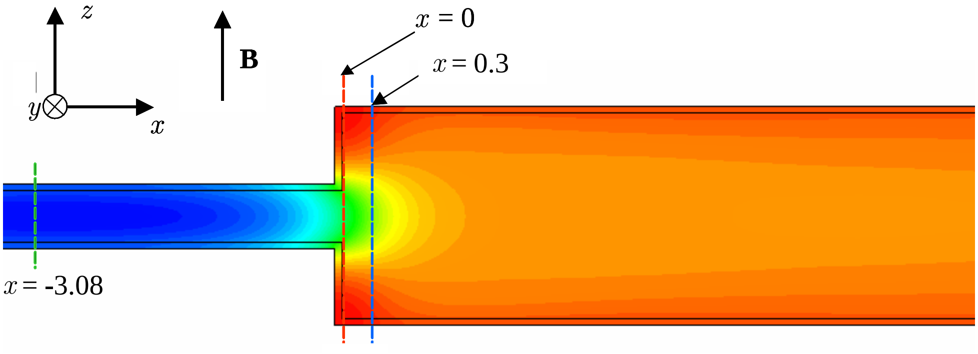

Figure 65: Colored contours of side wall potential for $Ha = 500$, $N = 50$. The figure is shown to indicate the axial positions of potential profiles plotted in Fig. 66.

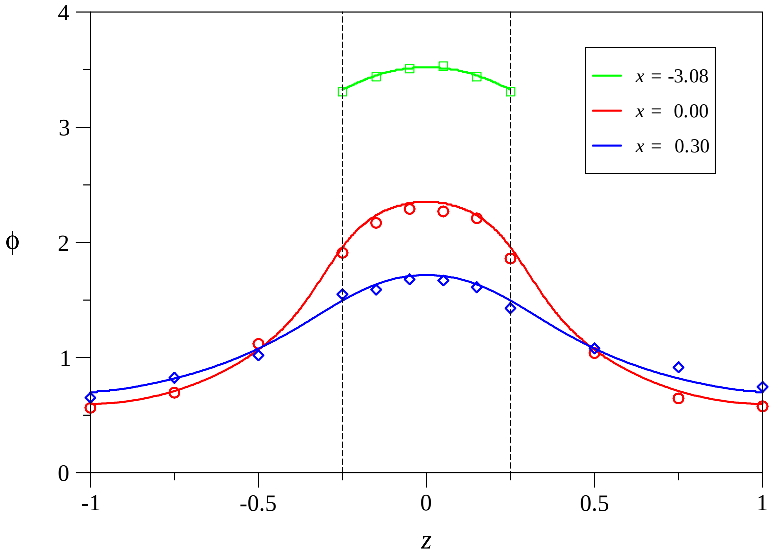

Figure 66: Potential $\phi(z)$ at the side wall $y = -1$ for $Ha = 500$, $N = 50$. Comparison of numerical simulations (solid lines) with experimental results (symbols).

Measurements for higher Hartmann numbers are compared with theoretical results obtained by asymptotic calculations. Results for $Ha = 1000$ and $N = 1000$ are displayed in Fig. 67(middle). Inertia effects seem to play not a decisive role for surface potentials since the results for smaller interaction parameters (not explicitly shown here) do practically not differ from these results. This might have its origin in the fact that 3D inertial currents find their path mainly inside the fluid without influencing too much the wall potential.

For higher Hartmann numbers the situation is analogous, i.e. the inertial influence at the expansion on wall potential seems to be not significant. Results for $Ha = 3000$ are displayed in Fig. 68. A comparison of the results obtained at the interaction parameter $N = 6000$ with the results of the asymptotic theory, displayed in the same figure, shows quite good agreement. This indicates once again that inertia effects on side wall potential are negligible already for $N \geq 6000$. The results are displayed quantitatively in Fig. 70, in which the side wall potential in the horizontal symmetry plane, $\phi\left(x, y=-1, z=0\right)$, is plotted along the axial coordinate x. The most pronounced effect of inertia is here observed rather for the flow in the entrance duct than for the expansion region. This behavior is most probably caused by unstable flows in the side layers of the small channel. This argument is supported by measurements of time-dependent local velocities in the small duct. At higher N those layers stabilize and the potential values converge to the predicted asymptotic solution.

All the behavior explained above is still present if the Hartmann number is progressively increased. Finally qualitative results for $Ha = 5000$ are displayed in Fig. 69 and a quantitative comparison in Fig. 71. The agreement both qualitatively and quantitatively with the asymptotic results becomes even better with increasing the Hartmann number. There could be two reasons for that. One is that side layers remain stable over a wider range of N. The other explanation could be that, once the layer is unstable, the perturbations remain within the layer that becomes thinner and thinner with increasing Ha so that the influence on the global behavior of the flow, expressed through the surface potential, is negligible. Near the expansion a weak inertial dependence of side wall potential remains for the parameters shown.

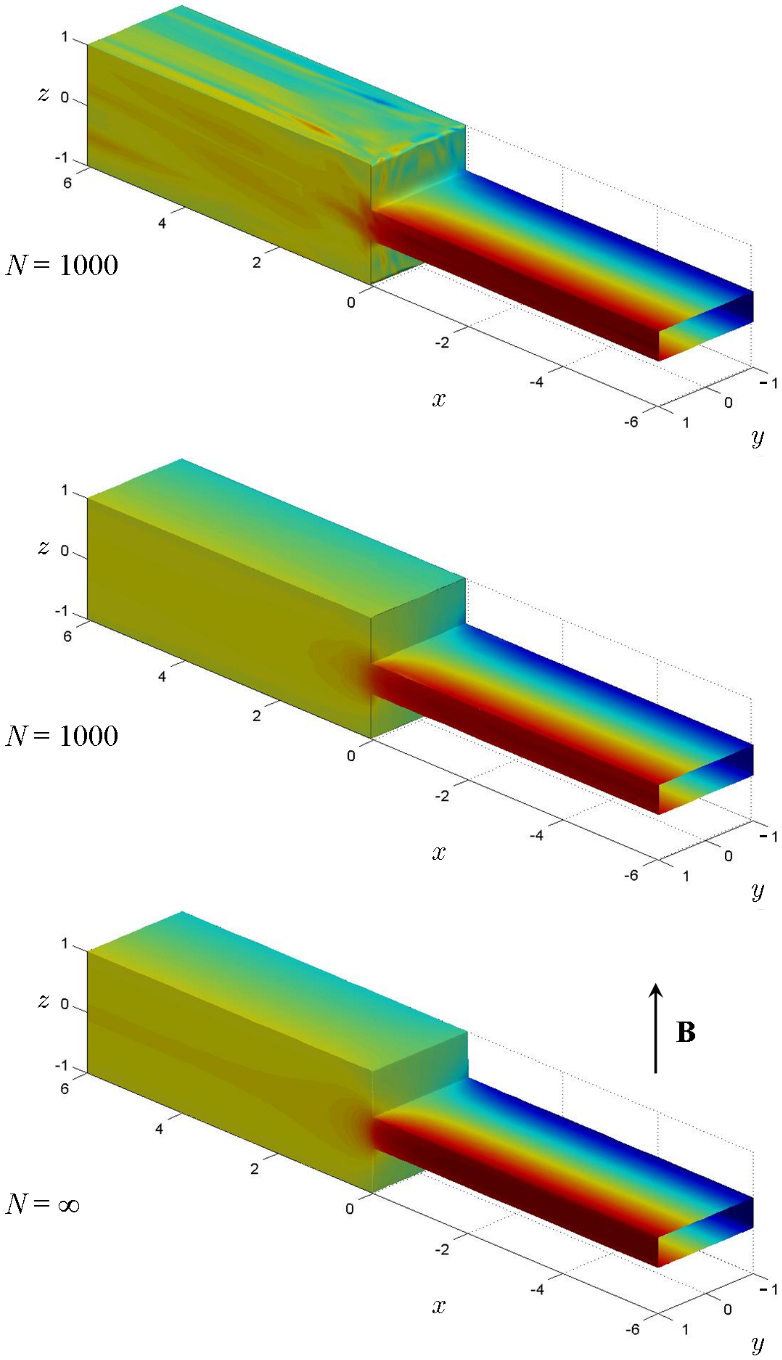

Figure 67: Colored contours of measured surface potential for $Ha = 1000$. Top: $N = 1000$ from an early campaign with insufficient wiring (to highlight the importance of careful instrumentation), middle: $N = 1000$ with improved wiring, bottom: $N = \infty$ from asymptotic theory.

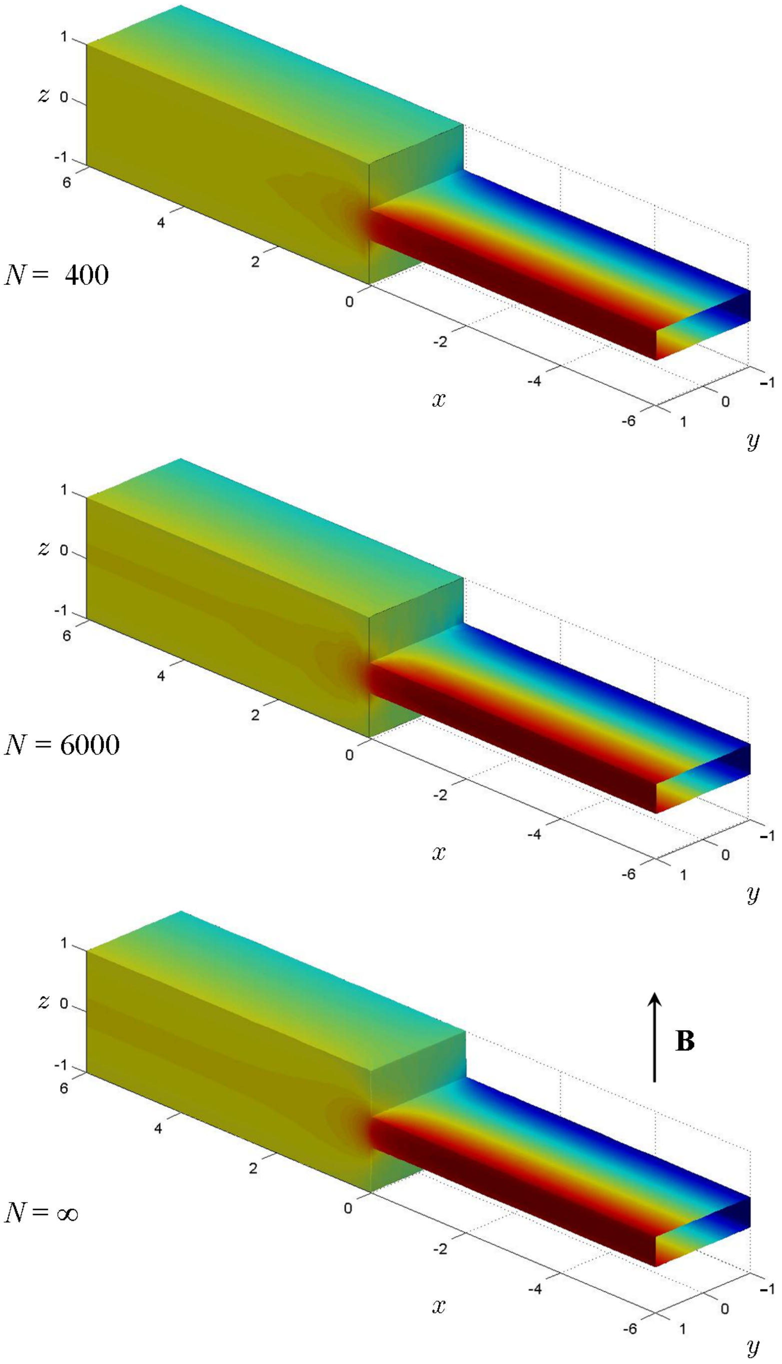

Figure 68: Colored contours of measured surface potential for $Ha = 3000$. Top: $N = 400$, middle: $N = 6000$, bottom: $N = \infty$ from asymptotic theory.

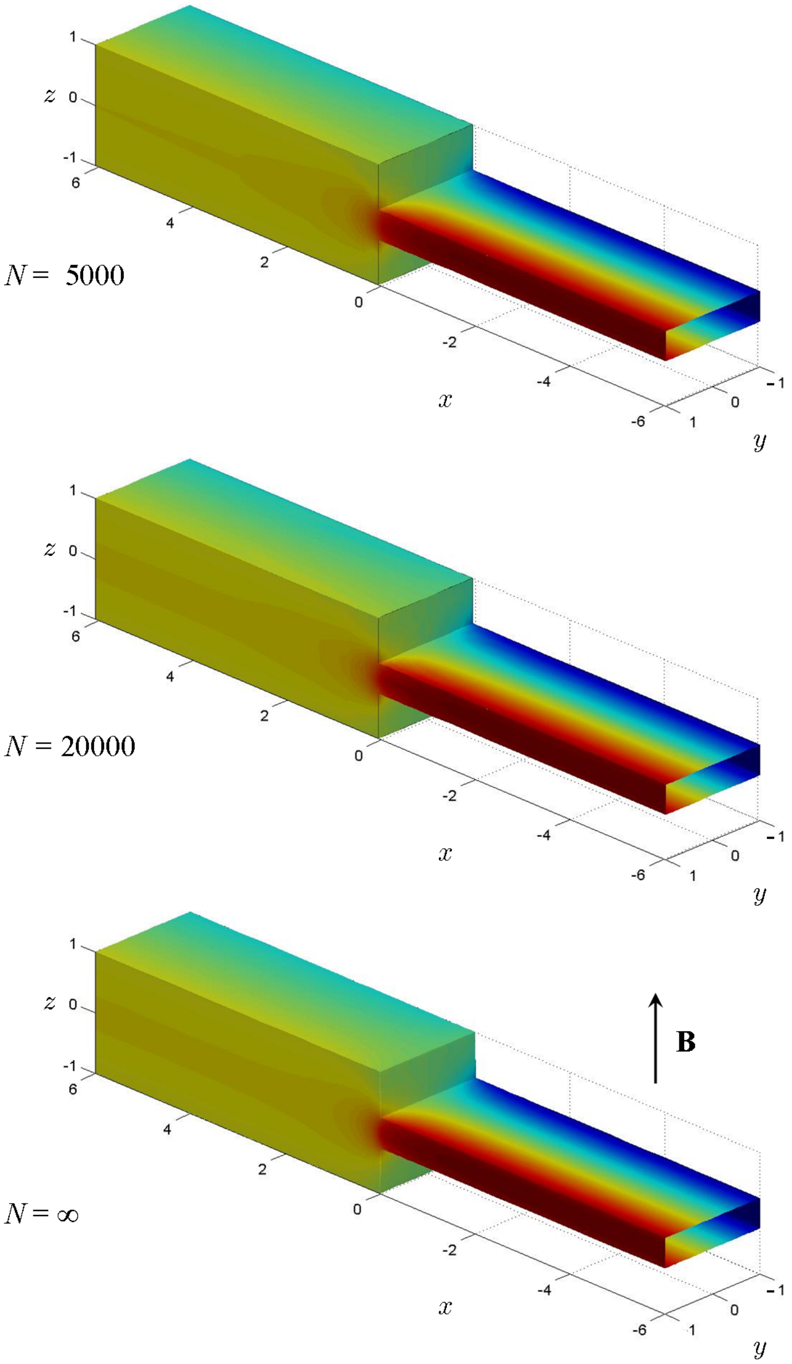

Figure 69: Colored contours of measured surface potential for $Ha = 5000$. Top: $N = 5000$, middle: $N = 20000$, bottom: $N = \infty$ from asymptotic theory.

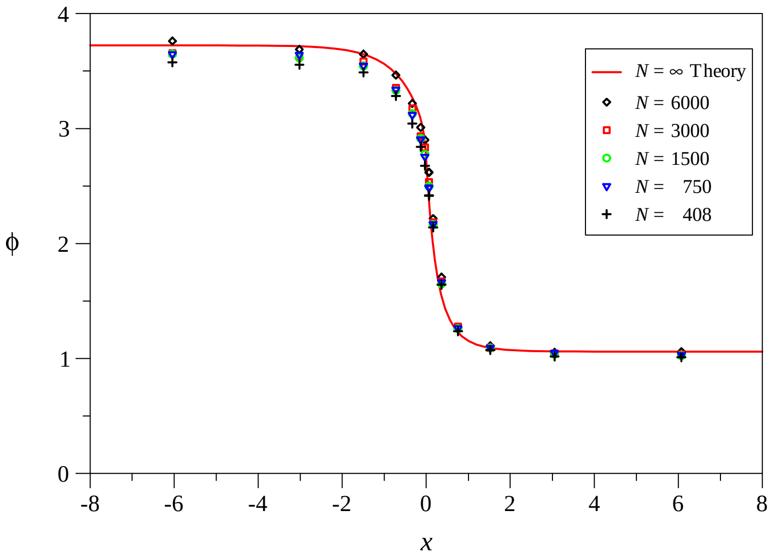

Figure 70: Side wall potential in the plane of symmetry, $\phi\,(x, y = -1, z = 0)$, along the axial coordinate x for $Ha = 3000$.

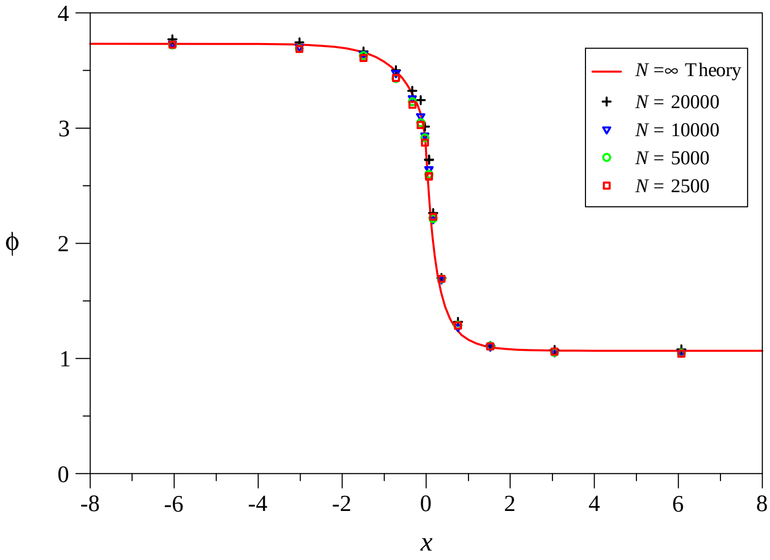

Figure 71: Side wall potential in the plane of symmetry, $\phi\,(x, y = -1, z = 0)$, along the axial coordinate x for $Ha = 5000$.

6 Conclusions

The prediction of three-dimensional MHD flows for applications in fusion engineering, where the Hartmann numbers may exceed even values of $Ha > 10^4$, is still a challenging task since numerical simulations for such flow conditions are beyond the capabilities of modern CFD tools. Also experimentally these values of parameters are hard to reach on laboratory scales. For strong magnetic fields, when electromagnetic forces are much stronger than inertia forces, i.e. for $N \gg 1$, and for smooth geometries, asymptotic techniques based on inertialess approximations may yield quite good results. However, especially for geometries with sudden changes of cross section, inertia effects may still be present in thin parallel layers, where relatively high values of velocity may occur. For such cases only numerical simulations and/or experiments can give the proper insight into the physics involved. Those methods are therefore applied to determine the relevant scaling laws for strong fields, which then allow a physically meaningful extrapolation of data to the desired parameters for engineering applications.

As an example the 3D MHD flow through a sudden expansion of rectangular ducts was considered; For strong magnetic fields results have been obtained by asymptotic theory and compared with experimental results. It was possible to derive the relevant scaling laws for pressure drop as a function of the Hartmann number Ha and the interaction parameter N or the Reynolds number Re. Instead numerical simulations could be performed up to Hartmann numbers $Ha \leq 1000$. As for the inertialess asymptotic analysis, the results have been compared with experiments showing a quite good agreement for the parameters considered. Moreover, the numerical simulations allowed to investigate further the interesting 3D transitions and changes in the topology of the flow in the parameter range between the hydrodynamic case with $Ha = 0$ and the strong field case where $Ha \gg 1$.

In the experiments performed in the MEKKA laboratory of the Forschungszentrum Karlsruhe, Hartmann numbers Ha larger than 5000 and interaction parameters N up to $N = 130\,000$ have been achieved. For such values of parameters the fluid behaves as being inviscid and nearly inertialess in the so-called cores that occupy most of the fluid volume. Viscous (and inertial) effects are confined within thin boundary or internal layers. The flow was investigated through measurements of pressure variation along the upper Hartmann wall, by measuring surface potential on the duct walls and by local potential gradient probes, which were traversed through the channel width at several axial positions.

Measurements of pressure gradients and distribution of surface potential both far upstream and downstream of the expansion showed that the test section is long enough that fully developed flow conditions are well established before the flow reaches the expansion. Moreover, gradients of pressure upstream and downstream of the expansion coincide quite well with those predicted by asymptotic analysis for strong magnetic fields, for $Ha \geq 1000$, or by numerical simulations for moderate fields up to $Ha \leq 1000$. This fact is a good indication that the fluid perfectly wets the walls, i.e. that contact resistance in the experiment is negligible. This condition is a necessary requirement without which a proper comparison with theoretical results cannot be expected.

When approaching the expansion the pressure drops more rapidly compared with fully developed flows due to extra braking Lorentz forces, caused by additional electric current loops present at the expansion. Behind the expansion the pressure gradient is reversed, i.e. part of the pressure drop is recovered by the action of Lorentz forces acting now in flow direction. All these phenomena predicted by the asymptotic analysis and by numerical simulations have been observed experimentally for Hartmann numbers in the range of $500 \leq Ha \leq 5000$.

A comparison of the measured pressure with results from the asymptotic theory valid for $N \rightarrow \infty$, shows that experimentally obtained data points converge monotonically towards the theoretical results as N increases. For the highest values of N that could be reached experimentally, however, one can still observe some weak inertial influence. This indicates that even the highest interaction parameters, which could be realized in the experiments, were not large enough to reach a completely inertialess flow. For smaller values of N, inertia may double the 3D pressure drop in comparison with that in a flow where inertia forces are neglected.

The influence of inertia on pressure drop has been studied by varying the interaction parameter N over a wide range $33 < N < 130\,000$. The measurements indicate clearly that the expansion causes an additional fraction of pressure drop Δp_{3D} due to three-dimensional effects. It has been shown that the influence of inertia and viscous effects can be summarized by a correlation of the type

$$\Delta p_{3D} = 0.315 + 4.76\ Ha^{-1/2} + 0.62 \cdot 10^{-3}\,(Ha\,Re)^{1/3}\,.$$

This additional 3D pressure drop consists of three parts. The first part is present even for inviscid and inertialess flows ($Ha \rightarrow \infty$, $N \rightarrow \infty$) and it depends on the geometry and wall conductivity. The second term accounts for viscous effects and the third one represents the inertial influence. One should note that the first two terms, which have been obtained by an asymptotic numeric approach, fit quite well into the experimental data base. It has been shown, depending on the governing parameters, that viscous and inertia effects may contribute significantly to the 3D pressure drop.

Measurements of surface potential have been performed using an array of more than 300 potential probes distributed with higher density near the expansion. A qualitative and quantitative comparison with the asymptotic theory and with numerical simulations shows quite good agreement. All theoretically predicted features could be observed in the experiments. Since the potential may serve as a hydrodynamic streamfunction for the flow inside the duct, the isolines of potential obtained from the experimental data give already a comprehensive picture of the flow at the expansion.

Approaching the expansion, the flow which was initially carried by the core in the smaller duct is driven towards the sides. Part of that flow enters the upstream side layers in front of the expansion and another part enters directly the large cross section. This fraction is collected by an internal layer from where it is distributed mainly towards the sides. Further downstream a certain amount of fluid is redistributed to the core flow in the large duct. The quantitative comparison of side wall potential with theoretically predicted results is in good agreement for large N. At the expansion a small influence of inertia on the side layer potential remains.

Using traversable probes at the expansion it was possible to determine the local transverse potential gradient $-\partial_y \phi$, which is an indication of the axial velocity component u. As expected from theoretical analyses, the flow in the center of the duct gets depressed and the magnitude of the potential gradient (velocity) near the sides is increased compared to the upstream values. At the expansion maximum values 15 times higher than the average velocity were detected close to the side walls. By increasing the Hartmann number the side layer thickness decreases, the velocity near the side wall increases, and the core becomes more flat.

Inspection near the side walls, at $y = 0.9$, of the local axial potential gradient $\partial_x \phi$, that gives an indication of transverse velocity v, yields at the expansion a typical behavior as

$\partial_x \phi \,(y = 0.9) \sim N^{0.25}$ for $N < 5000$ and $\sim N^{0.37}$ for $N > 5000$. For the highest investigated interaction parameter $N = 64000$ maximum values 13 times larger than the average velocity have been found. These results indicate explicitly that the internal layer remains inertial for all investigated values of N.

The present experiment is the first one that investigates MHD flows in electrically conducting sudden expansions at very high Hartmann numbers and the discussed results extend the existing data base for 3D MHD flows. The results are of fundamental interest not only for applications in fusion but they may serve also as a basis for validation of existing and future computational tools. The experience gained throughout this work shows that numerical techniques for simulating 3D MHD flows may be applied up to Hartmann numbers of about $Ha \lesssim 1000$ with currently available computational resources. Within this parameter range the flow practically completes all major transitions in flow structure from a pure hydrodynamic flow towards a state that is primarily governed by electromagnetic forces. After all these transitions are completed one can apply efficient asymptotic tools to describe the flow in very strong magnetic fields and the error made by neglecting inertia even at sudden expansions remains quite small if $N \gg 1$.

For future improvements of numerical codes for simulations of 3D MHD flows in very strong magnetic fields it would be desirable to implement known wall functions to describe analytically the flow in viscous boundary layers. Such a treatment would remove the restrictions on the Hartmann number since it makes unnecessary resolving the thin layers with a large number of nodes. It would provide a more uniform grid spacing resulting finally in more efficient numerical performance. In order not to depend too strongly on a commercial company, which provides only limited access to the source code and that may change its software versions quite frequently, as directly experienced, a good option could be implementing new models like wall functions in an academic numerical code.

References

Barleon, L., Mack, K.-J. and Stieglitz, R.: 1996, The MEKKA-facility - A flexible tool to investigate MHD-flow phenomena, *Technical Report FZKA 5821*, Forschungszentrum Karlsruhe.

Branover, G. G., Vasil'ev, A. S. and Gel'fgat, Y. M.: 1967, Effect of a transverse magnetic field on the flow in a duct at a sudden cross section enlargement, *Magnetohydrodynamics* **3**(3), 61–65.

Bühler, L.: 1995, Magnetohydrodynamic flows in arbitrary geometries in strong, nonuniform magnetic fields, *Fusion Technology* **27**, 3–24.

Bühler, L.: 2003, Inertialess magnetohydrodynamic flow in expansions and contractions, *Technical Report FZKA 6904*, Forschungszentrum Karlsruhe.

Bühler, L.: 2007, A parametric study of 3D MHD flows in expansions of rectangular ducts, *Fusion Science and Technology* **52**(3), 595–602.

Chang, C. and Lundgren, S.: 1961, Duct flow in magnetohydrodynamics, *Zeitschrift für angewandte Mathematik und Physik* **XII**, 100–114.

Chong, M. S., Perry, A. E. and Cantwell, B. J.: 1989, A general classification of three-dimensional flow fields, *in* H. K. Moffatt and A. Tsinober (eds), *Topological Fluid Mechanics, Proceedings of the IUTAM Symposium*, Cambridge University Press, pp. 408–420.

Délery, J. M.: 2001, Robert Legendre and Henri Werlé: Towards the elucidation of three-dimensional separation, *Annual Review of Fluid Mechanics* **33**, 129–154.

Foust, O. J.: 1972, *Sodium - NaK engineering handbook*, Gordon and Breach Science Publishers.

Gel'fgat, Y. M. and Kit, L. G.: 1971, Investigation of the conditions of occurrence of M-shaped velocity profiles at sudden expansion or contraction of a magnetohydrodynamic flow, *Magnetohydrodynamics* **7**(1), 21–25.

Giancarli, L., Golfier, H., Nishio, S., Raffray, R., Wong, C. and Yamada, R.: 2002, Progress in blanket designs using SiCf/SiC composites, *Fusion Engineering and Design* **61-62**, 307–318.

Hartmann, J.: 1937, Hg-Dynamics I, Theory of the laminar flow of an electrically conductive liquid in a homogeneous magnetic field, *Det Kgl. Danske Videnskabernes Selskab. Mathematisk-fysiske Meddelelser.* **XV**(6), 1–27.

Hartmann, J. and Lazarus, F.: 1937, Hg-Dynamics II, Experimental investigations on the flow of mercury in a homogeneous magnetic field, *Det Kgl. Danske Videnskabernes Selskab. Mathematisk-fysiske Meddelelser.* **XV**(7), 1–45.

Hunt, J. C. R.: 1965, Magnetohydrodynamic flow in rectangular ducts, *Journal of Fluid Mechanics* **21**, 577–590.

Hunt, J. C. R. and Leibovich, S.: 1967, Magnetohydrodynamic flow in channels of variable cross-section with strong transverse magnetic fields, *Journal of Fluid Mechanics* **28**(Part 2), 241–260.

Kulikovskii, A. G.: 1974, Flows of a conducting incompressible liquid in an arbitrary region with a strong magnetic field, *Fluid Dynamics* **8**(1), 462–467. Russian original (1973).

Legendre, R.: 1956, Séparation de l'écoulement laminaire tridimensionnel, *La Recherche Aéronautique* **54**, 3–8.

Mistrangelo, C.: 2005, *Three-dimensional MHD flow in sudden expansions*, PhD thesis, Universität Karlsruhe.

Mistrangelo, C. and Bühler, L.: 2005, Three-dimensional magnetohydrodynamic flows in sudden expansions, *Proceedings of the Joint 15th Riga and 6th Pamir International Conference, Riga, June 27-July*, Vol. 1, pp. 239–242.

Mistrangelo, C. and Bühler, L.: 2007, Numerical investigation of liquid metal flows in rectangular sudden expansions, *Fusion Engineering and Design* **82**(15-24), 2176–2182.

Molokov, S. and Bühler, L.: 1994, Liquid metal flow in a U-bend in a strong uniform magnetic field, *Journal of Fluid Mechanics* **267**, 325–352.

Moreau, R.: 1990, *Magnetohydrodynamics*, Kluwer Academic Publisher.

Mück, B., Günther, C., Müller, U. and Bühler, L.: 2000, Three-dimensional MHD flows in rectangular ducts with internal obstacles, *Journal of Fluid Mechanics* **418**, 265–295.

Müller, U. and Bühler, L.: 2001, *Magnetofluiddynamics in Channels and Containers*, Springer, Wien, New York. ISBN 3-540-41253-0.

Oertel, H.: 2004, *Prandtl's Essentials of Fluid Mechanics*, Vol. 158 of *Applied Mathematical Sciences*, second edn, Springer.

Picologlou, B. F., Reed, C. B., Hua, T. Q., Barleon, L., Kreuzinger, H. and Walker, J. S.: 1989, MHD flow tailoring in first wall coolant channels of self-cooled blankets, *Fusion Engineering and Design* **8**, 297–303.

Shercliff, J. A.: 1953, Steady motion of conducting fluids in pipes under transverse magnetic fields, *Proc.Camb.Phil.Soc.* **49**, 136–144.

Stahl-Eisen-Werkstoffblätter: 1992, *Physikalische Eigenschaften von Stählen*, Verein Deutscher Eisenhüttenleute.

Sterl, A.: 1990, Numerical simulation of liquid-metal MHD flows in rectangular ducts, *Journal of Fluid Mechanics* **216**, 161–191.

Tillack, M. S. and McCarthy, K.: 1989, Flow quantity in side layers for MHD flow in conducting rectangular ducts, *Technical Report UCLA-IFNT-89-01*, University of California, Los Angeles.

Walker, J. S.: 1981, Magnetohydrodynamic flows in rectangular ducts with thin conducting walls, *Journal de Mécanique* **20**(1), 79–112.

Walker, J. S.: 1986a, Laminar duct flows in strong magnetic fields, *in* H. Branover, P. S. Lycoudis and M. Mond (eds), *Liquid-metal flows and magnetohydrodynamics*, American Institute of Aeronautics and Astronautics.

Walker, J. S.: 1986b, Liquid metal flow through a thin walled elbow in a plane perpendicular to a uniform magnetic field, *Int. J. Engng. Sci.* **24**(11), 1741–1754.

Walker, J. S., Ludford, G. S. S. and Hunt, J. C. R.: 1971, Three-dimensional MHD duct flows with strong transverse magnetic fields. Part 2. Variable-area rectangular ducts with conducting sides, *Journal of Fluid Mechanics* **46**, 657–684.

Walker, J. S., Ludford, G. S. S. and Hunt, J. C. R.: 1972, Three-dimensional MHD duct flows with strong transverse magnetic fields. Part 3. Variable-area rectangular ducts with insulating walls, *Journal of Fluid Mechanics* **56**, 121–141.

Widlund, O.: 2003, Wall functions for numerical modeling of laminar MHD flows, *European Journal of Mechanics - B/Fluids* **22**(3), 221–237.

A Appendix

A.1 Asymptotic analysis

A.1.1 Side layers

Axial velocity It has been shown in Sect 3.3 that the viscous correction to the side layer potential and velocity take the form

$$\phi_s = \sum_{k=0}^{\infty} \left(a_k \cos \alpha_k \eta + b_k \sin \alpha_k \eta\right) \exp \alpha_k \eta \, \cos \beta_k z, \tag{85}$$

and

$$u_s = -\sum_{k=0}^{\infty} Ha^{1/2} \alpha_k \left[(b_k + a_k) \cos \alpha_k \eta + (b_k - a_k) \sin \alpha_k \eta\right] \exp \alpha_k \eta \, \cos \beta_k z, \tag{86}$$

where

$$\beta_k = \frac{2k+1}{2} \frac{\pi}{Z}, \quad \alpha_k = -\sqrt{\beta_k / 2}. \tag{87}$$

Boundary conditions $\phi = \phi_w$ and $u = 0$ provide matching conditions at the side wall $\eta = 0$ for determining the unknown coefficients a_k and b_k from

$$\left.\begin{aligned} \phi_w = \phi_c + \phi_s = &\quad \phi_c + \textstyle\sum a_k \cos \beta_K z \\ 0 = u_c + u_s = &\quad u_c - \textstyle\sum \underbrace{Ha^{1/2} \alpha_k \left(b_k + a_k\right)}_{u_k} \cos \beta_k z \end{aligned}\right\} \text{ at } \eta = 0. \tag{88}$$

The coefficients a_k and u_k correspond to the Fourier coefficients of viscous potential and velocity taken at the position $y = -1$ (at $\eta = 0$). While the core values ϕ_c and u_c are independent of the field aligned coordinate according to (26) and (27), the value ϕ_w, known from the numerical solution depends on z.

By using orthogonality of trigonometric functions the equations determining the a_k and u_k are found as

$$a_k = \frac{2}{Z} \int_0^Z \left(\phi_w - \phi_c\right) \cos \beta_k z \, dz, \tag{89}$$

$$u_k = \frac{2}{Z} \int_0^Z u_c \cos \beta_k z \, dz, \tag{90}$$

which determine the last coefficient

$$b_k = -a_k + \frac{1}{\alpha_k Ha^{1/2}} u_k$$

for the side layer velocity in (86). The analysis follows the ideas of Walker (1981) who calculated the coefficients up to the leading order in Ha.

We have seen in (27) that the core velocity u_c is uniform along magnetic field lines. This simplifies the calculation for u_k and we obtain

$$u_k = 2 u_c \frac{\sin Z\beta_k}{Z\beta_k}. \tag{91}$$

The core potential ϕ_c is constant along field lines but the potential difference $(\phi_w - \phi_c)$ depends on z. The values $(\phi_w - \phi_c)$ are known at discrete locations as a result from the numerical calculations. For evaluating the expression (89) we assume that for the simplest case the potential varies like a piecewise linear function between the numerically known values at the ends of a line element l. This yields

$$a_k = \frac{2}{Z\beta_k^2} \sum_{l=1}^{n} [\phi_w - \phi_c]_l \, \frac{[\cos \beta_k z]_l}{[z]_l}, \tag{92}$$

where $[\ ]_l$ stands for the difference of a quantity taken between the two nodes of the line element l. The summation over all n line elements approximates the value of the integral (89). This procedure ensures convergence for $k \to \infty$. in contrast to an approximation that would take $\phi_w - \phi_c$ at a finite number of collocation points.

Vertical velocity As outlined in Sect. 3.3.2, the vertical velocity in the side layer can be obtained by the solution of (24) in stretched coordinates in the form of

$$\partial_\eta^4 w = \partial_{zz} w. \tag{93}$$

It was shown that a viscous solution for w, which vanishes at large distance from the side wall and which satisfies no-slip at the wall reads as

$$w = Ha^{1/2} \sum_{k=1}^{\infty} w_k \sin \alpha_k \eta \, \exp \alpha_k \eta \, \sin \beta_k z, \tag{94}$$

where as a scale for the order of magnitude of side layer velocity the factor $Ha^{1/2}$ has been introduced and

$$\beta_k = \frac{1}{Z} k\pi, \qquad \alpha_k = - \sqrt{\beta_k / 2}. \tag{95}$$

The coefficients w_k are obtained by conservation of mass as outlined in the following. Mass conservation requires that

$$\partial_z w = -\partial_x u - \partial_y v. \tag{96}$$

Integration across the side layers results in

$$\int_0^\infty \partial_z w \, d\eta = - \int_0^\infty \partial_x u \, d\eta - \sqrt{Ha} \, (v_c - v_w) \tag{97}$$

and gives with (40) and with velocity component $v_w = 0$ at the wall

$$\int_0^\infty \partial_z w \, d\eta = \sqrt{Ha} \int_0^\infty \partial_\eta \partial_x \phi_s \, d\eta - \sqrt{Ha} v_c \tag{98}$$

from which we obtain

$$Ha^{-1/2} \int_0^\infty \partial_z w \, d\eta = \partial_x (\phi_c - \phi_w) - v_c. \tag{99}$$

After using the Fourier expansion for w the equation reads as

$$\int_0^\infty \sum_{k=1}^{\infty} \beta_k w_k \sin \alpha_k \eta \, \exp \alpha_k \eta \, \cos \beta_k z \, d\eta = \partial_x (\phi_c - \phi_w) - v_c \tag{100}$$

and evaluation of the integral yields

$$\sum_{k=1}^{\infty} \alpha_k w_k \cos \beta_k z = \partial_x (\phi_c - \phi_w) - v_c. \tag{101}$$

Orthogonality of trigonometric functions determines the coefficients as

$$\alpha_k w_k = -\frac{2}{Z} \int_0^Z \partial_x \phi_w \cos \beta_k z \, dz. \tag{102}$$

A.1.2 Expansion layer

Potential and transverse velocity It has been shown in Sect. 3.4.1 that the viscous corrections for potential and velocity are represented for $\xi > 0$ as:

$$\phi_E = \sum_{K=0}^{\infty} (A_K \cos \alpha_K \xi + B_K \sin \alpha_K \xi) \exp \alpha_K \xi \, \cos \beta_K z, \tag{103}$$

$$v_E = \sum_{K=0}^{\infty} Ha^{1/2} \alpha_K \left[(B_K + A_K) \cos \alpha_K \xi + (B_K - A_K) \sin \alpha_K \xi \right] \exp \alpha_K \xi \, \cos \beta_K z, \tag{104}$$

and for $\xi < 0$ as

$$\phi_e = \sum_{k=0}^{\infty} (a_k \cos \alpha_k \xi + b_k \sin \alpha_k \xi) \exp \alpha_k \xi \, \cos \beta_k z, \tag{105}$$

$$v_e = \sum_{k=0}^{\infty} Ha^{1/2} \alpha_k \left[(a_k + b_k) \cos \alpha_k \xi + (b_k - a_k) \sin \alpha_k \xi \right] \exp \alpha_k \xi \, \cos \beta_k z, \tag{106}$$

where

$$\beta_K = \frac{2K+1}{2} \frac{\pi}{Z_C}, \quad \alpha_K = -\sqrt{\beta_K/2}. \tag{107}$$

$$\beta_k = \frac{2k+1}{2} \frac{\pi}{Z_c}, \quad \alpha_k = +\sqrt{\beta_k/2}. \tag{108}$$

Matching conditions for ϕ and v at $\xi = 0$, namely

$$\left. \begin{array}{rr} \phi = \phi_C + \phi_E = & \phi_C + \sum A_K \cos \beta_K z \\ v = v_C + v_E = & v_C + \sum \underbrace{Ha^{1/2} \alpha_K (B_K + A_K)}_{V_K} \cos \beta_K z \end{array} \right\} \text{ at } \xi = 0 \tag{109}$$

$$\left. \begin{array}{rr} \phi = \phi_c + \phi_e = & \phi_c + \sum a_k \cos \beta_k z \\ v = v_c + v_e = & v_c + \sum \underbrace{Ha^{1/2} \alpha_k (a_k + b_k)}_{v_k} \cos \beta_k z \end{array} \right\} \text{ at } \xi = 0 \tag{110}$$

are used to determine the unknown coefficients A_K, B_K and a_k, b_k. The coefficients A_K and V_K correspond to the Fourier coefficients of viscous potential and velocity taken at the position

$\xi = 0$. While the core values are independent of the field aligned coordinate according to (26) and (27), the values ϕ and v at $\xi = 0$ do depend on z.

Elimination of ϕ and v at $\xi = 0$ from (109) and (110) yields

$$\phi_C + \sum_K A_K \cos \beta_K z = \begin{cases} \phi_w & \text{for } Z_c < z < Z_C \\ \phi_c + \sum_k a_k \cos \beta_k z & \text{for } 0 < \ z \leq Z_c \end{cases}, \tag{111}$$

$$v_C + \sum_K V_K \cos \beta_K z = \begin{cases} 0 & \text{for } Z_c < z < Z_C \\ v_c + \sum_k v_k \cos \beta_k z & \text{for } 0 < \ z \leq Z_c \end{cases}. \tag{112}$$

The potential and the velocity at $\xi = 0$ are given by the expressions shown in (110) for $0 < z \leq Z_c$. For $Z_c < z < Z_C$, however, the potential $\phi\,(\xi = 0)$ equals the wall potential ϕ_w and the velocity at the solid wall vanishes. We find by using orthogonality of trigonometric functions and with the abbreviations

$$\Delta\phi = \begin{cases} \phi_w - \phi_C \\ \phi_c - \phi_C \end{cases} \quad \text{and} \quad \Delta v = \begin{cases} 0 - v_C & \text{for } Z_c < z < Z_C \\ v_c - v_C & \text{for } 0 < \ z \leq Z_c \end{cases} \tag{113}$$

the equations determining the A_K and B_K as

$$\frac{1}{2} A_K = \frac{1}{Z_C} \left(\sum_k a_k \int_0^{Z_c} \cos \beta_k z \cos \beta_K z \, dz + \int_0^{Z_C} \Delta\phi \cos \beta_K z \, dz \right), \tag{114}$$

$$\frac{1}{2} V_K = \frac{1}{Z_C} \left(\sum_k v_k \int_0^{Z_c} \cos \beta_k z \cos \beta_K z \, dz + \int_0^{Z_C} \Delta v \cos \beta_K z \, dz \right). \tag{115}$$

So far the coefficients A_K and V_K (B_K) satisfy continuity of potential and velocity at $\xi = 0$ for any given expansion of the solution in terms of a_k and v_k (b_k).

Continuity of shear stress (vorticity) at $\xi = 0$ is used now to derive equations for a_k and b_k, i.e.

$$\partial_{\xi\xi} \phi_e \,(\xi = -0) = \partial_{\xi\xi} \phi_E \,(\xi = +0) \,. \tag{116}$$

We obtain now

$$\sum_k \alpha_k^2 b_k \cos \beta_k z = \sum_K \alpha_K^2 B_K \cos \beta_K z, \tag{117}$$

and after using orthogonality we find

$$\frac{1}{2} Z_c \alpha_k^2 b_k = \sum_K B_K \alpha_K^2 \int_0^{Z_c} \cos \beta_K z \cos \beta_k z \, dz. \tag{118}$$

If we further assume that the vorticity field is smooth at $\xi = 0$,

$$\partial_\xi^3 \phi_e \,(\xi = -0) = \partial_\xi^3 \phi_E \,(\xi = +0) \,, \tag{119}$$

we find the equation

$$\sum_k \alpha_k^3 \,(b_k - a_k) \cos \beta_k z = \sum_K \alpha_K^3 \,(B_K - A_K) \cos \beta_K z, \tag{120}$$

from which we determine

$$\frac{1}{2}Z_c\alpha_k^3\left(b_k-a_k\right)=\sum_K\left(B_K-A_K\right)\alpha_K^3\int_0^{Z_c}\cos\beta_K z\cos\beta_k z\,dz. \tag{121}$$

In the next step we substitute the integrals as

$$\begin{aligned}C_{kK} &= 2\int_0^{Z_c}\cos\beta_K z\cos\beta_k z\,dz=2\frac{\beta_k\cos Z_c\beta_K\sin Z_c\beta_k}{\beta_k^2-\beta_K^2}, &(122)\\ \Delta\phi_K &= \frac{2}{Z_C}\int_0^{Z_C}\Delta\phi\cos\beta_K z\,dz,\quad \Delta v_K=\frac{2}{Z_C}\int_0^{Z_C}\Delta v\cos\beta_K z\,dz. &(123)\end{aligned}$$

Note, there is a possibility that the denominator in (122) vanishes if $\beta_K\to\beta_k$. For such a case it can be shown, however, that C_{kK} remains finite:

$$\lim_{\beta_K\to\beta_k}C_{kK}=Z_c. \tag{124}$$

The core velocities are uniform along field lines so that Δv becomes a piecewise constant function along z. The Fourier coefficients evaluate analytically as

$$\begin{aligned}\Delta v_K &= \frac{2}{Z_C}\left(\int_0^{Z_c}\left(v_c-v_C\right)\cos\beta_K z\,dz+\int_{Z_c}^{Z_C}\left(-v_C\right)\cos\beta_K z\,dz\right)\\ &= \frac{2}{Z_C\beta_K}\left(v_c\sin\beta_K Z_c-v_C\sin\beta_K Z_C\right). &(125)\end{aligned}$$

The values v_c and v_C have to be taken from the asymptotic numerical solution. The function $\Delta\phi\left(z\right)$ is not known analytically but may be approximated in the simplest case as a continuous piecewise linear function that connects the numerically obtained potential data. Analytic integration of the piecewise function yields

$$\Delta\phi_K=\frac{2}{\beta_K^2Z_C}\sum_{l=1}^{n}\left[\Delta\phi\right]_l\frac{\left[\cos\beta_K z\right]_l}{\left[z\right]_l}, \tag{126}$$

where $[\;]_l$ stands for the difference of a quantity taken between two nodes of the computational grid. This procedure ensures convergence as $K\to\infty$ in contrast to an approximation that would take $\Delta\phi$ at a finite number of collocation points.

The final system of equations that determines the solution of the flow in the expansion layer reads as

$$\begin{aligned}A_K &= \frac{1}{Z_C}\sum_k a_kC_{kK}+\Delta\phi_K, &(127)\\ V_K &= \frac{1}{Z_C}\sum_k v_kC_{kK}+\Delta v_K. &(128)\end{aligned}$$

With $v_k=Ha^{1/2}\alpha_k\left(a_k+b_k\right)$ and $B_K=-A_K+\frac{V_K}{\alpha_K Ha^{1/2}}$ the latter equation determines B_K as

$$B_K=-A_K+\frac{1}{Z_C}\frac{1}{\alpha_K}\sum_k\alpha_k\left(a_k+b_k\right)C_{kK}+\frac{1}{\alpha_K Ha^{1/2}}\Delta v_K.$$

The system of equations is finally closed by the determination of the coefficients a_k and b_k. We summarize the governing equations as follows:

$$\begin{aligned} A_K &= \frac{1}{Z_C}\sum_k a_k C_{kK} + \Delta\phi_K & (129)\\ B_K &= -A_K + \frac{1}{Z_C\alpha_K}\sum_k \alpha_k\left(a_k+b_k\right)C_{kK} + \frac{1}{\alpha_K Ha^{1/2}}\Delta v_K & (130)\\ b_k &= \frac{1}{Z_c\alpha_k^2}\sum_K \alpha_K^2 B_K C_{kK}, & (131)\\ a_k &= b_k - \frac{1}{Z_c\alpha_k^3}\sum_K \alpha_K^3\left(B_K-A_K\right)C_{kK}. & (132)\end{aligned}$$

We see already that the problem is mainly governed by core potentials and that the corrections due to core velocity become unimportant as $Ha \to \infty$. For a numerical solution of the problem the series are truncated at a finite number of modes and the solution is obtained by an iterative process. Initially $a_k = b_k = 0$ is assumed and first estimates of A_K and B_K are calculated. Then b_k and a_k are updated and a better approximation for A_K and B_K is obtained. This procedure is repeated (with underrelaxation if necessary) until A_K, B_K and a_k, b_k approach their final constant values.

Vertical velocity For deriving an equation for vertical velocity in the expansion layer we use (24) in stretched coordinates as

$$\partial_\xi^4 w = \partial_{zz} w. \tag{133}$$

At large distance from the expansion the solution for w requires that

$$w = \partial_\xi w = 0 \text{ as } \xi \to \pm\infty. \tag{134}$$

The boundary conditions at Hartmann walls are

$$w = 0 \text{ at } z = Z_c, Z_C \tag{135}$$

and symmetry implies that

$$w = 0 \text{ at } z = 0. \tag{136}$$

At the vertical wall of the expansion, for $Z_c < z < Z_C$, we have no-slip and zero normal component of velocity,

$$w = 0 \text{ and } u = 0 \text{ at } \xi = 0. \tag{137}$$

In general, the axial component u of velocity evaluates at leading order from Ohm's law as

$$u = -\partial_x p - \partial_y \phi. \tag{138}$$

The variables and expressions for u, $\partial_x p$, and $\partial_y \phi$ are used for continuous matching at $\xi = 0$ for $0 < z < Z_c$.

As before we split the expansion domain in two regions and define the vertical velocity as

$$w = \left\{ \begin{array}{ccc} Ha^{1/2} w_e & & \xi < 0 \\ & \text{for} & \\ Ha^{1/2} w_E & & \xi > 0\ . \end{array} \right. \tag{139}$$

By separation of variables we find viscous solutions for w, which vanish at large distance from the expansion in the form

$$\begin{aligned} w_E &= \sum_{K=1}^{\infty} \left(A_K \cos \alpha_K \xi + B_K \sin \alpha_K \xi\right) \exp \alpha_K \xi \ \sin \beta_K z, & (140) \\ w_e &= \sum_{k=1}^{\infty} \left(a_k \cos \alpha_k \xi + b_k \sin \alpha_k \xi\right) \exp \alpha_k \xi \ \sin \beta_k z, & (141) \end{aligned}$$

where

$$\begin{array}{ll} \beta_K = \frac{1}{Z_C} K \pi, & \alpha_K = -\sqrt{\beta_K / 2}, \\ \beta_k \ = \frac{1}{Z_c} k \pi, & \alpha_k \ = \ \sqrt{\beta_k / 2}. \end{array} \tag{142}$$

At $\xi = 0$ we smoothly match both solutions up to the second derivatives:

$$\sum_K A_K \ \sin \beta_K z = \left\{ \begin{array}{c} 0 \\ \sum_k a_k \ \sin \beta_k z \end{array} \right. \ \text{for} \ \begin{array}{c} Z_c < z < Z_C \\ 0 < z < Z_c \end{array} , \tag{143}$$

$$\sum_K \alpha_K \ \left(B_K + A_K\right) \sin \beta_K z = \sum_k \alpha_k \ \left(b_k + a_k\right) \sin \beta_k z \text{ for } 0 < z < Z_c, \tag{144}$$

$$\sum_K {\alpha_K}^2 B_K \sin \beta_K z = \sum_k \alpha_k^2 \, b_k \sin \beta_k z \text{ for } 0 < z < Z_c\ . \tag{145}$$

The fourth condition for matching is obtained by consideration of vertical fluxes as described below. The vertical component of velocity is related to pressure according to (21) at leading order as

$$\partial_{xx} p = \partial_z w \tag{146}$$

Integration along x yields the variation with z of the flow rate carried by the layer in the vertical direction, i.e.

$$\begin{aligned} \partial_x p_C - \partial_x p_{0+} &= \int_0^{\infty} \partial_z w_E d\xi, & (147) \\ \partial_x p_{0-} - \partial_x p_c &= \int_{-\infty}^{0} \partial_z w_e d\xi, & (148) \end{aligned}$$

where $\partial_x p_{0\pm} = \partial_x p\left(\xi = \pm 0\right)$ are the left and right sided limits of pressure gradient. Matching of pressure gradients (potential and velocity) at $\xi = 0$ leads us to

$$\int_0^{\infty} \partial_z w_E d\xi = G\left(z\right) - \left\{ \begin{array}{ccc} 0 & & Z_c < z < Z_C \\ & \text{for} & \\ \int_{-\infty}^{0} \partial_z w_e d\xi & & 0 < z < Z_c \end{array} \right. , \tag{149}$$

where

$$G(z) = \left\{ \begin{array}{ccc} \partial_x p_C - \partial_x p_{0+}(z) & & Z_c < z < Z_C \\ & \text{for} & \\ \partial_x p_C - \partial_x p_c & & 0 < z < Z_c \end{array} \right. . \tag{150}$$

For efficient calculation of (150) we substitute the pressure gradient according to $\partial_x p = -(u + \partial_y \phi)$, i.e.

$$G(z) = \left\{ \begin{array}{cccc} 0 - u_C & +\partial_y (\phi_w(z) - \phi_C) & & Z_c < z < Z_C \\ & & \text{for} & \\ u_c - u_C & +\partial_y (\phi_c - \phi_C) & & 0 < z < Z_c \end{array} \right. \tag{151}$$

and we use of the 2D streamfunction as $u_{c,C} = -\frac{1}{Z_{c,C}} \partial_y \psi_{c,C}$ to find

$$G(z) = \partial_y \left\{ \begin{array}{cccc} \frac{1}{Z_C}\psi_C & +\phi_w(z) - \phi_C & & Z_c < z < Z_C \\ & & \text{for} & \\ \frac{1}{Z_C}\psi_C - \frac{1}{Z_c}\psi_c & +\phi_c - \phi_C & & 0 < z < Z_c \end{array} \right. . \tag{152}$$

Integration of (149) along z yields

$$\int_0^\infty w_E d\xi = \int_0^z G(z)\,dz - \left\{ \begin{array}{c} 0 \\ \int_{-\infty}^0 w_e d\xi \end{array} \right. \text{ for } \begin{array}{c} Z_c < z < Z_C \\ 0 < z < Z_c \end{array} . \tag{153}$$

Inserting the ansatz for w_E and w_e gives

$$\frac{1}{2} \sum_K \frac{B_K - A_K}{\alpha_K} \sin \beta_K z = \int_0^z G(z)\,dz + \left\{ \begin{array}{c} 0 \\ \frac{1}{2} \sum_k \frac{b_k - a_k}{\alpha_k} \sin \beta_k z \end{array} \right. \text{ for } \begin{array}{c} Z_c < z < Z_C \\ 0 < z < Z_c \end{array} \tag{154}$$

and orthogonality determines the coefficients as

$$\frac{B_K - A_K}{\alpha_K} = \frac{4}{Z_C} \int_0^{Z_C} \left(\int_0^z G(z')\,dz' \sin \beta_K z \right) dz + \frac{1}{Z_C} \sum_k \frac{b_k - a_k}{\alpha_k} S_{kK}, \tag{155}$$

with the abbreviation

$$S_{kK} = 2 \int_0^{Z_c} \sin \beta_k z \sin \beta_K z \, dz = \frac{2\beta_k}{\beta_K^2 - \beta_k^2} \cos Z_c \beta_k \sin \beta_K Z_c. \tag{156}$$

The integral

$$G_K = \int_0^{Z_C} \left(\int_0^z G(z')\,dz' \sin \beta_K z \right) dz \tag{157}$$

can be evaluated using integration by parts as

$$G_K = \frac{1}{\beta_K} \left(\int_0^{Z_C} G(z) \cos \beta_K z dz - \cos \beta_K Z_C \int_0^{Z_C} G(z)\,dz \right). \tag{158}$$

It can be shown that the second integral vanishes identically, i.e. $\int_0^{Z_C} G(z)\,dz = 0$ at the present order of approximation. This is immediately seen after integration of (149) along z. For this reason we can calculate G_K only from the first integral in (158).

With orthogonality used through (143)-(145) we arrive at the final set of equations determining the vertical component w of velocity as

$$\begin{aligned} A_K &= \frac{1}{Z_C}\sum_k a_k S_{kK}, && (159)\\ B_K - A_K &= \frac{\alpha_K}{Z_C}\sum_k \frac{b_k - a_k}{\alpha_k} S_{kK} + \frac{4\alpha_K}{Z_C} G_K, && (160)\\ b_k &= \frac{1}{\alpha_k^2 Z_c}\sum_K {\alpha_K}^2 B_K S_{kK}, && (161)\\ b_k + a_k &= \frac{1}{\alpha_k Z_c}\sum_K \alpha_K \left(B_K + A_K\right) S_{kK}. && (162) \end{aligned}$$

A.2 Experiments

A.2.1 Magnetic field

The uniform transverse magnetic field is provided for this experiment by a normal conducting dipole magnet. Its maximum field strength is 2.1 T. The magnetic field has a vertical orientation and is directed perpendicular to the axis of the channel. The magnetic gap used for the experiment has a cubic shape and within a region of 800 mm × 480 mm × 165 mm the field is quite uniform with deviations from the core value smaller than 1%. The operation of the magnet requires a variable DC power supply of 300 V and 1500 A. Therefore, a transductor is used, which is three phase fed from the general power supply and which provides $0 - 300\,\mathrm{V}$ at the output. The magnetic field **B** depends approximately linearly on the applied current I_m. However, for higher magnetic fields the magnet feels already weak saturation which is shown by a slightly nonlinear behavior. This slight nonlinearity is taken into account by a calibration fit of measured field intensities as shown in Fig. 72. A measured shunt voltage U_m in a range $0\,\mathrm{V} < U_m < 0.03\,\mathrm{V}$ corresponds to currents I_m in the range between $0\,\mathrm{A} < I_m < 1500\,\mathrm{A}$.

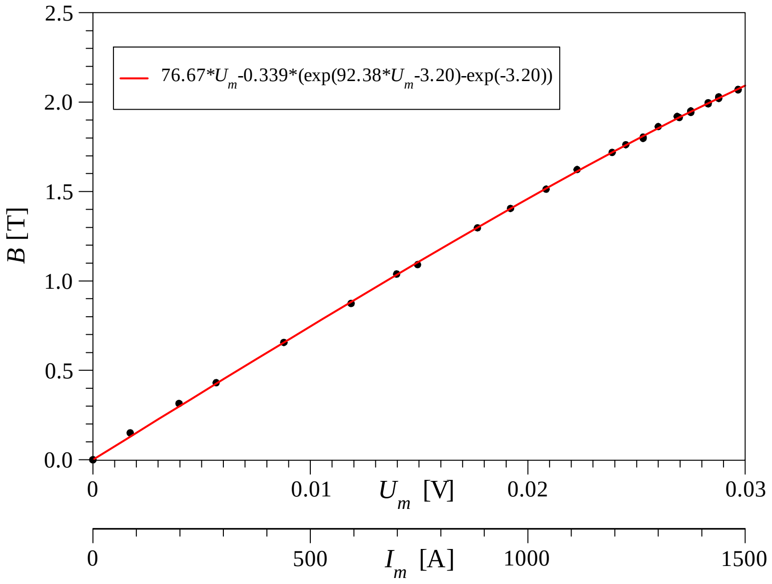

Figure 72: Calibration of magnetic field with measured voltage signal.

A.2.2 Flow rate measurements

An important property for the investigation of MHD flows is the total mass flow rate or the volumetric flow rate that flows through the test section. In order to achieve accurate and redundant results two different types of flow meters are used. One is a so-called gyrostatic (Coriolis) mass flow meter (F1) and the other is an electromagnetic flow meter (F2). The positions of both flow meters in the loop can be seen from Fig. 39.

The gyrostatic flow meter, as sketched in Fig. 73, measures directly the mass flow rate in the liquid metal loop. The measurement principle is based on the Coriolis force that appears when the fluid moves through the measuring U- tube that is forced to oscillations around the axis A.

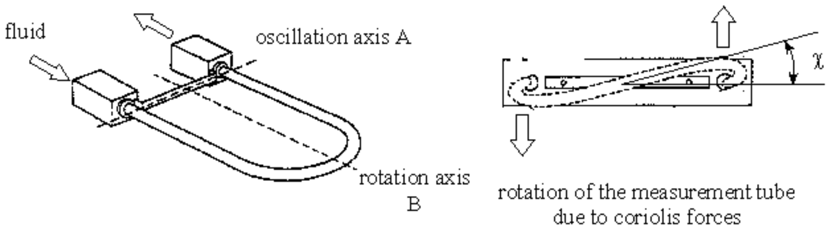

Figure 73: Sketch of the measuring principle of the gyrostatic mass flow meter.

The Coriolis force tends to tilt the initially horizontal U- loop by a certain angle $\varkappa$ around the axis B. This angle of twist is a direct measure $\dot{M}_1$ for the mass flow rate $\dot{M}$. Moreover, the eigenfrequency of the U- shaped loop depends on the mass that is inside the loop so that the instrument gives additionally information on the density ρ of the fluid. The measurements are independent of the kinematic viscosity and the temperature. The used mass flow meter can be adjusted continuously in its measurement range from $\dot{M}_1 = 0 - 3840\,\mathrm{kg/h}$ to $0 - 76000\,\mathrm{kg/h}$ via remote control. The instrument offers the possibility to a self-calibration if the fluid is at rest. The accuracy of the mass flow meter is quite good with relative errors below 1% of the chosen scale. The operation range of the instrument is limited to temperatures below 200 °C and the maximum pressure limit is 40 bar.

The second type of flow meter is an electromagnetic flow meter. The measurement principle is based on Faraday's law, according to which an electrically conducting medium that moves though a transverse magnetic field experiences an induced electric field. The latter one can be detected by electrodes welded at the sides of a channel or pipe. A photograph of the electromagnetic flow meter used in the MEKKA laboratory is shown in Fig. 74. The calibration diagram in Fig. 75 shows the almost perfect linearity between mass flux $\dot{M}_1$ and induced voltage U_2 of this instrument in the considered range of flow rates.

Both flow meters are used in parallel in the range of parameters as shown in Fig. 75, i.e. for $\dot{M} = 0 - 10\,000\,\mathrm{kg/h}$ $(0 - 2.77\,\mathrm{kg/s})$. For higher flow rates it would have been necessary to change the sensitivity of the gyrostatic flow meter which would, however, decrease its accuracy for lower flow rates. For that reason the electromagnetic flow meter is used exclusively for fluxes above $\dot{M} = 2.77\,\mathrm{kg/s}$. For very small flow rates, i.e. for $\dot{M} \lesssim 0.05\,\mathrm{kg/s}$ the gyrostatic flow meter in the present scaling starts to loose its accuracy. Moreover, it turned out that also the electromagnetic flow meter shows some nonlinear behavior for small flow rates, which might have its origin in the fact that the flow at the EM−flow meter returns to a laminar state, whereas calibration has been performed in a turbulent regime. A solution to this problem was achieved by using the first two pressure taps on the test section as an indication for flow rate. Especially for creeping, fully established MHD flows the pressure drop Δp depends linearly on the group $u_0 B^2$. Since pressure drop can be measured with high precision ($\pm 1\,\mathrm{mbar}$), it is possible, after careful calibration, to cover the lower range of flow rates by using the readings of the pressure difference Δp between the first two pressure taps on the experimental test section.

Figure 74: Photograph of the electromagnetic flow meter used for the present experiment.

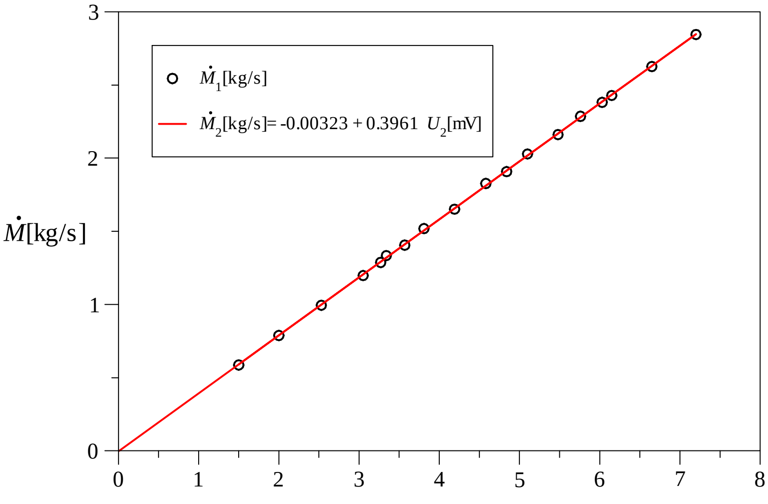

Figure 75: Calibration diagram of the electromagnetic flow meter. Mass flux $\dot{M}_1, \dot{M}_2$ versus induced voltage U_2.

A.2.3 Pressure difference measurements

The pressure difference measurements are performed in the NaK loop via four capacitive pressure transducers mounted in series. Since the pressure transducers are unipolar, the pressure measurement system consists of a line for low pressure, abbreviated with ”L” and another one for high pressure, abbreviated with ”H”, respectively. For details see Fig. 76. All transducers are sensing the same pressure. In order to avoid measurement errors due to nonlinearities near the end of the measurement ranges the ranges for individual transducers are overlapping. From all four readings the one with highest accuracy for the measured data range is selected as *the* measured pressure value.

The measurement principle of a capacitive pressure transducer is very simple. If between the membranes a pressure difference exists the membranes are deformed which leads to a change in electric capacity. This capacity change is transformed in a current ($4\,\mathrm{mA} - 20\,\mathrm{mA}$) that can be measured by a data acquisition system. The accuracy of the pressure transducers used is $\pm 0.5\%$ of the maximum value of the chosen measurement range. An eventual shift of the measurement instrument by temperature changes is compensated by electronics. The operation temperature is limited to 120 °C and the maximum pressure allowed at the membrane is restricted to 140 bar.

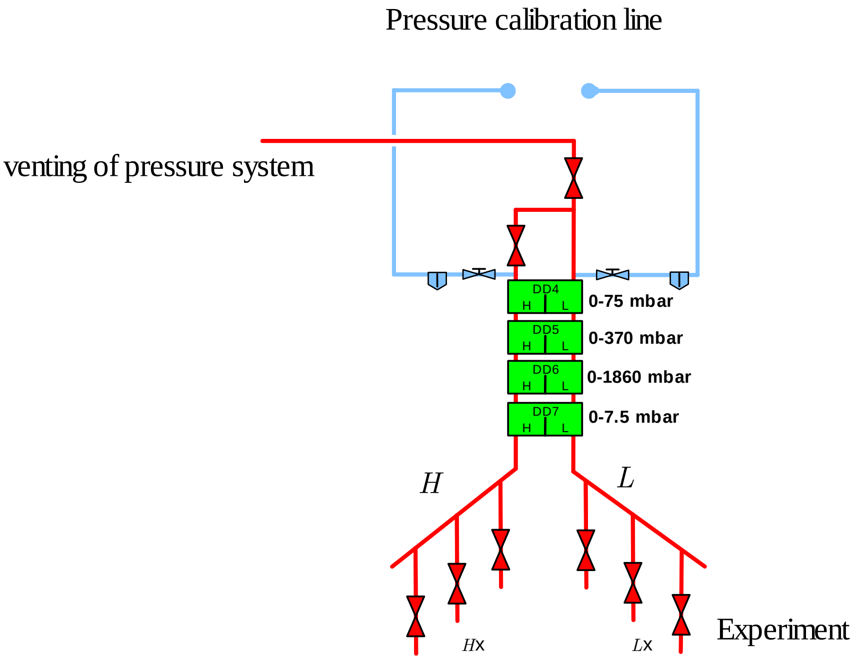

Figure 76: Sketch of the pressure measuring system

A.2.4 Surface potential measurements

Since the walls are thin, the potential measured on the outer surface equals approximately the potential at the fluid-wall interface. Potential measurements give essential information on the flow structure in the ducts since potential can be often interpreted as an approximate streamfunction for the fluid flow and it can be directly compared with theoretical data. The surface of the test section is covered by insulating plates which carry more than 300 potential probes in form of spring-loaded needles for detecting the electric potential on the duct walls. Some of these needles are displayed in a photograph shown in Fig. 77. The fully instrumented test section with surface potential probes has been already shown in Fig. 36. The cables are connected with a multiplexer that switches packages of 20 signals to a digital multichannel nano-voltmeter, which resolves electric potential differences up to an accuracy of $\pm 0.1\,\mu$V. The multiplexer and the nano-voltmeter are controlled by a computer.

Figure 77: Photograph of an insulating plate showing sensing spring-loaded needles.

In order to get more accurate information about potential distribution at the expansion a non-uniform grid spacing has been used for positioning of the electrodes. A really fine mesh has been used to resolve the expansion region and a coarser one is employed in the upstream and downstream parts. The measuring points are mainly distributed on one half of the duct, in $y < 0$. It is expected that the potential distribution is symmetric with respect to the vertical symmetry plane at $y = 0$. Nevertheless, for checking symmetry the other half of the upper wall has been equipped with two additional lines of electrodes. In all experiments performed, the symmetry with respect to $y = 0$ could be confirmed. The positions of potential probes on the small and on the large duct are shown in Fig. 78 and in Fig. 79, respectively. These figures display drawings of the insulating plates, mounted around the test section, which carry the potential probes.

A.2.5 Data acquisition

The measurements were controlled by a computer using a program on the basis of the LabView software. This program controls the valves H_x and L_x of the pressure measuring system, it switches the multiplexer used to measure surface electric potential, it controls and reads the multi-channel nano-voltmeter, the data acquisition cards in the PC etc. Moreover, temperature measurements at the entrance and exit of the test section are used to determine on-line the actual temperature-dependent physical properties of the liquid metal, i.e. $\rho(T)$, $\nu(T)$, $\sigma(T)$, and

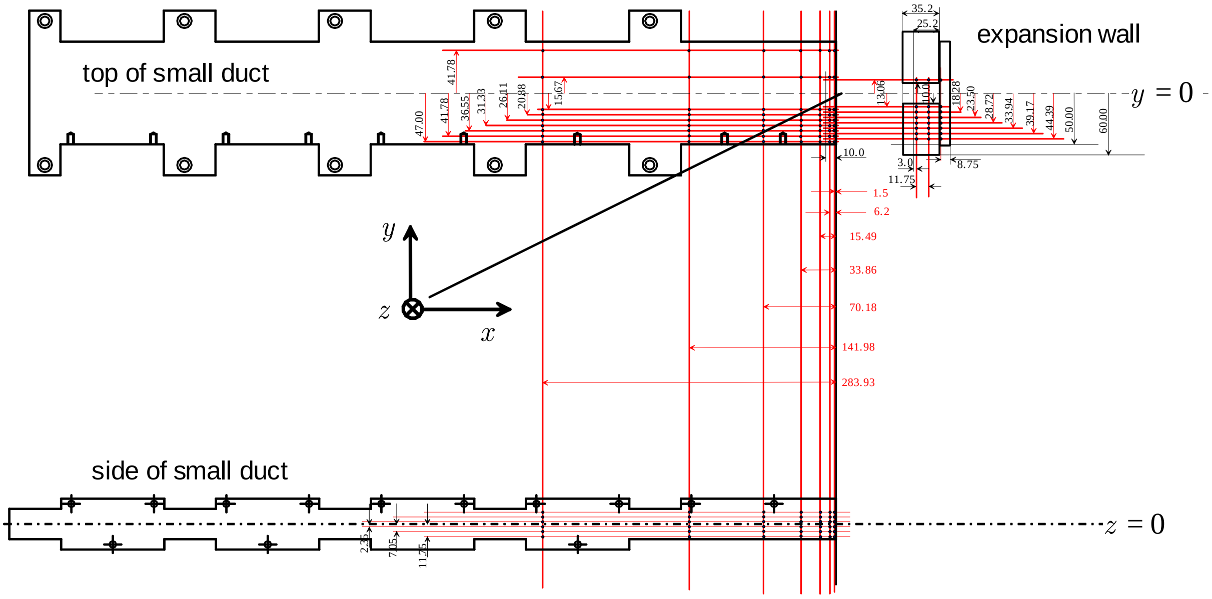

Figure 78: Positions (measured here in mm) of potential probes mounted on the small duct. The figure shows the upper Hartmann wall and the side wall.

together with measurements of B and u_0 it is possible to determine immediately the governing nondimensional parameters, the Hartmann number Ha, the interaction parameter N or the Reynolds number Re.

The measurements were arranged in the following way: the magnetic field and the flow rate are adjusted to give desired Hartmann numbers and interaction parameters. The program then switches automatically one of the 16 levels of the multiplexer, where each level switches 20 potential signals to the multi-channel nano-voltmeter. At each multiplexer level the 20 potential signals are scanned by the voltmeter and send to the PC. For each potential signal an integration time of 2 s is used. The total time for potential measurement at one level of the multiplexer is more than enough to reach a steady state reading at the pressure transducer. After the pressure difference is recorded, the multiplexer is switched to the next level, the pressure system is connected to the next pressure taps and the same procedure is repeated. With this program it is possible to record simultaneously surface potential and pressure variations along the duct. Results are plotted online into a diagram for visualization. This is very helpful since irregularities in the data can be detected immediately and inconsistent measurements can be repeated. This is important since during operation it may happen that sometimes a small gas bubble is occasionally trapped in a pressure tap, which leads to wrong pressure data at that line. In all cases when such inconsistencies have been observed, careful venting of the pressure measuring line removed the defect.

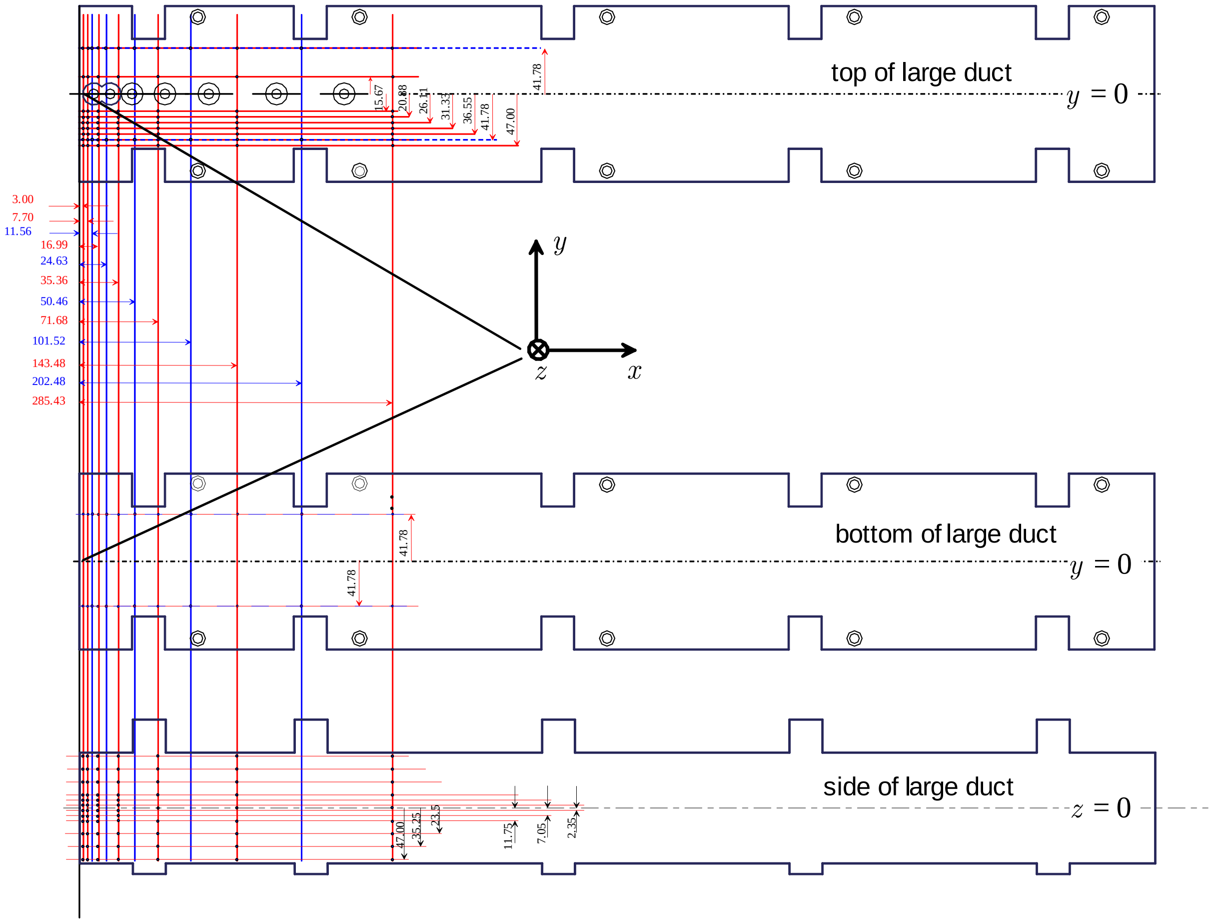

Figure 79: Positions (measured here in mm) of potential probes mounted on the large duct. The figure shows the upper and lower Hartmann walls and the side wall.